A Novel Optimised Design Using Slots for Flow Control and High-Lift Performance of UCAVs

Usman Ali

Aeronautical Engineering

School of Computing Science and Engineering

University of Salford, Salford, UK

Submitted in Partial Fulfilment of the Requirements of the Degree of Doctor of Philosophy, April 2017

Tables of Contents

TABLES OF CONTENTS II

LIST OF FIGURES VI

LIST OF TABLES XIV

ACKNOWLEDGEMENTS XVI

ABSTRACT XVII

CHAPTER 1. INTRODUCTION 1

CHAPTER 2. LITERATURE REVIEW 9

2.1. A Brief Review of Flying Wings 9

2.2. Aerodynamics of Flying Wing 12

2.2.1 Vortex Lift 16

2.2.2 Vortex Breakdown 20

2.2.3 Swept wings 22

2.2.4 Flying Wings at Low Speed 26

2.3. Introduction to Flow Control 27

2.3.1 Radar Cross Section 30

2.3.2 High Lift Devices 32

2.4. Role of UAVs 33

2.5. Computational Aerodynamics 36

2.6. Computational Fluid Dynamics 39

2.6.1 Reynolds Averaged Navier Stokes Equations 48

2.6.2 Turbulence Modelling 52

2.6.3 Near-Wall Turbulence 57

2.7. Vortex Lattice Method 61

2.8. Introduction to Optimisation 67

2.8.1 Optimisation Algorithms 68

2.8.2 Direct Search Methods 70

2.9. Previous Studies 72

2.9.1 Experimental Findings 73

2.9.2 Computational Findings 78

CHAPTER 3. RESEARCH METHODOLOGY 83

3.1. Experiment Methodology 84

3.1.1 Experiment Parameters 84

3.1.2 Wind Tunnel Calibration 86

3.1.3 Experiment Procedure 90

3.2. Computational Methodology 91

3.2.1 Geometry and Grid Details 93

3.2.2 Boundary Conditions 99

3.2.3 Solver Settings 103

3.3. Vortex Lattice Method Approach 107

CHAPTER 4. FLOW VISUALISATION OF CLEAN WINGS 111

4.1. Problem Description 111

4.2. Results and Discussion 114

CHAPTER 5. PREDICTIONS OF STABILITY AND CONTROL 128

5.1. Problem Description 128

5.2. Computational Details 129

5.2.1 Geometry and Grid 129

5.2.2 Solver Settings 132

5.3. Stability and Control Results 133

CHAPTER 6. FLOW CONTROL 140

6.1. Flow Control Description 140

6.2. Flow Control Results 146

CHAPTER 7. NUMERICAL OPTIMISATION 157

7.1. CFD Approach to Optimisation 157

7.2. Computational Details of Optimised Wings 167

7.2.1 Geometry and Mesh Details 168

7.2.2 Solver Settings 172

7.3. Optimisation Results and Discussion 173

CHAPTER 8. CONCLUSION 184

REFERENCES 188

APPENDIX 198

List of Figures

Figure 1.1: Highly swept flying wing UCAV configurations (Google, 2014) 3

Figure 2.1: First turbojet-powered flying wing aircraft (Okonkwo & Smith, 2016) 11

Figure 2.2: B2-Spirit Stealth Bomber (Okonkwo & Smith, 2016) 11

Figure 2.3: Four variants of delta wing planform (J.D. Anderson, 2010) 13

Figure 2.4: Schematic of formation of leading edge vortices over the top of a delta wing at an angle of attack (Houghton & Carpenter, 2003) 14

Figure 2.5: Three regions within leading edge vortex (Earnshaw, 1961).....14

Figure 2.6: Schematic of the spanwise pressure coefficient distribution across a delta wing (J.D. Anderson, 2010) 17

Figure 2.7: Lift coefficient plot for a delta wing showing an increase in lift due to leading edge vortices on the upper side of the wing (Barnard & Philpott, 2010) 19

Figure 2.8: Water tunnel visualisation of vortex breakdown over a delta wing at an angle of attack (Cummings, Forsythe, Morton, & Squires, 2003) 21

Figure 2.9: The deconstruction of free stream velocity into normal and spanwise components (Barnard & Philpott, 2010) 23

Figure 2.10: Effects of sweepback on drag and Critical Mach number (J.D. Anderson, 2010) 25

Figure 2.11: Delta wing air vehicle with vertical fences on the wing (J.D. Anderson, 2010) 26

Figure 2.12: Classification of flow control methods (Jahanmiri, 2010).....28

Figure 2.13: Radar Cross Section signature at 9GHz (a) F-18E Super Hornet, (b) Northrup Grumman X-47B and (c) Generic 40° Swept UCAV (Johnston, July 2012) 31

Figure 2.14: Unmanned Air Vehicle Predator adapted to be used for military purposes (Barnhart, 2012) 34

Figure 2.15: Typical point velocity measurement in turbulent flow (Versteeg & Malalasekera, 2007) 50

Figure 2.16: Visualisation of turbulent flow structures (Versteeg & Malalasekera, 2007).50

Figure 2.17: Structure of turbulent velocity distribution near a solid wall (Bertin, 2002)..59

Figure 2.18: Single horseshoe vortex which is part of a vortex system on the wing (J.D. Anderson, 2010) 62

Figure 2.19: The horseshoe vortex layout for a Vortex Lattice Method (Schminder, 2012) 63

Figure 2.20: Nomenclature for calculating the velocity induced by a finite-length vortex filament (Bertin, 2002) 65

Figure 2.21: A Graphical depiction of pattern search method (Chapra & Canale, 1985) ...71

Figure 2.22: Cross section of a leading-edge vortex (S. A. Thompson, 1992).....75

Figure 2.23: Visualisation of four flow control on right side of wing. The left side of wing is uncontrolled. (a) down-stream obstacle. (b) Suction. (c) Blowing opposite the axial velocity of the vortex core. (d) Blowing along the vortex core (Mitchell & Délery, 2001).....76

Figure 3.1: Flying wing configuration 2 mounted in low speed wind tunnel.....85

Figure 3.2: Weight applied linearly in order to measure lift and drag.....87

Figure 3.3: Weight linearly applied to measure pitching moments.....87

Figure 3.4: New lift calibration with result of 0.3812.....88

Figure 3.5: New drag calibration with result of 0.0691.....88

Figure 3.6: New pitching moment calibration with result of -0.0103.....88

Figure 3.7: Aerodynamic forces and moments comparison between wind tunnel tests for configuration 1 89

Figure 3.8: Typical functions in a computational aerodynamics system (Liu, 2007) 92

Figure 3.9: Planform view and geometric dimensions of baseline clean configuration 1 ..95

Figure 3.10: Planform view and geometric dimensions of baseline clean configuration 2 95

Figure 3.11: Multi-block structured grid for clean configuration 1.....96

Figure 3.12: Multi-block structured grid for clean configuration 2.....96

Figure 3.13: Coefficient of lift solution monitor for configuration 2 at incidence angle of 30° 105

Figure 3.14: Coefficient of drag solution monitor for configuration 2 at incidence angle of 30°.....105

Figure 3.15: Moments coefficient solution monitor for configuration 2 at incidence angle of 30°.....106

Figure 3.16: VLM mesh generated in Tornado for Configuration 1 108

Figure 3.17: VLM mesh generated in Tornado for Configuration 2 108

Figure 4.1: Flying-wing planform geometries used for experimental and computational investigations: 40° configuration (left); and 40° with 60° cranked configuration (right) .112

Figure 4.2: Y^+ distribution on suction sides of configuration 1 (left) and configuration 2 (right) at an angle of attack of $\alpha = 30^{\circ}$.....115

Figure 4.3: Experiment coefficient of lift comparison between configuration 1 and configuration 2 for flat plate models.....118

Figure 4.4: Pressure distribution comparison between configuration 1 (left) and configuration 2 (right) at incidence angle of $\alpha = 20°$.....118

Figure 4.5: Lift coefficient vs angle of attack are shown: 40° configuration 1 (left) and 40° with 60° strake configuration 2 (right) 119

Figure 4.6: Induced-drag coefficient vs angle of attack are shown: 40° configuration (left) and 40° with 60° strake configuration (right).....119

Figure 4.7: Pitching-moment coefficient vs angle of attack are shown: 40° configuration (left) and 40° with 60° strake configuration (right) 120

Figure 4.8: Visualisation of the vortex system on the upper surface of configuration 2 for incidence angles from α = 5° to α = 20° 123

Figure 4.9: Mach number distribution on the upper surface of configuration 2 for incidence angles from α = 5° to α = 20° 124

Figure 4.10: Absolute helicity based Iso surface for incidence angles of α = 20° to α = 40° 124

Figure 4.11: Plots of pressure coefficient distribution and wall shear vectors at incidence angles of α = 15° and α = 20° 125

Figure 4.12: Pressure distribution and surface streamlines on upper surface of configuration 2 for incidence angles from α = 5° to α = 20° 125

Figure 5.1: Trailing edge control surface deflected up at an angle of 10° on configuration 1 130

Figure 5.2: Topology of unstructured grid used in this study for Configuration 1.....131

Figure 5.3: Aerodynamic coefficients and moments comparison between clean and control surface models with respect to angle of attack 135

Figure 5.4: Aerodynamic forces and moments for configuration 1 in sideslip angle of 30° 137

Figure 5.5: Pressure distribution and skin friction lines for alpha = 10° and beta = 30° (left); alpha = 20° and beta = 30° (right).....137

Figure 6.1: Dimensions of leading-edge slot on highly swept flying wing called configuration 2 in this study.....141

Figure 6.2: Dimensions of chordwise slot on highly swept flying wing called configuration 2 in this study 142

Figure 6.3: Meshed configuration 2 with leading-edge slot (left); chordwise slot (right) 142

Figure 6.4: Wings used for the calculations of coefficients of lift.....145

Figure 6.5: Topology of unstructured grid used for highly swept wing 145

Figure 6.6: Comparison of aerodynamic coefficients and pitching moments between clean and leading-edge slot models.....148

Figure 6.7: Pressure distribution and surface streamlines comparison between clean and leading-edge slot models at incidence angle of 5°.....151

Figure 6.8: Pressure distribution and surface streamlines comparison between clean and chordwise slot models at incidence angle of 20° 151

Figure 6.9: Pressure distribution and surface streamlines comparison between clean and chordwise slot models at incidence angle of 25° 152

Figure 6.10: Lift difference comparison between wings with and without chordwise slot at constant angle of attack of 20° 154

Figure 6.11: Lift difference comparison between wings with and without chordwise slots at constant control deflection of 5° 155

Figure 7.1: Positions of chordwise slot for the optimisation analysis, Locations 1 - 8 161

Figure 7.2: Widths of chordwise slot for the optimisation analysis, 0.5mm - 2mm 161

Figure 7.3: Lengths of chordwise slot for the optimisation analysis, 0.06m - 0.10m 162

Figure 7.4: Angles of chordwise slot with respect to trailing edge for the optimisation analysis, 130° - 60° 162

Figure 7.5: Dimensions of optimised chordwise slot 163

Figure 7.6: Horizontal lines on the trailing edge of chordwise slot wing that were used to calculate mass flow rate of the wing 163

Figure 7.7: Mass flow rate as a function of location with interpolated data 164

Figure 7.8: Mass flow rate as a function of location with interpolated data 164

Figure 7.9: Mass flow rate as a function of length with interpolated data 165

Figure 7.10: Mass flow rate as a function of cavity angle with interpolated data 165

Figure 7.11: Flying wing configurations with optimised chordwise slot: Flat plate model (left); GOE444 aerofoil profile wing (right) 169

Figure 7.12: Y^+ values for optimised flat plate slot wing at incidence angle of 30° 170

Figure 7.13: Y^+ values for optimised GOE444 slot wing at incidence angle of 30° 171

Figure 7.14: Topology of unstructured grid for GOE444 wing 171

Figure 7.15: Convergence monitors for optimisation analysis: Residual convergence (left); Lift, Drag and Moments (right).....173

Figure 7.16: Horizontal lines along trailing edge on top and bottom surfaces of the model 175

Figure 7.17: Mass flow rate comparison between clean and chordwise cavity flat plate wings.....175

Figure 7.18: Aerodynamic coefficients and moments comparison between clean and optimised chordwise cavity flat plate wings 176

Figure 7.19: Aerodynamic coefficients and moments comparison between clean and chordwise cavity for flat plate, GOE444 and NACA0008 configurations 180

Figure 7.20: Mass flow rate comparison between clean and chordwise cavity models for GOE444 aerofoil sections 181

Figure 7.21: Pressure distribution and surface streamlines comparison between clean and chordwise cavity for GOE444 wing at angle of attack of 20° 181

List of Tables

Table 2.1: Number of transport equations solved for RANS turbulence models 53

Table 3.1: Reference values for the wind tunnel models 86

Table 3.2: Comparing grid refinement results for configuration 1 at incidence angle of 19.2° 97

Table 3.3: Comparing grid refinement results for configuration 2 at incidence angle of 29° 97

Table 3.4: Comparison of compressible and incompressible computations wherein solutions for far-field and velocity-inlet boundary conditions are analysed for configuration 1 101

Table 3.5: Comparison of far-field boundaries placed at 10c and 15c from the wing for configuration 2 101

Table 4.1: Reference values for CFD computations 115

Table 5.1: Number of elements used for the computations of control surface and clean wings.....131

Table 6.1: Number of elements used for clean, leading-edge and chordwise slot wings for flow control investigations 143

Table 6.2: Number of elements used for the computations of wings 146

Table 7.1: Mesh parameters of Flat Plate and GOE444 wings used for computational analysis 170

Acknowledgements

I would first like to thank my original supervisor Dr. Leslie Johnston who sadly passed away when I was halfway into my PhD. I would like to express my gratitude to my current supervisor Dr. Edmund Chadwick for taking me over as his PhD student, and for the immeasurable support and motivation he has provided throughout this project. I owe my gratitude to lab technicians Dave and Mike for helping me with experiments. Finally, this project would not have been possible without the perpetual love and support of my parents, to whom I shall forever remain indebted.

Abstract

In this study, two UCAV planforms are considered based around generic 40° edge-aligned configurations. One configuration has a moderate leading and trailing edges sweep of Λ = 40°, while the other configuration is highly swept with a leading-edge sweep of Λ = 60° and trailing edges sweep of Λ = 40°. The objectives of the present study on UCAV configurations are two-fold: first to predict aerodynamic performance particularly the maximum-lift characteristics of two flying wing planforms; second to control the flow by inserting leading-edge and chordwise slots and analysing the viscous flow development over the outboard sections of a flying-wing configuration to maximise the performance of control surfaces.

The first part is demonstrated using a variety of inviscid Vortex Lattice Method (VLM) and Euler, and viscous CFD Reynolds Averaged Navier-Stokes (RANS) methods. The computational results are validated against experiment measured in a wind tunnel. The VLM predicts a linear variation of lift and pitching moment with incidence angle, and substantially under-predicts the induced drag. Results obtained from RANS and Euler agree well with experiment.

For the second part, a novel optimised design using chordwise slot is implemented on a highly swept Unmanned Combat Air Vehicle (UCAV) configuration to maximise the lift over

trailing edge control surfaces. More airflow over the control surfaces will result in enhanced lateral control of the air vehicle at medium to high angles of attack. Four parameters describing the chordwise slot are identified for the numerical optimisation. They are: location, width, length and angle of trajectory of chordwise cavity relative to freestream. The angle of trajectory of chordwise slot is measured with respect to the trailing edge of the air vehicle. The results of CFD optimisation are compared with a clean configuration and verified with experiment. The configuration with chordwise slot has shown higher mass flow rate over the control surfaces of the air vehicle in comparison to baseline clean configuration. It is demonstrated that higher mass flow rate results in higher lift. Leading-edge slot method is considered, but the method improves the flow control for the low angles of attack regime, and is found to be ineffective for a highly-swept UCAV configuration at medium to high angles of attack.

Chapter 1. Introduction

The current generation of Unmanned Combat Air Vehicle (UCAV) technology demonstrators employ flying-wing, edge-aligned configurations in order to reduce their Radar Cross Section (RCS) characteristics. The resulting wing-sweep angles are non-optimal from an aerodynamic point of view for vehicles designed to cruise at high subsonic Mach numbers (Schütte, Hummel, & Hitzel, 2012); (Barnard & Philpott, 2010). The highly-swept leading edges of these configurations promote separated-vortex flows at moderate-to-high incidence angles, enhancing lift generation but resulting in substantially increased lateral flow to the outboard sections of the wing (Gudmundsson, 2014a); (Shevell, 1989); (Barnard & Philpott, 2010); (Bertin, 2002); (Kerstin, Andreas, & Martin, 2012); (Frink, Tormalm, & Schmidt, 2012); (Kermode, 2012). This lateral flow separation on outboard sections of the configurations is a limiting factor in the ability to exploit the high-lift generated by the leading-edge vortices. Moreover, separated outboard flows under discussion also adversely impact the stability and control of the air vehicle at medium to high angles of attack, and additionally it generates a nose pitch-up moment as the angle of attack approaches stall (Gudmundsson, 2014a); (Barnard & Philpott, 2010); (Shevell, 1989); (Robert et al., 2007). To address these problems, novel methods of leading-edge and chordwise slots are used for the first time on a flying wing configuration and they successfully control the flow by maximising the lift over control surfaces. It should be noted

that although leading-edge slots have been used on low sweep wings to enhance the lift of air vehicles, to the best of the author's knowledge they have not been used to maximise the performance of control surfaces on highly swept flying wing configurations. Furthermore, the author has not found any literature on flying wing configurations where chordwise slots have been used for the purpose of passive flow control. Therefore, this is novel strand of the research.

Future UCAVs will need to be highly manoeuvrable whilst retaining reduced detectability characteristics in order to ensure their survival in hostile air-defence environments. Modern flying wing UCAV configurations of different stealth designs are shown in Figure 1.1. These aerial vehicles are largely similar in design with geometric features chosen for stealth reasons (Barnard & Philpott, 2010); (Bertin, 2002). It can be noticed from Figure 1.1 that leading and trailing edges of flying-wing configurations are significantly different to those employed on current air vehicles. Moreover, they lack conventional stabilising surfaces or the associated control surfaces, and as a result in its purest form air vehicles suffer from the inherent disadvantage of being unstable and difficult to control (Schütte et al., 2012); (Lee, 2014); (Kermode, 2012); (Barnard & Philpott, 2010). Due to Radar Cross Section (RCS) signature and weight constraints, leading and trailing edges have to be aligned at a common angle of between 40° and 60°, resulting in aerodynamic design between pure deltas, diamond and lambda wings (Tianyuan & Xiongqing, 2009); (Schütte et al., 2012).

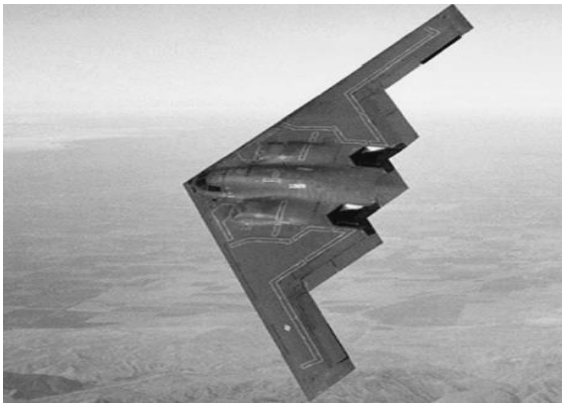

a) *Northrop Grumman B-2 (Barnard & Philpott, 2010)*

b) *BAE Systems Taranis (Lee, 2016)*

c) *Future UCAV Concept (Gursul, Gordnier, & Visbal, 2005)*

d) *Boeing X-45A (Cummings, Morton, & Siegel, 2008)*

Figure 1.1: Highly swept flying wing UCAV configurations

These swept wing vehicles have desirable characteristics of low drag at high speeds. Moreover, they continue to produce lift up to high angles of attack by taking advantage of the additional lift generated by the leading-edge vortices. Leading edge vortex is the main element of flow over swept wings, as it provides lift for flight control at high angles of attack (J.D. Anderson, 2010); (Houghton & Carpenter, 2003); (Wilson & Lovell, 1947); (Hummel & Srinivasan, 1967). A disadvantage, however, is that as the angle of attack is increased, the leading-edge vortices become detached and experience a forward migration or lateral flow to the outboard sections of the wing. The intensity of this forward migration of flow to the outer panels of the vehicle grows in intensity with higher angles of attack (Frink et al., 2012); (Kerstin et al., 2012); (Barnard & Philpott, 2010). As a result of this forward migration of flow to the outer panels of the vehicle, the roll control contributed by trailing edge control surfaces becomes severely restricted, as control surfaces would be operating in a separated flow (Gudmundsson, 2014a); (Barnard & Philpott, 2010); (Shevell, 1989). Therefore, high lift generated by leading-edge vortices cannot be exploited, as control surfaces become ineffective in producing the control forces required for the lateral control of air vehicle at medium to high angles of attack. In addition to the deterioration in roll stability, a powerful nose pitch-up moment is experienced by air vehicle as angle of attack approaches stall (Gudmundsson, 2014a); (Kermode, 2012).

To alleviate these problems, current research has focused on passive flow control techniques such as leading-edge flaps, barriers, canards and fences (Buchholz & Tso, 2000); (D. F. Anderson, 2000); (Kermode, 2012); (Gudmundsson, 2014b). These flow-control techniques, however, cannot be implemented on representative flying-wing configurations due to RCS constraints. Leading edge flaps, barriers and vertical fences can have

detrimental effects on RCS signature, hence they must be avoided (Schütte et al., 2012); (Barnard & Philpott, 2010). Therefore, as an alternative to the above methods, leading-edge and cross-flow slots are used for the first time on a flying-wing configuration and they successfully control the flow by maximising the lift over control surfaces at medium to high angles of attack. With smooth and higher airflow rate over the control surfaces, good roll control can be retained by the air vehicle at medium to high angles of attack (Shevell, 1989). It should be noted that the slots under study lie flush with the surface of the wing, and as a result the effect on RCS signature is expected to be minimal when compared to standard flow-control techniques.

There are two main aims of this study. The first is to enhance our understanding of the flowfield over two low observable UCAV configurations, and their prediction of high-lift performance using high and low fidelity CFD techniques. High-lift performance of an air vehicle can have major influence on vehicle's weight and stability. Therefore, accurate predictions of high-lift performance are of paramount importance. The second aim is to determine whether chordwise slots in the wing improved the lift coefficient at high angles of attack upon control surface deflection and to control lateral flow development on the upper surface of the wing using leading-edge and chordwise slots, and to develop a novel optimised design using a slot to maximise the performance of control surfaces at moderate to high angles of attack.

To achieve the first aim, aerodynamic forces and moments were measured as functions of angle of attack in a low speed wind tunnel and results were compared with in-house and commercial CFD codes using Euler and Reynolds Averaged Navier Stokes (RANS) methods, and low fidelity method Vortex Lattice Method (VLM). Both longitudinal and lateral

stabilities were assessed and the flow features responsible for nonlinearities were highlighted. Computational studies were performed to understand the capabilities of inviscid and viscous flow methods to predict the high lift characteristics, and to analyse the viscous flow development over the outboard sections of UCAV configurations. The flowfield on the upper surface of swept wings was visualised with streamlines. Grid refinement investigations were carried out to examine the effects of grid resolution on the solution. Moreover, computational investigations into turbulence models, boundary conditions, and solvers were performed to analyse the effect of different computational choices on the solution of flying wing configurations.

The second aim was achieved by performing computational investigations for flow control on wings with leading-edge and chordwise slots. The results of computational investigations were compared with clean configurations and verified with experiment. Leading-edge and chordwise slots were considered because they lie flush with the surface of the wing, and thus are expected to have a reduced RCS signature. A novel optimised design was developed for a chordwise slot using a numerical optimisation method. The optimised design was implemented on a highly-swept UCAV configuration to maximise the performance of trailing edge control surfaces of the wing. The mass flow rate normal to trailing edge of optimised UCAV configuration was measured and compared with the clean configuration.

Chapter 2 of this thesis covers background and literature review on UCAV flying wing configurations. This chapter includes a brief review and description on fundamental aerodynamics of flying wing configurations. The current flow control techniques and their limitations in the context of Radar Cross Section (RCS) signature are highlighted. The roles

of modern UCAVs, and different types of methods used in Computational Aerodynamics for the resolution of aerodynamic problems of flying wing configurations are discussed. The theoretical background of nonlinear and linear computational methods is elaborated. This is followed by a brief introduction on Numerical Optimisation and its algorithms. Finally, critical review of papers and summary of previous studies on swept wings are presented. Chapter 3 covers the research methodology of the study. In this section, experiment and computational approaches used for the analysis of clean UCAV configurations are described. The parameters used for experimental and computational investigations of clean configurations are presented in this section as well. Chapter 4 is a detailed investigation into the comparison of moderately and highly swept clean UCAV configurations. The capability of linear and nonlinear methods to predict the high-lift characteristics and vortex structure of flying wing configurations is investigated. Moreover, viscous flow development over the outboard sections of flying wing configuration is analysed using surface streamlines. Chapter 5 presents detailed investigation into the prediction and stability of wing with a moderate leading-edge sweep. Pitch and yaw characteristics of UCAV configuration are predicted using computations and compared against experiment. Furthermore, RANS computations of deflected control surfaces are compared with a clean configuration to assess the efficiency of trailing edge control surfaces. Chapter 6 describes an investigation into leading-edge and chordwise slots for the purpose of passive flow control. The computational results of leading-edge and chordwise slots are compared with clean configurations and verified with experiment. The chapter also covers computational analysis to ascertain whether chordwise slots in the wing improved the lift upon deflection of control surface. Chapter 7 of this thesis presents analysis of novel optimised design of chordwise slot using a numerical optimisation

method. The mass flow rate of optimised configuration is calculated over trailing edge and compared with the clean configuration. The computational results of optimised configuration are verified with experiment. Chapter 8 draws conclusions on above work and makes suggestions for the future work.

Chapter 2. Literature Review

2.1. A Brief Review of Flying Wings

The conventional air vehicles have been using a prevalent design for last five decades, where fixed wings are attached to the cylindrical fuselage, with a rear tail for stability. The fuselage of aircraft performs sole function of carrying payload contributing almost nothing to aerodynamic efficiency other than added drag, as wings alone provide the required lift to keep the aircraft airborne. Although conventional design has been useful from stability point of view, but it compromises aerodynamic efficiency of the entire aircraft (Ordoukhanian & Madni, 2014). On the contrary, flying wing aircraft has no horizontal and vertical control surfaces, leading to stability and control issues (Shevell, 1989); (Schütte et al., 2012); (Rehman, 2009). The flying wing design has no discernible fuselage section as it blends fuselage and wings into single lifting surface, making it aerodynamically compact and efficient system (Bolsunovsky et al., 2001); (Dehpanah & Nejat, 2015). It should be noted that flying wing design is different from a Blended Wing Body (BWB) aircraft design in that it has no definite fuselage for carrying payloads. On the contrary, BWB design has a flattened fuselage for carrying payload (Okonkwo & Smith, 2016). The advantage of flying wing design is that entire aircraft contributes in generating the required lift to keep the vehicle airborne. Moreover, this system reduces drag for high subsonic air vehicles at cruise

speeds, resulting in a fuel-efficient aircraft design. Therefore, flying wing systems emit less pollutants as they burn less fuel, making it more environmental friendly (Okonkwo & Smith, 2016). The flying wing system also has low noise signature when compared with conventional air vehicles (Mistry, 2009); (Kundu, 2014).

The concept of a flying wing aircraft was introduced by a German Engineer Dr. Adolph Busemann at Fifth Volta Conference held in Rome in September 1930. Although, Dr. Busemann is credited with introducing the concept of a flying wing, but another German Engineer, Dr. Alexander Lippisch, had been experimenting with swept wing and tailless aircraft for several years, and he is credited with the first flight of a swept wing aircraft in 1931. Dr. Lippisch was primarily interested in reducing the aerodynamic drag and increasing the flight speeds, therefore he chose to explore the potentials of a flying wing design (Pattillo, 2001); (S. A. Thompson, 1992). The desire to increase flight speeds was found in many parts of the aviation industry at that time, but the concept of a flying wing was not investigated to its full potential until the development of jet engine in the early 1940's. After the introduction of jet engine in aviation, transonic speeds became attainable, and therefore research investigations on swept wing aircrafts soon began to increase (S. A. Thompson, 1992); (Pattillo, 2001).

The Horten Brothers, Walter and Reiman Horten, who served in the German Army during Second World War worked extensively on the flying wing concept from 1931 to 1944. Their contribution to flying wing concept came in the form of Ho-series flying wing aircraft. Horten brothers are credited with the flight of first turbojet powered flying wing aircraft called Ho-IX, shown in Figure 2.1 (Okonkwo & Smith, 2016); (Rehman, 2009).

Figure 2.1: First turbojet-powered flying wing aircraft (Okonkwo & Smith, 2016)

Figure 2.2: B2-Spirit Stealth Bomber (Okonkwo & Smith, 2016)

Jack Northrop in United States explored the potentials of flying wing concept, as he was convinced of aerodynamic advantages of wing sweep and fewer control surfaces on an air vehicle. Northrop established the Northrop's corporation in 1927, building several flying wing aircrafts including N-1M, N-9M, XB-35, YB-35 and so on (Okonkwo & Smith, 2016).

The most successful flying wing aircraft of Northrop Corporation was developed in 1980s, after the advent of modern fly-by-wire technology. The aircraft in question is known as B2 Spirit, and is shown in Figure 2.2. The primary advantages of B2 bomber include stealth design, better payload carrying capability and considerably better flight control characteristics due to the incorporation of fly-by-wire technology (Okonkwo & Smith, 2016); (Rehman, 2009). Some of the earliest contributions to the Flying Wing design were also made by Lt. John Dunne in United Kingdom. Dunne realised the importance of wing sweep and incorporated it in his tailless glider and series of powered bi-planes (Rehman, 2009).

2.2. Aerodynamics of Flying Wing

Although all types of wings are expected to suffer from flow separation at high angles of attack due to viscous effects, but sharped edged swept wings under consideration in this study are particularly affected by this phenomenon (J.D. Anderson, 2010). To investigate the aerodynamic properties of a flying wing planform, the flow physics of a delta wing can be evaluated. The term delta wing refers to a wing with a triangular planform as shown in Figure 2.3. The figure in question shows four different variants of a delta wing planforms. As a variant of a delta wing aircraft, the flying wing vehicles are expected to exhibit aerodynamic properties commonly associated with traditional delta wings (Robert et al.,

2007). When the capability of a flying wing aircraft at medium to high angles of attack is taken into consideration, the presence of leading-edge vortices must be considered. The understanding of leading-edge vortices can be furthered by examining the flowfield of delta wings shown in Figure 2.4.

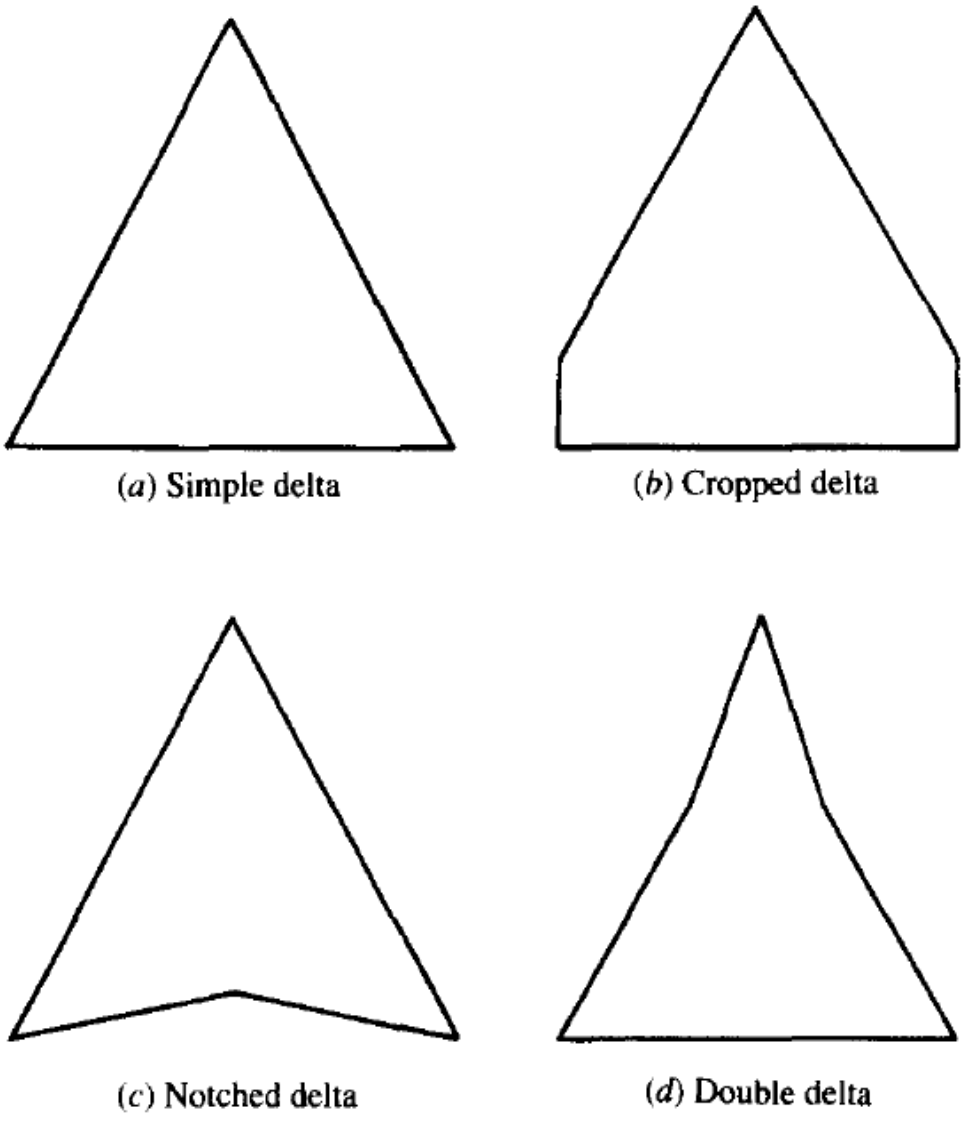

Figure 2.3: Four variants of delta wing planform (J.D. Anderson, 2010)

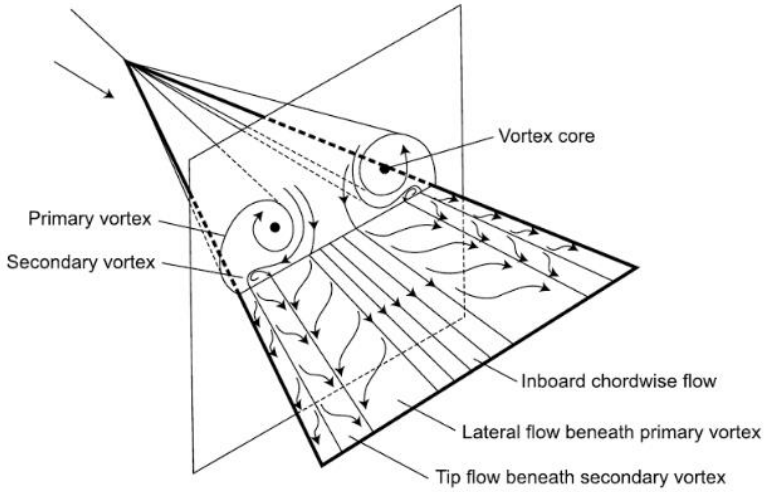

Figure 2.4: Schematic of formation of leading edge vortices over the top of a delta wing at an angle of attack (Houghton & Carpenter, 2003)

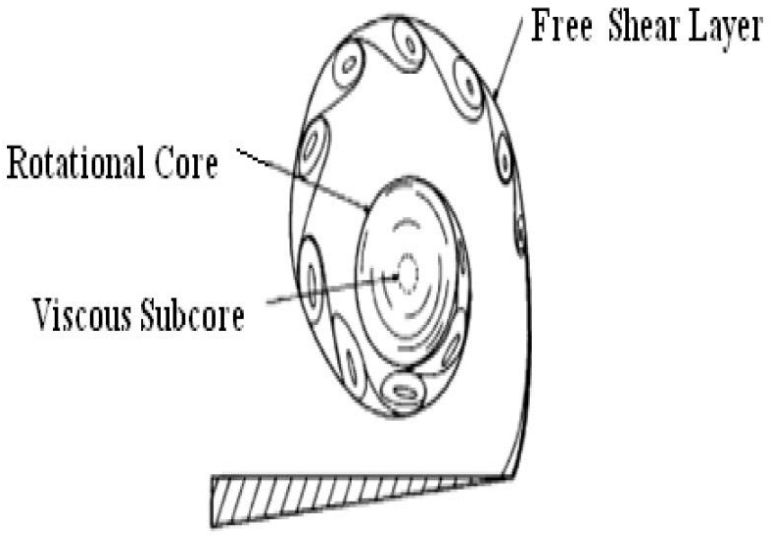

Figure 2.5: Three regions within leading edge vortex (Earnshaw, 1961)

Experimental investigations have established that at relatively low angles of attack the flow separates from the leading edges and rolls into two vortex sheets of rotating fluid (Lambourne & Bryer, 1959); (Earnshaw, 1961); (Delery, 2001); (Elle & Britain, 1961) as illustrated in Figure 2.4. When sharp leading edge of the wing is encountered, a free shear layer is formed which rolls into a vortex. This phenomenon transpires on both sides of the wing, resulting in the formation of two counter rotating vortices. This pair of vortices is the cause of high lift and delay in wing stall to a higher angle of attack for delta wing configurations (J.D. Anderson, 2010). The angle of attack at which these vortices are first formed is mainly a function of wing sweep angle (Gursul, Wang, & Vardaki, 2007), as will be explained in a later section.

The primary vortex pair is formed due to the flow separation that transpires at the leading edge of the wing (Lambourne & Bryer, 1959); (McLean, 2013). These primary vortices start as small shear layers, but grow in size extending from the apex to the trailing edge of the wing. The free shear layer rolls and contacts the surface of the wing, creating attachment lines all the way to the trailing edge of the wing. The internal structure of the vortex can be divided into shear layer, rotational core and viscous sub-core as shown in Figure 2.5 (Earnshaw, 1961). The outer shear layer increases in diameter with the distance from the apex of the wing. The rotational core of the vortex, covers about 30% of the local semi span diameter, and only small variation in longitudinal velocity are produced in this region. Although, the viscous sub-core covers about 5% of the local semi span diameter, but this is the region where high velocity is produced with longitudinal velocity exceeding three times the freestream value (Earnshaw, 1961).

As noted earlier, the separated vortex flows under the influence of vorticity contained within it, rolls up in a spiral fashion to form a primary vortex pair (Wilson & Lovell, 1947); (Lambourne & Bryer, 1959) shown in Figure 2.4. The inner core region in the centre of the vortex is influenced by the viscous forces as illustrated in Figure 2.5, and has characteristics of large velocity and pressure gradients. The core gives rise to strong swirling velocities and associated with this a strong negative pressure on the suction side of the wing (Earnshaw, 1961); (J.D. Anderson, 2010). The primary vortex pair creates lateral boundary layer on the suction side of the wing, colliding with the primary separation and resulting in secondary vortex as shown in Figure 2.4. The secondary vortex is smaller and weaker, is located outboard and rotates in opposite direction to the primary vortex. However, unlike primary vortex, strength and size of secondary vortex is dependent on Reynolds number, and is a function of area covered by the lateral boundary layer flow. This system of vortical flows exist up to very high incidence angles for delta wing planforms (Delery, 2001); (Frink et al., 2012).

2.2.1 Vortex Lift

The strength and energy of separated vortex increases with incidence angle, resulting in axial velocity in the vortex core to exceed three times the freestream velocity (Earnshaw, 1961). The high velocity of fluid within vortex core causes a significant drop in pressure on the upper surface of the wing. This results in high lift as upper surface of the wing is exposed to lower pressure than the bottom surface of the wing (Wilson & Lovell, 1947); (Barnard & Philpott, 2010). High lift coefficients achieved by delta wing planforms, at moderate-to-high incidence angles, are therefore primarily due to the separation of

leading edge vortices on the upper side of the wing (Polhamus, 1969); (Campbell & Osborn, 1986); (Newsome & Thomas, 1986).

They leading edge vortices formed on both sides of delta wing are strong and stable, and consequently they increase the energy of vortex flows. This results in local static pressure to drop in the vicinity of leading-edge vortices. Therefore, surface pressure on the upper side of wing is reduced near the edges of the delta wing, but remains reasonably constant over the middle of the wing as is shown in Figure 2.6. It should be noted that Figure 2.6 shows the spanwise pressure variation over the upper surface of a delta wing (J.D. Anderson, 2010).

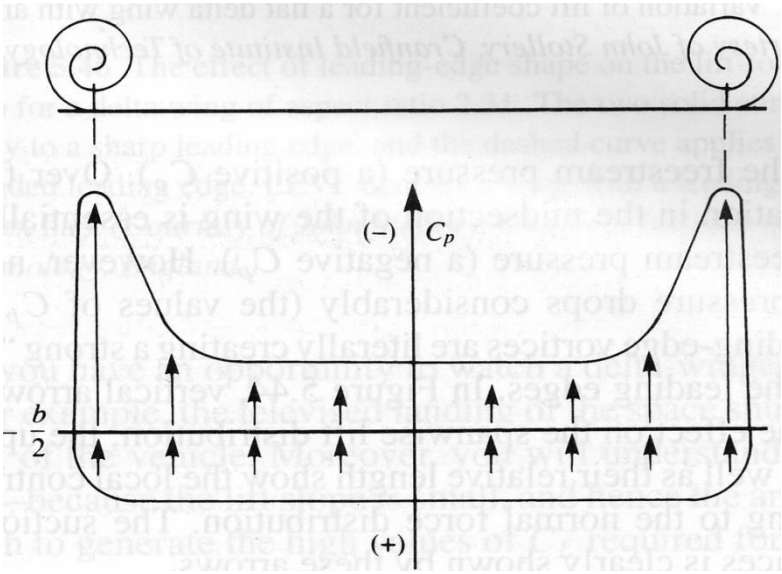

Figure 2.6: Schematic of the spanwise pressure coefficient distribution across a delta wing (J.D. Anderson, 2010)

The spanwise pressure distribution over the bottom surface of the wing remains constant but higher than the freestream pressure. On the upper surface of the wing, the pressure

remains constant in the mid-section but lower than the freestream pressure. The considerable drop in pressure over the upper surface can be observed near the edges of delta wing, depicted by vertical arrows in Figure 2.6. This is the result of leading-edge vortices creating a strong suction over the top surface of the wing near the edges of the delta wing. The length of arrows in Figure 2.6 represent the local lift contribution of each section on the upper and lower sides of the delta wing (J.D. Anderson, 2010).

This suction effect is the cause of lift enhancement over delta wings, and the reason why delta wing configurations obtain much higher lift coefficients for angles of attack at which conventional wings would normally stall (J.D. Anderson, 2010). The separated vortices on the upper surface of the wing make an extra contribution to lift known as vortex-lift (Polhamus, 1969); (Barnard & Philpott, 2010). For subsonic flows, total lift of delta wings is a combination of attached potential flow and vortex lift. This method is termed as the leading-edge suction analogy and can be represented by the following equation:

$$C_L = K_P sin\alpha cos^2\alpha + K_V cos\alpha sin^2\alpha \qquad \textbf{(2.1)}$$

where K_P and K_V are coefficients that can be found approximately by $2\pi tan\Lambda$ and 1.95 respectively, or they can be determined from experimental data (Houghton & Carpenter, 2003). The Figure 2.7 shows an increase in lift coefficients over the upper surface of a delta wing due to the leading-edge vortices. It can be noticed that at high incidence angles, leading edge vortices make a considerable non-linear contribution to the lift of the wing (Barnard & Philpott, 2010).

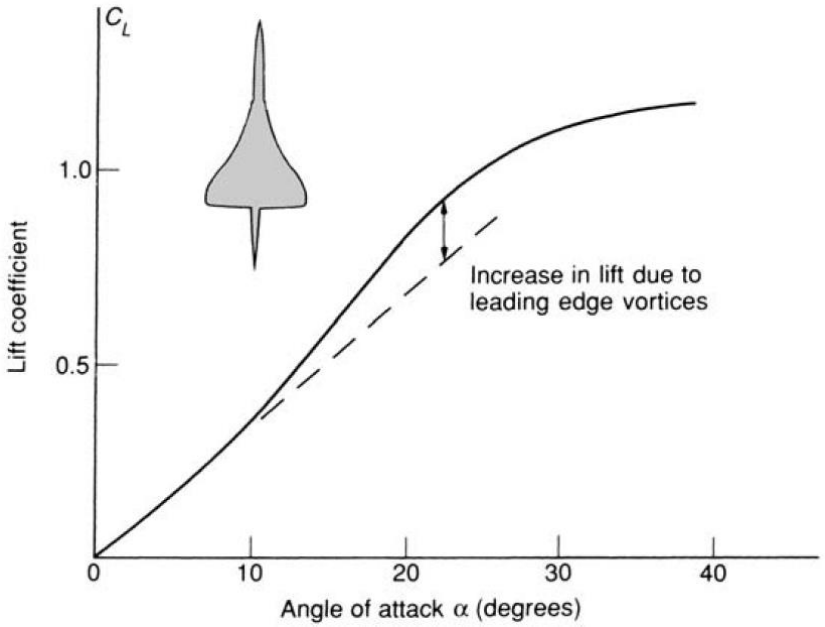

Figure 2.7: Lift coefficient plot for a delta wing showing an increase in lift due to leading edge vortices on the upper side of the wing (Barnard & Philpott, 2010)

The aerodynamic properties of delta wing planforms are considered to be a strong function of wing sweep angle (Earnshaw, 1961); (Siouris & Qin, 2007). The leading edge geometry and thickness are additional factors that affect the flow physics of delta wings, but variations in Reynolds number do not have a considerable effect on aerodynamic properties, as primary flow separation point is fixed for sharp leading edges regardless of Reynolds number of delta wing planforms (Peckham, 1958); (Elkhoury & Rockwell, 2004). Therefore, aerodynamic forces and moments do not change substantially with Reynolds number, in comparison to stronger factors such as incidence angle and wing sweep. High Reynolds number, however, decrease the vortex diameter adding energy and velocity to the core resulting in a tightly wrapped core (Delery, 2001). It should be noted that in this study only configurations with sharp leading edges are considered.

2.2.2 Vortex Breakdown

At high angles of attack, leading edge vortices undergo a transition known as vortex breakdown or vortex bursting shown in Figure 2.8. The phenomenon of vortex breakdown was first observed in a water tunnel, where it was discovered that vortex flow undergoes an abrupt decrease in the magnitude of axial and circumferential velocity components (Peckham, 1958), and core of the vortex suddenly increases in cross sectional area when incidence angle is increased beyond a critical angle of attack. It can be observed from Figure 2.8 that upstream of vortex breakdown, the flow is tightly bound, but downstream of vortex breakdown the flow is highly turbulent. The vortex breakdown causes the flow to become stagnant, exhibiting large scale of unsteadiness (Lambourne & Bryer, 1961).

As noted earlier, the vortex increases in velocity and energy with the angle of attack, and at low angles of attack the vortex burst transpires near the trailing edge of the wing without affecting the vortex lift of the wing (Hummel & Srinivasan, 1967). However, at a certain point, a sudden decrease in the strength of the primary vortex occurs. It should be noted that axial velocity in the sub-core region was measured to be three times higher than the freestream velocity upstream of vortex breakdown region. However, after the breakdown, significant drop in the axial velocity was noticed in the region of vortex breakdown, and this results in decrease in lift due to the rise in static pressure on the suction side of the wing (Earnshaw, 1961). The incidence angle at which vortex breakdown occurs depends on the sweep angle, and to a lesser extent, the leading edge shape and the wing thickness (Earnshaw, 1961); (Elkhoury & Rockwell, 2004).

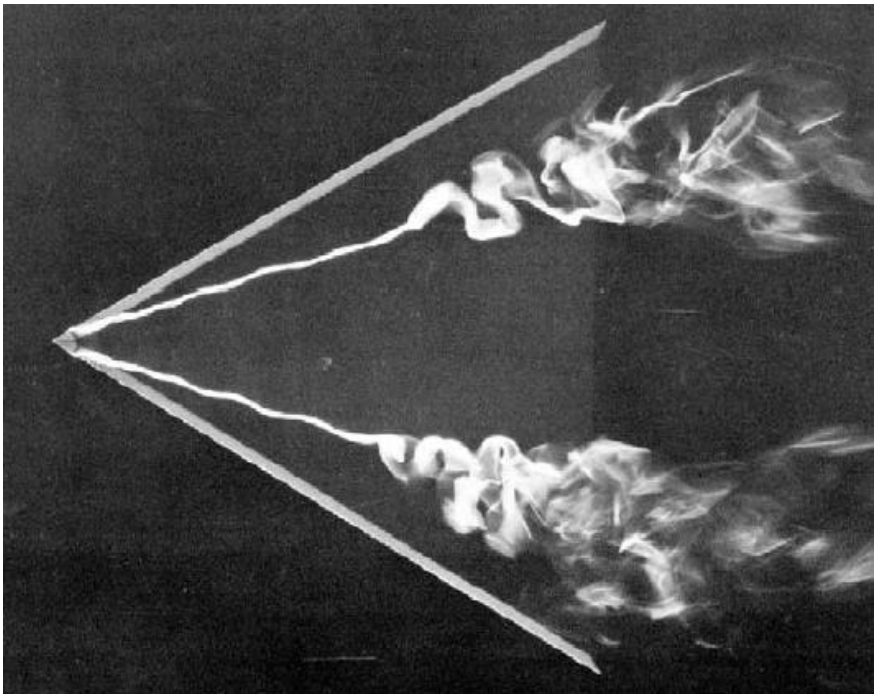

Figure 2.8: Water tunnel visualisation of vortex breakdown over a delta wing at an angle of attack (Cummings, Forsythe, Morton, & Squires, 2003)

The vortex breakdown first occurs near the trailing edge of the wing, and then moves forward as angle of attack is increased. When vortex burst reaches the vicinity of the apex of the wing, a further increase in angle of attack results in the loss of coherent vortex flow over the wing, leading to total flow separation (Lambourne & Bryer, 1961); (Mitchell & Délery, 2001). However, unlike conventional wings, the catastrophic loss of lift does not occur for delta wings when a certain angle of attack is reached, rather a gradual loss of lift has been noticed beyond the critical incidence angle of attack (Houghton & Carpenter, 2003). Vortex breakdown has been focus of the research in the aerospace community as it can create large changes in pitching moments, thus affecting the stability of air vehicle (Breitsamter, 2008).

2.2.3 Swept wings

With the advent of jet engine transonic speeds became possible, and research started to focus on problem of raising the critical Mach number by delaying the onset of shockwaves (Kermode, 2012). It is a formidable task to design a wing that behaves well in both low and high speed flows, as flows of different types can drastically change the control and stability characteristics of air vehicle (Barnard & Philpott, 2010). Wing sweep is often used on both civil and military aircrafts to reduce the effects of compressibility at transonic speeds. It should be noted that wing sweep can be backward sweep or forward sweep. The latter type of sweep is less common and is not considered in this study. The purpose of the wing sweep is twofold: first to raise the critical Mach number of flows by delaying the onset of shockwaves; and second to resolve a potential Centre of Gravity (CG) problem in an aircraft design (Gudmundsson, 2014a). In a low speed aircraft, wing sweep allows to fix Centre of Gravity (CG) problem if it is discovered that CG is further forward or aft than expected. Backward wing sweep was used for this purpose on DC-3 Dakota, and forward sweep was used on SAAB MFI-15 Safari to solve the CG issue that resulted from the engine and two occupants sitting in front of the main spar (Gudmundsson, 2014a).

Wing sweep can also have a huge impact on the critical Mach number of the aircraft. The greatest benefit of wing sweep for high speed aircrafts is in the reduction of strength and delay in the formation of shockwaves (Kermode, 2012); (Gudmundsson, 2014a). The formation of shockwaves not only results in sharp increase in drag, but it also alters the chordwise pressure distribution of the wing, causing the centre of the lift to move from quarter chord position to the centre of the wing. The change in centre of lift causes a severe

increase in nose-down pitching moment in a phenomenon termed as Mach-tuck (Gudmundsson, 2014a).

The Figure 2.9 illustrates how wing sweep raises the critical Mach number and delays the onset of shockwaves. The airflow can be divided into two components of velocity, one normal to the span and one along the direction of the span of the wing. The component of velocity along or parallel to the span can be ignored as it does not change considerably as the flow passes over the wing. The normal component of the velocity is responsible for the pressure distribution but it is lower than the freestream velocity (Barnard & Philpott, 2010); (Kermode, 2012). The normal component can be represented by the free stream velocity V_∞, and leading-edge sweep angle Ψ by the following relationship:

$$V_n = V_\infty cos\Psi \qquad \textbf{(2.2)}$$

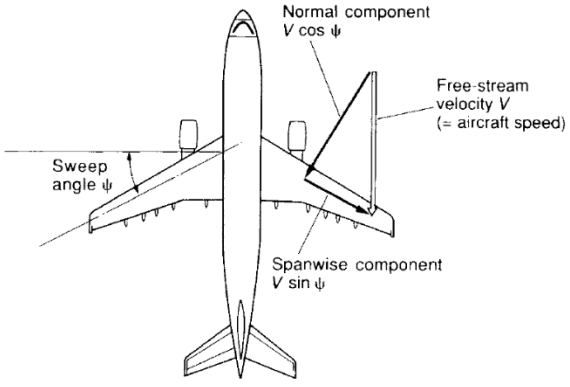

Figure 2.9: The deconstruction of free stream velocity into normal and spanwise components (Barnard & Philpott, 2010)

With sufficient wing sweep, the normal component of the velocity becomes considerably slower than speed of the sound even when aircraft is flying in supersonic speed regimes (Kermode, 2012); (Barnard & Philpott, 2010). A look into flow past a section of a swept wing reveals that flow patterns and general flow features are similar to ordinary subsonic flow as long as normal component of the velocity remains subsonic. Even when resultant of normal and spanwise components of velocity has become supersonic in places, the flow features remain subsonic.

The wings of aircraft have to be swept even when aircraft is not intended to fly at supersonic speeds, as airflow becomes supersonic on the upper surface of the wing where it is moving faster than the freestream velocity. This phenomenon occurs when aircraft has a flight speed of 60 to 70 percent of the speed of the sound. Civil aircrafts for medium to long-haul flights fly faster than 70 percent of the speed of the sound, therefore swept wings are used to delay the onset of shockwaves on such aircrafts (Barnard & Philpott, 2010).

Figure 2.10 shows the effects of sweepback on critical Mach number and drag on a straight wing and results are compared with two moderately swept wings. One wing has a sweep of 30°, while other has a higher sweep of 45°. The Figure 2.10 shows that sweepback not only increases the critical Mach number but it also reduces the rate at which drag coefficients rise. Moreover, it reduces the peak of drag coefficients, with 45° sweep reducing it more than 30°. The Figure in question shows three different types of wings with aspect ratio of 3 and thickness-to-chord (t/c) ratio of 5%. It can also be noticed from Figure 2.10 that sweepback has very little advantage above Mach = 2 (Kermode, 2012). The increase in critical Mach number is helpful as it allows for the aircraft to use thicker and structurally more efficient aerofoils in the wings (Gudmundsson, 2014a). Swept wings have

their advantages when aircraft is designed to cruise close to or above speed of sound. However, sweep should be avoided on a low speed aircraft unless necessary (Barnard & Philpott, 2010); (Gudmundsson, 2014a).

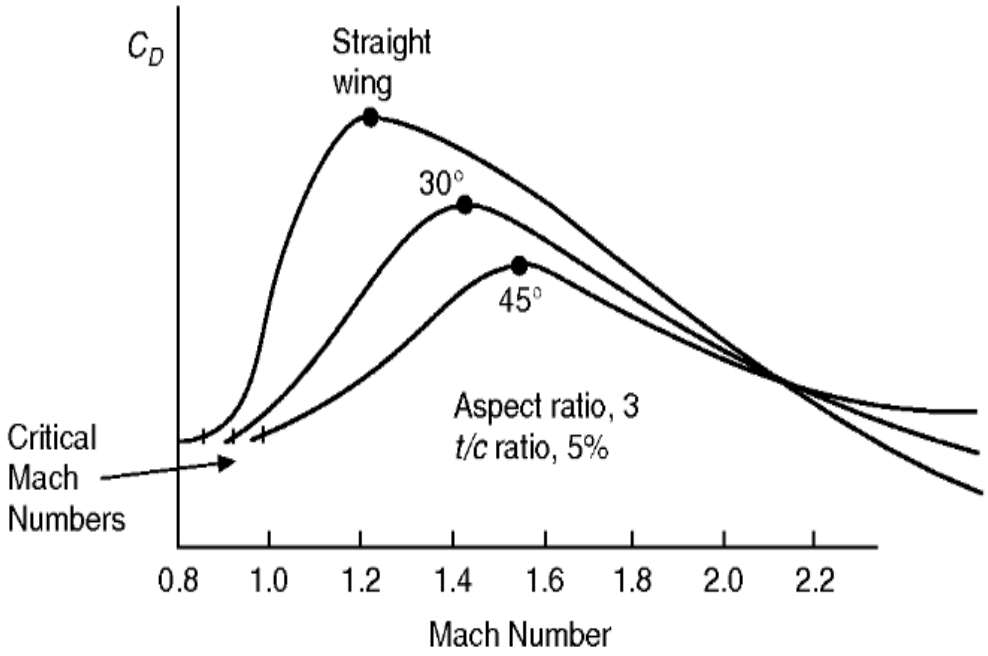

Figure 2.10: Effects of sweepback on drag and Critical Mach number (J.D. Anderson, 2010)

Although, only normal component of velocity contributes to the lift, but both spanwise and normal components contribute to the drag. Therefore, swept wings have poorer lift to drag ratio when compared with equivalent straight wings (Barnard & Philpott, 2010). Another implication of wing sweep is that upwash makes the tips stall first when wing approaches stalling angle. The tip stall results in centre of lift to move forward, causing the aircraft to pitch up and thereby pushing it further into stall. This issue of tip stalling was encountered on early swept aircrafts, and can be resolved by either moving the wings forward or by

introducing a washout in the wing design (Coppin, 2014). The washout prevents tip stalling first by keeping root at higher angle of attack than the tip of the wing when aircraft approaches stall (Kermode, 2012); (Barnard & Philpott, 2010).

2.2.4 Flying Wings at Low Speed

The idea behind wing sweep is that by putting the leading edge at an angle relative to the direction of air flow, the critical Mach number can be delayed. This results in reduced wave drag, making air vehicles under consideration suitable for high cruise speeds (Gudmundsson, 2014a); (Barnard & Philpott, 2010); (S. A. Thompson, 1992). However high speed air vehicles, such as one shown in Figure 2.11, fly at low speeds for take-off and landing, and spend most of their time flying at subsonic speeds using supersonic capability only for short periods of time (J.D. Anderson, 2010).

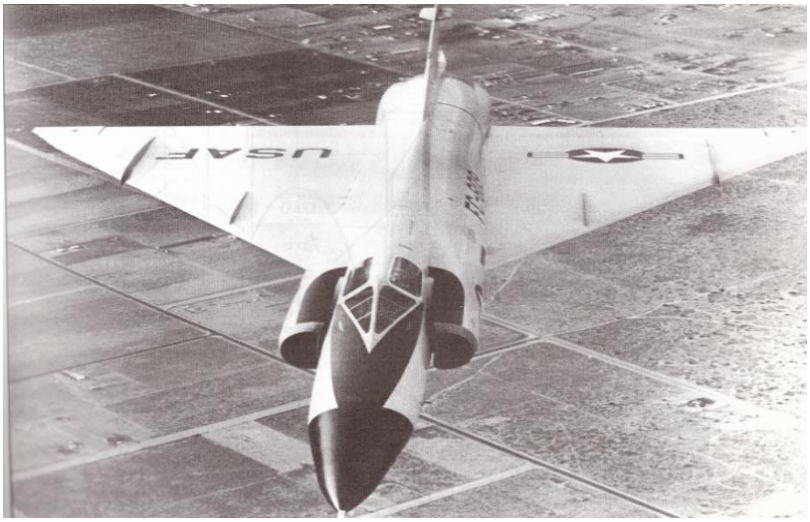

Figure 2.11: Delta wing air vehicle with vertical fences on the wing (J.D. Anderson, 2010)

At subsonic speeds, the aerodynamic behaviour of swept wing vehicles is different than the high aspect ratio wings (Gudmundsson, 2014a). The performance of swept wing vehicles at low speeds is crucial as the mission roles of modern air vehicles require them to operate at low speed and variety of alpha conditions during various flight phases such as take-off and landing (Houghton & Carpenter, 2003); (J.D. Anderson, 2010). Therefore, understanding of aerodynamic properties of subsonic flows for these vehicles is essential.

As noted earlier, one of the unique aspects of flying wing configurations is that they generate high lift at high angles of attack. This aspect of flying wings makes them suitable for military applications, as such applications have begun to encompass very high incidence angles for their flight envelopes (Robert et al., 2007). Furthermore, flight operations such as landing, take off and combat manoeuvring are encountered at moderate to high angles of attack regimes (Coppin, 2014). Therefore, flow physics of subsonic flows for flying wing configurations at moderate to high incidence angles is of immense significance. It should be noted that the high lift generated by the leading edge vortices on delta wing configurations cannot be fully exploited due to the spanwise flow to the outboard sections of the wing (Shevell, 1989); (Coppin, 2014). One of the objectives of this research is to control the spanwise flow on the outboard sections of the wing to enhance the lateral control of the flying wing configurations.

2.3. Introduction to Flow Control

In order to meet Radar Cross Section (RCS) demands on flying-wing configurations, the vertical tails or the associated control surfaces have to be avoided which makes aerodynamic stability and control a special problem for an air vehicle (Schütte et al., 2012).

This study explores the flow control mechanisms which can limit the development of the lateral flow to the outboard sections of a flying wing configuration. The objective is to route more airflow over the control surfaces of the trailing edges of the air vehicle. More airflow over the control surfaces will result in effective lateral control of air vehicle at medium to high angle of attack (Barnard & Philpott, 2010); (Shevell, 1989).

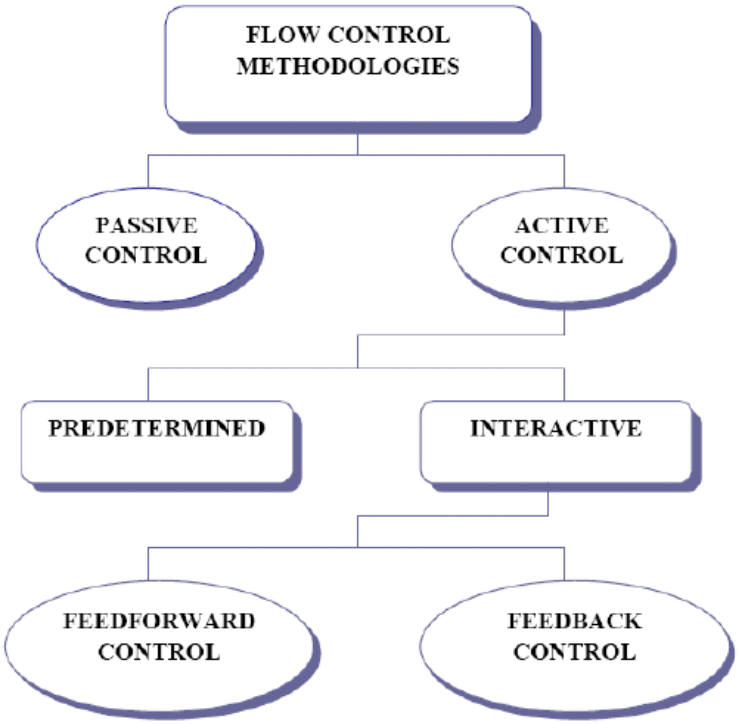

Figure 2.12: Classification of flow control methods (Jahanmiri, 2010)

Flow control can be defined as the ability to manipulate a flowfield to produce a desired change, and it is generally classified into active and passive control of the flow structures (Gad-el-Hak, 2000). The concept of flow control dates back to Prandtl (1904) when he first discovered the concept of a boundary layer (Barnwell & Hussaini, 2012). A comprehensive

review and analysis on active flow control has been provided by Jahanmiri (Jahanmiri, 2010).

Active flow control requires some form of energy input in order to manipulate the flow structures over the wing. Active flow control schemes are further divided into predetermined and interactive methods. Predetermined control loops refer to steady or unsteady energy inputs without consideration for the state of the flowfield, and thus sensors are not required for this method. In reactive scheme, sensors are used continuously to adjust the controller or energy input. The control loop for interactive scheme can either be feed forward (open) or feedback (closed) loop as shown in Figure 2.12. In feed forward loop, the sensors are placed upstream of the controller (Jahanmiri, 2010). In past active flow control concepts of various types have been used that can successfully improve the aerodynamic characteristics of air vehicles. Efforts to control the structure and trajectory of leading edge vortices on swept flying wings, using active flow control approaches, have included suction and blowing at the leading edges (Joslin, Miller, & Lu, 2000). Active flow control methods to control the leading-edge vortices and vortex break breakdown for improved aerodynamics of swept wing vehicles have been described by Gursul (Gursul et al., 2007) and Nathan (Nathan, Zhijin, & Ismet, 2008).

Passive flow control does not require energy input and any feedback mechanism (Gad-el-Hak, 2000). This method of flow control remains the most used mode of flow control to this day. Vortex generators, for example, are currently employed on the wings of most Boeing aircrafts in order to control the flow separation on the wings (Gad-el-Hak, 2000). In past, passive flow control method has been applied by adding control surfaces to the wing such as canards, flaps, barriers and leading edge fences (Buchholz & Tso, 2000); (J.D.

Anderson, 2010); (Gudmundsson, 2014b). In present study, however, it is not feasible to add such control surfaces due to their adverse effect on Radar Cross Section (RCS) signature of flying wing configurations. As a result, novel flow control mechanisms must be investigated in order to manipulate the flowfield structures over flying wing without leading to the loss of control of the air vehicle. The challenge is to achieve that change with a simple device that is inexpensive to build and operate, and has minimum side effects with respect to RCS signature.

2.3.1 Radar Cross Section

Radio detection and ranging commonly known as Radar, transmits radio waves to detect the presence of an aircraft and find its position. The principle of the radar is that a transmitter sends out radio signals which are reflected back to the source or a receiver when an object is encountered (Kingsley & Quegan, 1992). When transmitter and receiver are located on same platform and share the antenna, the radar is called monostatic. The radar is referred as bistatic, when radar transmitter and receiver are at two different locations.

Although stealth aircraft is not completely invisible to radar, but to remain undetected the aircraft must be designed with the smallest possible Radar Cross Section (RCS) signature, so that its return is below the detection threshold of the radar (Jenn, 1995). RCS is a measure of how detectable an aircraft is when encountered by the radio signals. Radar cross section of an aircraft can be minimised by planform alignment and materials selection for the airframe (Coppin, 2014). The planform alignment is an airframe design strategy in which leading and trailing edges are aligned in a particular direction in order to direct radar

energy away from the source into the space. The planform alignment or shaping of a stealth aircraft is generally considered to be most important line of RCS control (Bertin, 2002); (Coppin, 2014). The shaping of aerial vehicles under discussion leads to unconventional planform shapes that are associated with the term stealth. As noted earlier, the stealth designs are aerodynamically unstable, as vertical tails and conventional control surfaces are absent from these aerial vehicles (Schütte et al., 2012). For the aircraft with curved or perpendicular surfaces, the returns to the source will be strong (Coppin, 2014). An example of this phenomena is shown in Figure 2.13 where a conventional fighter aircraft is compared with two stealth UCAVs.

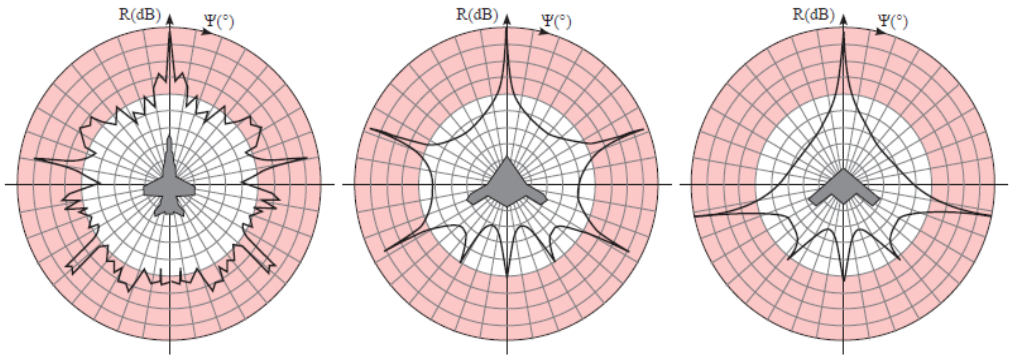

Figure 2.13: Radar Cross Section signature at 9GHz (a) F-18E Super Hornet, (b) Northrup Grumman X-47B and (c) Generic 40° Swept UCAV (Johnston, July 2012)

It can be seen that edge aligned planforms have much lower broadband response, and reflections from UCAVs take the form of spikes. The other way of minimising RCS signature of aircraft is by using Radar Absorbing Materials (RAM). The materials in question absorb and attenuate radar energy rather than reflecting it out to space (Jenn, 1995); (Coppin, 2014).

2.3.2 High Lift Devices

Devices or modifications to the wing that increase maximum lift coefficient and stall angle of the aerofoil are called high lift devices (J.D. Anderson, 2010). Air vehicles use various high lift devices to increase landing and take-off performance of the aircraft. High lift devices allow the air vehicle to operate at stall speeds during landing and take-off, resulting in shorter runway requirements. The stall speed of air vehicle is the lowest speed at which controllable flight can be sustained (Shevell, 1989); (Gudmundsson, 2014b). Therefore, objective is to reduce stall speed as much as possible when designing a wing. This can be achieved by increasing the camber of the wing and delaying flow separation by adding energy to the boundary layer (Bertin, 2002); (Moran, 2012); (Rathakrishnan, 2013) (Schlichting, Gersten, Krause, Oertel, & Mayes, 1960).

There are two types of high lift devices: passive and active. Passive high lift devices do not require any form of energy input where as active devices do (Gudmundsson, 2014b). In this study, only passive high lift devices are considered, and they can be further divided into leading and trailing edge devices. The most common trailing edge device is the wing flap and most common leading edge devices are believed to be slots and slats (J.D. Anderson, 2010); (Kundu, 2014). The leading-edge devices can increase the maximum lift coefficient and stall angle without significantly altering the lift curve (Houghton & Carpenter, 2003); (Kermode, 2012). Leading-edge slots are discussed in more detail in Chapter 6 of this thesis. The slots in this study were used for the purpose of passive flow control to maximise the performance of control surfaces, and not to increase the maximum lift coefficients. It should be noted that leading-edge device will not increase the lift of the wing unless flow can be made to follow the curvature of the geometry. The effectiveness of a leading-edge

slot is therefore highly dependent on the geometry of the wing and the leading-edge device mounted on the wing (Gudmundsson, 2014b).

Trailing edge high-lift device increases the maximum lift coefficient of wing by increasing the camber, but this usually results in reduction of stall angle as well (Kermode, 2012); (Gudmundsson, 2014b). Some of the common trailing edge flaps include plain flap, split flap, external flap, single-slotted flap, double-slotted flap, fowler flap and Gurney flap. The performance of these trailing edge devices has been comprehensively reviewed by Gudmundsson (Gudmundsson, 2014b). In this study, trailing edge flaps were mounted and computationally analysed on a moderately swept flying wing configuration and comparison was made with a clean model in Chapter 5 of the thesis. Flying wings do not use horizontal stabiliser, and therefore combine the functions of elevators and ailerons into one set of flight control. For a flying wing, control surfaces on the trailing edge of the wing deflect up or down at the same time like an elevator to provide pitch control, and they are also able to move in an opposite direction to each other like ailerons to give roll control to a flying wing (J.D. Anderson, 2010).

2.4. Role of UAVs

Unmanned Aerial Vehicles (UAVs) can be defined as aircrafts that have the capability to fly either remotely or autonomously (B.S & Poondla, 2017). The UAVs can either be operated remotely with constant operator involvement, or they can be pre-programmed with a set of instructions to execute a mission autonomously without operator intervention. A completely autonomous UAV has the capability to fly without external involvement from take-off to landing. The pilot-in-command can, however, intervene by overriding the

autopilot in case of emergencies (Barnhart, 2012). The amount of system autonomy has huge effect on UAV development though, as project becomes more complex and expensive with increased autonomy of the air vehicle (Clark, 2000). It should be noted that UAVs under consideration in this study are designed to be returned and reused, and they do not have a human on board. The generic terms drone, remotely piloted vehicle (RPV) or remotely piloted aircraft (RPA) are sometimes used interchangeably for UAVs under discussion (Clark, 2000); (Barnhart, 2012).

Figure 2.14: Unmanned Air Vehicle Predator adapted to be used for military purposes (Barnhart, 2012)

UAVs have drawn a considerable interest in recent years due to their increased use for military and civilian tasks. The success of UAVs in combat areas was noted by various non-military agencies in mid 1990s, and applications were developed to allow unmanned aircraft to perform civilian missions at a fraction of cost in comparison to manned aircrafts (Barnhart, 2012). UAVs have several potential advantages over manned aircrafts. They can

be deployed in a high-risk environment without the need to risk a pilot's life. They are more cost effective in comparison to manned aircraft, as pilot and associated life support system is not required to operate such air vehicles (Clark, 2000). Moreover, they can perform manoeuvres that human pilots will not be able to withstand (Kermode, 2012).

Some UAVs such as Predator can be adapted for offensive use by fitting them with air-to-surface missile. The Predator, shown in Figure 2.14, was originally designed to carry out intelligence gathering, surveillance, and reconnaissance or ISR missions, but in recent years it has been adapted to deliver hellfire missiles on enemy targets (Barnard & Philpott, 2010); (Barnhart, 2012). Civilian applications of UAVs not only include surveillance but they are also being used for mapping, traffic monitoring, land resource management and so on (Barnard & Philpott, 2010).

There is no standard when it comes to classification of UAVs, but Keane (J. F. Keane & Carr, 2013) and Clark (Clark, 2000) divide them into following three categories: a) Pilotless aircrafts used for training personnel in air-to-air and surface-to-air targets are termed as Pilotless Target Aircrafts (PTA); b) Non-lethal pilotless aircrafts designed to be used for the purposes of intelligence, surveillance, and reconnaissance (ISR); c) Unmanned Combat Air Vehicles (UCAVs) designed to strike the enemy defences and provide lethal ISR services (J. F. Keane & Carr, 2013). It should be noted that flying wing vehicles being investigated in this study are of last category. Such air vehicles are currently used in stealth technology as their flat surfaces, high wing sweep and sharp edges help reduce the radar signature (Bertin, 2002); (Schütte et al., 2012). The concept of a UCAV is to a design a system for the delivery of an offensive weapon in combat situations, as opposed to mounting weapon on a system that was designed for another purpose. Several UCAV designs are currently in use

such as Boeing X-45A, Northrop Grumman X-47B, BAE Systems Taranis (Barnhart, 2012). Some of the roles of modern UCAVs include flying surveillance missions, strike and suppression of enemy defences, bomb damage assessment and so on (Clark, 2000).

Aviation technology has made great leaps in mechanics, structures, materials, and power delivery in last 20 years (Barnhart, 2012). UCAV research has benefited from these advancements but technical and aerodynamic challenges associated with low observable air vehicles remain considerable (Lee, 2014); (Clark, 2000). The integration of mature technologies into UCAV operational system, and making close-hand technologies affordable are two great challenges in the developments of future UCAVs (Clark, 2000).

The UCAV market is anticipated to experience strong growth in the coming years. A team of market research analysts, Teal Group Corporation, has predicted that UAV sector of aerospace is going to be most dominant sector in terms of growth, with expenditures expected to grow substantially (Barnhart, 2012).

2.5. Computational Aerodynamics

With the emergence of a high speed digital computer combined with the development of numerical algorithms have radically changed the way aerodynamics is practiced in this day and age (Cummings, 2015). Historically, aerodynamics revolved in two dimensional worlds of theory and experiment, but Computational Aerodynamics (CA) incorporates a new third approach in the study of aerodynamics, and has become an equal partner with pure theory and experiment in the resolution of aerodynamic problems. When computations are carried out in parallel with experiments, they assist to interpret the physical experiments

and also establish the validity of experimental data. Numerical computations provide a new dimension in the analysis and solution of aerodynamic problems, and moreover they are more cost effective than laboratory experiments. One of the early achievements of Computational Aerodynamic methods was with NASA's aircraft called HiMAT. Wind tunnel tests had established that HiMAT would have unacceptable drag levels at speeds of Mach 1. If NASA had redesigned HiMAT using wind tunnels, the cost would have amounted to $150,000, and additionally it would have delayed the project. The wings of aircraft were redesigned using a computer program at the cost of $6000, saving NASA substantial amount of money and time (John D. Anderson, 1995).

The process of aircraft design can be aided using numerical methods by focusing on smaller elements of aircraft such as flow over an aerofoil with a control surface, and internal flows such as compressors, burners, turbine blades and so on. The usefulness of such flows is that it can show flow imperfections in a localised region, which can then be rectified by modifying the design. The amount of wind tunnel testing for the development of novel designs has been greatly reduced with the advent of computational aerodynamics, as computer programs can be used to test design options and parameters of aircrafts (Pozrikidis, 2017); (Cummings, 2015).

Although aerodynamic predictions have become increasingly accurate and fast using numerical methods, but computational burden on computing resources is still remarkably high due to the large number of variables required for the analysis of full aircraft configurations (Coppin, 2014). Therefore, depending on the complexity of a flowfield and accuracy required, correct computational approach should be implemented to reduce computational costs and time. The discipline of Computational Aerodynamics is generally

divided into linear and non-linear methods. Linear methods are less computer intensive, and they require a solution of large system of linear equations that would be too laborious to solve otherwise (Moran, 2012). Panel Method and Vortex Lattice Method are two widely known linear techniques for aeronautical applications.

As computer processing speeds and memory became faster and bigger, engineers soon began to solve more difficult non-linear problems in fluid dynamics. This gave rise to whole new discipline – Computational Fluid Dynamics (CFD), which has become a leading method in the prediction and solution of aerodynamic problems (Cummings, 2015). The major target of CFD process is to enhance design process of any problem that deals with fluid flow, therefore CFD codes are structured around the numerical algorithms that can solve all kind of fluid flow problems not just aerodynamic problems (Pozrikidis, 2017). Today CFD has found its applications in range of Engineering disciplines including automobile and engine, industrial manufacturing, civil engineering, environmental engineering, naval architecture and so on (John D. Anderson, 1995).

There are several schemes within CFD codes that can be used to solve and analyse fluid dynamic problems. Euler, Steady-State RANS and time dependent RANS are most notable and widely used schemes for aerospace applications (Zikanov, 2010). More recently, however, computational intensive techniques, such as Detached Eddy Simulation (DES), Large Eddy Simulation (LES) and Direct Numerical Simulation (DNS) have surfaced in the research sector and industry (Wilcox, 1994); (Versteeg & Malalasekera, 2007). The choice of any of these schemes is based upon the physics of flowfield in question, the accuracy of solution required and the resources at hand in terms of computational time and cost. Therefore, correct method of computational analysis should be adopted to reduce

computational time and cost for the resolution of aerodynamic problems. In this study, Vortex Lattice Method (VLM), Euler and RANS approaches were used to analyse and validate the experimental data of clean and cavity wings.

2.6. Computational Fluid Dynamics

All of the fluid dynamics is based upon fundamental governing principles of continuity, momentum and energy equations (Versteeg & Malalasekera, 2007). These physical principles can be described as: a) Principle of conservation of mass i.e. the mass of fluid is conserved; b) The rate of change of momentum equals the sum of the forces on a material element (Newton's second law); c) Principle of conservation of Energy i.e. energy is conserved (the first law of thermodynamics) (Versteeg & Malalasekera, 2007). The physical principles under discussion represent mathematical statements of conservation laws and can be written as follows (John D. Anderson, 1995):

Continuity Equation

$$\frac{\partial \rho}{\partial t} + \nabla \cdot (\rho V) = 0 \qquad \textbf{(2.3)}$$

Where: $V = (u, v, w)$. Therefore u is x component of velocity, v is y component of velocity and w is z component of velocity.

In Cartesian coordinates, the vector operator ∇ is described as

$$\nabla \equiv i\frac{\partial}{\partial x} + j\frac{\partial}{\partial y} + k\frac{\partial}{\partial z} \tag{2.4}$$

Momentum Equations

x Component:

$$\frac{\partial(\rho u)}{\partial t} + \nabla \cdot (\rho u V) = -\frac{\partial p}{\partial x} + \frac{\partial \tau_{xx}}{\partial x} + \frac{\partial \tau_{yx}}{\partial y} + \frac{\partial \tau_{zx}}{\partial z} + \rho f_x \tag{2.5}$$

y Component:

$$\frac{\partial(\rho v)}{\partial t} + \nabla \cdot (\rho v V) = -\frac{\partial p}{\partial y} + \frac{\partial \tau_{xy}}{\partial x} + \frac{\partial \tau_{yy}}{\partial y} + \frac{\partial \tau_{zy}}{\partial z} + \rho f_y \tag{2.6}$$

z Component:

$$\frac{\partial(\rho w)}{\partial t} + \nabla \cdot (\rho w V) = -\frac{\partial p}{\partial z} + \frac{\partial \tau_{xz}}{\partial x} + \frac{\partial \tau_{yz}}{\partial y} + \frac{\partial \tau_{zz}}{\partial z} + \rho f_z \qquad \textbf{(2.7)}$$

Energy Equation

$$\begin{aligned}\frac{\partial}{\partial t}\left[\rho\left(e + \frac{V^2}{2}\right)\right] + \nabla \cdot \left[\rho\left(e + \frac{V^2}{2}\right)V\right] \\ = \rho\dot{q} + \frac{\partial}{\partial x}\left(k\frac{\partial T}{\partial x}\right) + \frac{\partial}{\partial y}\left(k\frac{\partial T}{\partial y}\right) + \frac{\partial}{\partial z}\left(k\frac{\partial T}{\partial z}\right) - \frac{\partial(up)}{\partial x} \\ - \frac{\partial(vp)}{\partial y} - \frac{\partial(wp)}{\partial z} + \frac{\partial(u\tau_{xx})}{\partial x} + \frac{\partial\left(u\tau_{yx}\right)}{\partial y} + \frac{\partial(u\tau_{zx})}{\partial z} \\ + \frac{\partial\left(v\tau_{xy}\right)}{\partial x} + \frac{\partial\left(v\tau_{yy}\right)}{\partial y} + \frac{\partial\left(v\tau_{zy}\right)}{\partial z} + \frac{\partial(w\tau_{xz})}{\partial x} + \frac{\partial\left(w\tau_{yz}\right)}{\partial y} \\ + \frac{\partial(w\tau_{zz})}{\partial z} + \rho f \cdot V\end{aligned} \qquad \textbf{(2.8)}$$

In the above equation, k is the term for thermal conduction, $\dot{q}$ is the rate of volumetric heat addition per unit mass, T is the temperature and E is the total energy given as follows (Versteeg & Malalasekera, 2007):

$$E = e + \frac{1}{2}(u^2 + v^2 + w^2) \tag{2.9}$$

Total enthalpy H is defined as

$$H = E + \frac{p}{\rho} \tag{2.10}$$

For Newtonian fluids, shear stress in a fluid is proportional to the time rate of strain or velocity gradient (Andersson, 2012). The stress tensor for Newtonian fluids can be described by the following equations

$$\tau_{xx} = 2\mu\frac{\partial u}{\partial x} + \lambda\left(\frac{\partial u}{\partial x} + \frac{\partial v}{\partial y} + \frac{\partial w}{\partial z}\right) \tag{2.11}$$

$$\tau_{yy} = 2\mu\frac{\partial v}{\partial y} + \lambda\left(\frac{\partial u}{\partial x} + \frac{\partial v}{\partial y} + \frac{\partial w}{\partial z}\right) \tag{2.12}$$

$$\tau_{zz} = 2\mu\frac{\partial w}{\partial z} + \lambda\left(\frac{\partial u}{\partial x} + \frac{\partial v}{\partial y} + \frac{\partial w}{\partial z}\right) \quad \textbf{(2.13)}$$

$$\tau_{xy} = \tau_{yx} = \mu\left(\frac{\partial u}{\partial y} + \frac{\partial v}{\partial x}\right) \quad \textbf{(2.14)}$$

$$\tau_{yz} = \tau_{zy} = \mu\left(\frac{\partial v}{\partial z} + \frac{\partial w}{\partial y}\right) \quad \textbf{(2.15)}$$

$$\tau_{zx} = \tau_{xz} = \mu\left(\frac{\partial w}{\partial x} + \frac{\partial x}{\partial z}\right) \quad \textbf{(2.16)}$$

According to stokes hypothesis (John D. Anderson, 1995)

$$\lambda = -\frac{2}{3}\mu \quad \textbf{(2.17)}$$

In above equations μ represents the laminar viscosity which can be determined by using Sutherland's law as follows (Wilcox, 1994)

$$\frac{\mu}{\mu_0} = \left(\frac{T}{T_0}\right)^{\frac{3}{2}} \frac{T_0 + 110}{T + 110} \quad \textbf{(2.18)}$$

In the above equation, reference values are specified as μ_0 = 1.78.10^{-5}kg/ms and T_0 = 288.16K. The heat flux vector components are calculated using the following expressions

$$q_x = -k\frac{\partial T}{\partial x} = -\frac{1}{(\gamma - 1)M_\infty^2}\frac{\mu}{P_r}\frac{\partial T}{\partial x} \quad \textbf{(2.19)}$$

$$q_y = -k\frac{\partial T}{\partial y} = -\frac{1}{(\gamma - 1)M_\infty^2}\frac{\mu}{P_r}\frac{\partial T}{\partial y} \quad \textbf{(2.20)}$$

$$q_z = -k\frac{\partial T}{\partial z} = -\frac{1}{(\gamma - 1)M_\infty^2}\frac{\mu}{P_r}\frac{\partial T}{\partial z} \quad \textbf{(2.21)}$$

In above equations, P_r represents the Prandtl number and M_∞ is the freestream Mach number. The thermal conductivity k is represented by the following equation

$$P_r = \frac{\mu C_p}{k} \qquad \textbf{(2.22)}$$

Energy equation can be dropped when no heat transfer is involved in the flow and compressibility effects can safely be neglected. Compressibility effects are detected in flows at high speeds or for flows where large pressure fluctuations are present (Abbott & Basco, 1989).

The shear stress in the fluid is caused by friction between fluid particles due to viscosity and is defined as the product of viscosity (μ) times the velocity gradient (Petrila & Trif, 2005). Although, influence of viscosity becomes smaller for the part of flow further away from the solid surface, but in real world there are no fluids with zero viscosity. There are, however, examples where product of shearing velocity gradient and viscosity is adequately small to neglect the shear stress terms from Navier-Stokes equations (Bertin, 2002). A viscous flow has transport phenomena of friction and thermal conduction present in it. This phenomena increases the entropy of the flow as it is dissipative in nature (John D. Anderson, 1995). The equations that have been presented up to this point in this chapter apply to such viscous flows.

If viscous and thermal conduction terms are omitted from governing equations, the Navier-Stokes equations reduce to the Euler equations. By definition, a flow where viscous

transport phenomena, dissipation and thermal conductivity are neglected is called inviscid flow (Abbott & Basco, 1989). Continuity equation remains identical but momentum and energy equations reduce to the following (John D. Anderson, 1995):

Momentum Equations

x Component:

$$\frac{\partial(\rho u)}{\partial t} + \nabla \cdot (\rho u V) = -\frac{\partial p}{\partial x} + \rho f_x \qquad \textbf{(2.23)}$$

y Component:

$$\frac{\partial(\rho v)}{\partial t} + \nabla \cdot (\rho v V) = -\frac{\partial p}{\partial y} + \rho f_y \qquad \textbf{(2.24)}$$

z Component:

$$\frac{\partial(\rho w)}{\partial t} + \nabla \cdot (\rho w V) = -\frac{\partial p}{\partial z} + \rho f_z \qquad \textbf{(2.25)}$$

Energy Equation:

$$\frac{\partial}{\partial t}\left[\rho\left(e + \frac{V^2}{2}\right)\right] + \nabla \cdot \left[\rho\left(e + \frac{V^2}{2}\right)V\right] = \rho\dot{q} - \frac{\partial(up)}{\partial x} - \frac{\partial(vp)}{\partial y} - \frac{\partial(wp)}{\partial z} + \rho f \cdot V \qquad \textbf{(2.26)}$$

In Euler equations, fluid is assumed to be inviscid and therefore it does not stick to the wall, making slip condition feasible. This makes Euler equations suitable for compressible flows at high Mach numbers. At higher Mach numbers, boundary layer is constrained to a very small region adjacent to the solid surface where viscous and turbulence effects are important. Therefore, such flows are often well predicted with the Euler equations (Ferziger & Peric, 1999); (John D. Anderson, 1995).

In this study, Euler and RANS methods are compared for the investigations of baseline clean configurations. It has been reported by the researchers that Euler based methods are

not adequate to consistently capture the flow separation from sharp leading edges of delta wings (Fujii, Gavali, & Holst, 1988); (Görtz, 2005); (Crippa, 2008). In contrast, RANS results were found to be more realistic and produced better agreement with the experiment for the vortex separated flows of flying wing configurations.

2.6.1 Reynolds Averaged Navier Stokes Equations

All types of flows, whether they are two dimensional or more complicated three dimensional, become unstable above a certain Reynolds number (Versteeg & Malalasekera, 2007). A Reynolds number is described as:

$$Re = \frac{\rho v L}{\mu} \qquad (2.27)$$

Where v is mean velocity of the fluid, L is characteristic length, ρ is density of the fluid and μ is dynamic viscosity. It should be noted that Reynolds numbers in this study are based on the chord lengths of the configurations being investigated. It has been established in experiments that flow remains laminar at the values below critical Reynolds number (Re_{crit}) and becomes turbulent above Re_{crit}. It has been established that a complicated series of events take place at values above critical Reynolds number leading to a radical change in flow physics. This change in flow character results in a turbulent flow, making the flow

variables such as velocity and pressure to fluctuate in an irregular and chaotic manner (Versteeg & Malalasekera, 2007).

If a velocity measurement is made at a typical point in the turbulent flow with a hot-wire anemometer, or local pressure measurement is made with a small transducer, the flow variables might display a pattern shown in Figure 2.15. The velocity can be decomposed into a mean value U with a fluctuating component $u'(t)$ superimposed on it as shown in Figure 2.15 (Versteeg & Malalasekera, 2007). In Figure 2.15, $u(t)$ is time history of velocity vector, U is mean velocity of fluid, implying that equations derived for computing this quantity are independent of time, and $u'(t)$ is the fluctuating component of the velocity. Therefore, velocity can be calculated using the following equation

$$u(t) = U + u'(t) \qquad \textbf{(2.28)}$$

The turbulent flow can thus be decomposed into mean values of flow variables and their fluctuating components. Pressure and other flow variables can also be decomposed using this process which is known as Reynolds decomposition or Reynolds Averaging. The averaging of governing equations can be conventional Reynolds Averaging for incompressible flows or Favre (density) averaging for compressible flows (Versteeg & Malalasekera, 2007).

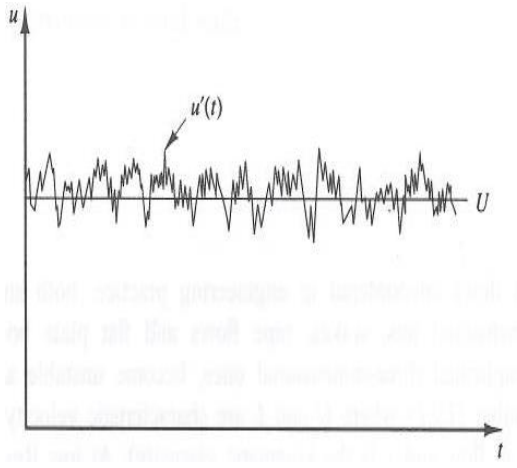

Figure 2.15: Typical point velocity measurement in turbulent flow (Versteeg & Malalasekera, 2007)

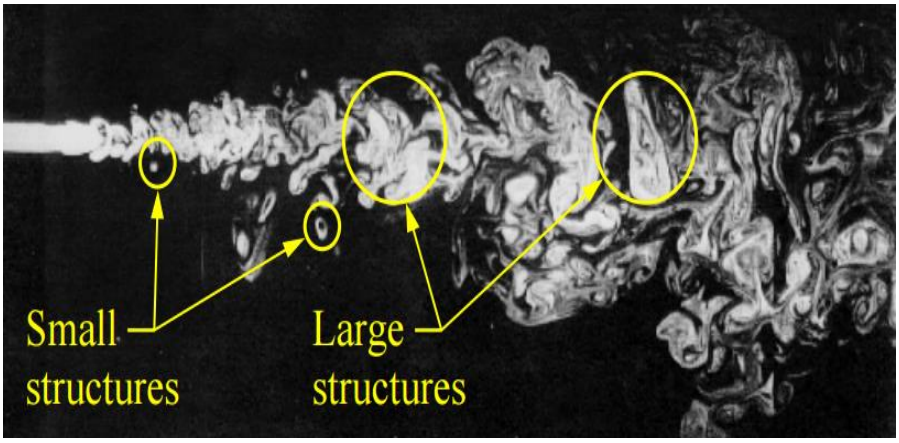

Figure 2.16: Visualisation of turbulent flow structures (Versteeg & Malalasekera, 2007)

An ordinary turbulent flow contains rotational flow structures, known as turbulent eddies, with a wide range of length scales as shown in Figure 2.16. The nonlinearity of governing equations leads to interactions between range of length scales present in a turbulent flow (Wilcox, 1994). Large turbulent scales in the flow contain the bulk of the energy, and they hand down kinetic energy to smaller and smaller eddies in a process called energy cascade

(Versteeg & Malalasekera, 2007); (Wilcox, 1994). The smallest scales, termed as Kolmogorov scales, are influenced by the viscosity, while large energetic eddies are effectively inviscid. At the micro level, energy associated with Kolmogorov scales is dissipated and converted into thermal internal energy (Versteeg & Malalasekera, 2007).

Direct Numerical Simulation (DNS) method is the most accurate method of modelling where time dependent governing equations are solved on grids that are adequately fine to resolve the Kolmogorov length scales at which dissipation take place. Therefore, time step in DNS method has to be sufficiently small in order to capture the fastest of fluctuations within turbulent flow. DNS provides most accurate results when computing turbulence, but at the expense of extremely high computational workload (Wesseling, 2010); (Versteeg & Malalasekera, 2007).

To use governing equations in their entirety, the distance between grid points and time step of computation have to be sufficiently small in order to resolve all the length scales down to Kolmogorov scales within a turbulent flow (Versteeg & Malalasekera, 2007). It is neither feasible nor desirable to resolve all the fluctuation details in majority of flows encountered in engineering (Versteeg & Malalasekera, 2007), therefore an approximation to the turbulent nature of the flow needs to be introduced. A computationally lighter alternative to DNS is to use LES or RANS turbulence modelling. All forms of turbulence modelling currently involve some form of decomposition of dependent variables to represent the physical situation. For RANS method, flow quantities of interest are time averaged, resulting in mean quantities with extra terms involving the fluctuating quantities (Bertin, 2002). When equations obtained from Reynolds decomposition are substituted

into instantaneous Navier-Stokes equations for time averaging, we obtain the following form for continuity and x component of momentum equations respectively:

$$\frac{\partial \bar{\rho}}{\partial t} + \nabla(\bar{\rho}V) = 0 \qquad \textbf{(2.29)}$$

$$\frac{\partial(\bar{\rho}\bar{u})}{\partial t} + \nabla(\bar{\rho}\bar{u}V) = -\frac{\partial \bar{p}}{\partial x} + \nabla(\mu\nabla\bar{u}) + [-\frac{\partial\left(\overline{\bar{\rho}u'^2}\right)}{\partial x} - \frac{\partial(\overline{\bar{\rho}u'v'})}{\partial y} - \frac{\partial(\overline{\bar{\rho}u'w'})}{\partial z} \qquad \textbf{(2.30)}$$

These equations are known as Reynolds-Averaged Navier-Stokes (RANS) equations. Time-averaging process have introduced Reynolds stresses terms $\rho\overline{u'v'}$. This nonlinear Reynolds stress term requires additional modelling to close the governing equations, and therefore has led to the formulation of turbulence models (Lomax, Pulliam, & Zingg, 2011); (Chen, 1997).

2.6.2 Turbulence Modelling

Turbulence modelling is an area where a mathematical model is used as an alternative to time dependent governing equations to predict the effects of turbulence (Versteeg & Malalasekera, 2007). As noted earlier, in majority of engineering problems it is impractical and unnecessary to resolve all the length scales in a turbulent flow. RANS methods have been providing satisfactory results to researchers and engineers for fluid dynamic

problems. Therefore, most of the computations in the past have been carried out using RANS method, and this trend is likely to continue for the foreseeable future (Versteeg & Malalasekera, 2007). It is, however, vital to account for the effects of turbulence on mean flow because time-averaging process eliminates all the fluctuation details in a turbulent flow, and those details must be modelled with a turbulence model (Abbott & Basco, 1989); (Versteeg & Malalasekera, 2007).

Number of transport equations	**Turbulence model**
Zero	Mixing Length model
One	Spalart-Allmaras model
Two	$k-\varepsilon\, model$ $k-\omega\, model$ Algebraic model
Seven	Reynolds stress model

Table 2.1: Number of transport equations solved for RANS turbulence models

A turbulence model is a computational procedure to close the system of RANS equations so that variety of flow problems can be calculated. The most common turbulence models include mixing length models (Cebeci & Smith, 1974); k-ε models (Launder & Spalding, 1974); Reynolds stress equation models (Launder et al, 1975) and algebraic stress equation models (Demuren & Rodi, 1984). RANS turbulence models are categorised on the basis of the additional transport equations that need to be solved in conjunction with RANS flow equations. The most common turbulence models used for RANS computations are shown in Table 2.1 (Versteeg & Malalasekera, 2007).

Large Eddy Simulations (LES) approach is an intermediate form of turbulence calculations method, where time dependent equations are solved to resolve the large eddies in the flow and effects of smaller eddies are modelled (Versteeg & Malalasekera, 2007); (Wilcox, 1994). The effects of unresolved eddies are included in the computations by means of sub-grid scale turbulence model. As unsteady equations are required to be solved, therefore demand on computing resources in terms of storage and volume of calculations is considerably higher than RANS computations, but this approach has started to be used for CFD problems with complicated geometries (Versteeg & Malalasekera, 2007).

In contrast to the methods mentioned above, DNS approach requires no turbulence modelling. In this method, unsteady governing equations are solved on a grid that is sufficiently fine to resolve the Kolmogorov length scales at which energy dissipation occurs. Moreover, the time step of the computations is sufficiently small to resolve the period of the fastest fluctuations (Wilcox, 1994); (Wesseling, 2010); (Versteeg & Malalasekera, 2007). Modern CFD packages have number of RANS turbulence models to choose from, but no single turbulence model is universally accepted for all class of problems (Pozrikidis,

2017); (J. F. Thompson, Warsi, & Mastin, 1985). In this study Spalart-Allmaras (SA) model was used, because it provided best results for the problem at hand and is the most popular approach for external aerodynamic flow simulations. The constants of the model have been specifically tuned for external aerodynamic flows, therefore it has shown good results in predicting stalled flows and provides economical computations of boundary layers. SA is a one equation turbulence model that solves one turbulent transport equation in conjunction with RANS equations, and it was specifically developed for external aerodynamic flow applications. Multi-equation models solve two or more additional equations, thereby adding complexity when model is implemented in CFD solver. Moreover, multiple equation turbulence models are computationally more expensive, as additional equations require extra time for the solution to converge (Chen, 1997); (Versteeg & Malalasekera, 2007). The advantage of using SA turbulence model is that it solves only one transport equation for the kinematic eddy viscosity as is shown in Table 2.1. The dynamic eddy viscosity (μ_t) in one equation turbulence model can be related to kinematic viscosity ($\tilde{v}$) by the following equation:

$$\mu_t = \rho \tilde{v} f_{v1} \qquad \textbf{(2.31)}$$

The equation above entails a wall damping function (f_{v1}), which goes to zero at the wall. The Reynolds stresses in SA turbulence can be written in x direction as:

$$\pi = (-\rho\overline{u'u'} - \rho\overline{u'v'} - \rho\overline{u'w'} \qquad \textbf{(2.32)}$$

$$= (\rho\tilde{v}f_{v1}\left(\frac{\partial\bar{u}}{\partial x} + \frac{\partial\bar{u}}{\partial x}\right), \rho\tilde{v}f_{v1}\left(\frac{\partial\bar{u}}{\partial y} + \frac{\partial\bar{v}}{\partial x}\right), \rho\tilde{v}f_{v1}\left(\frac{\partial\bar{u}}{\partial z} + \frac{\partial\bar{w}}{\partial x}\right))$$

The equations for y and z can be written similarly. The transport equation for eddy viscosity is as follows:

$$\frac{\partial(\rho\tilde{v})}{\partial t} + \nabla(\rho\tilde{v}U)$$

$$= \frac{1}{\sigma_v}\nabla[(\mu + \rho\tilde{v})\nabla(\tilde{v}) + C_{b2}\rho\nabla\tilde{v}.\nabla\tilde{v}] + C_{b1}\rho\tilde{v}\widetilde{\Omega}$$

$$- C_{w1}\rho\left(\frac{\tilde{v}}{Ky}\right)^2 f_w \qquad \textbf{(2.33)}$$

Where $\widetilde{\Omega}$ is the mean vorticity tensor and y is distance to solid wall

The model constants are given as:

$\sigma_v = \frac{2}{3}$	K = 0.4187	$C_{b1} = 0.1355$	$C_{b2} = 0.622$	$C_{w1} = C_{b1} + K^2\frac{1 + C_{b2}}{\sigma_v}$

The SA turbulence model has attracted growing interest in turbo-machinery applications due to its suitability for aerofoil problems. The turbulence model, however, is not

considered appropriate for general internal flows and should be avoided for such flows (Versteeg & Malalasekera, 2007).

2.6.3 Near-Wall Turbulence

The flow physics of turbulent boundary layers become considerably more complex due to the presence of walls. The mean velocity is affected by the no-slip condition at the wall where the flow is reduced to laminar flow. The near wall zone requires many grid nodes to resolve the variations in flowfield because velocity and other transport properties vary rapidly a short distance from the wall (Pozrikidis, 2017); (Chen, 1997). Turbulent boundary layer along a wall has a substantial region of inertia-dominated flow far away from the wall, but close to the wall flow is influenced by the viscosity of fluid and is independent of freestream parameters (Versteeg & Malalasekera, 2007). At high Reynolds numbers, the viscous part of boundary layer becomes very thin, and as a result it is difficult to use enough grid points to resolve it. This problem can be avoided by using the wall functions that rely on law of the wall of turbulent boundary layer (Ferziger & Peric, 1999).

The mean velocity profile of a turbulent boundary layer cannot be predicted accurately by laminar shear stress relationship, as boundary layer is divided into different flow regions as shown in Figure 2.17. Each region within turbulent boundary layer has its own distinct characteristics (Moran, 2012). Furthermore, turbulent boundary layers are turbulent for most of their length (Massey & Ward-Smith, 2012). More detailed analysis has shown that effects of turbulence should be included in laminar stress-strain relationship to predict the velocity distribution profile of turbulent part of the boundary layer as is shown in equation below (Moran, 2012).

$$\tau = \mu \frac{\partial u}{\partial y} - \rho \overline{u'v'} \qquad \textbf{(2.34)}$$

Numerous experiments have confirmed that near wall region can be divided into outer and inner layers, shown in Figure 2.17. The inner region that accounts for 10-20% of the total thickness of wall layer can be further subdivided into three layers: laminar sublayer, buffer zone and log-law layer (Bertin, 2002). The quantity u^* that appears in Figure 2.17 is the friction velocity of the fluid that can be described by the following relationship:

$$u^* = \sqrt{\frac{\tau_w}{\rho}} \qquad \textbf{(2.35)}$$

In above equation τ_w is wall shear stress and ρ is density of the fluid. In laminar sublayer, the fluctuating components are forced to zero due to no-slip boundary condition at the wall. The behaviour of fluid in this region is dominated by the viscous effects and turbulent stresses are negligible (Versteeg & Malalasekera, 2007); (Moran, 2012); (Massey & Ward-Smith, 2012).

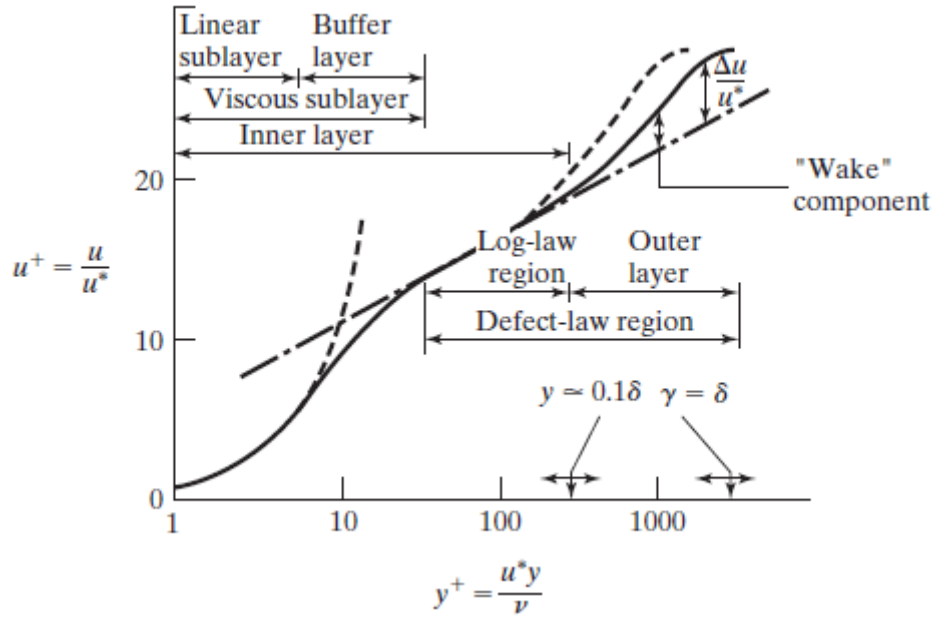

Figure 2.17: Structure of turbulent velocity distribution near a solid wall (Bertin, 2002)

The laminar sublayer is very thin (y^+ = 5-10), and it can be assumed that shear stress is approximately equal to wall shear stress τ_w throughout this region (Bertin, 2002). Therefore, laminar sublayer of the boundary layer can be evaluated as follows:

$$u^+ \equiv \frac{u}{u^*} \approx \frac{\rho u^* y}{\mu} \equiv y^+ \qquad \textbf{(2.36)}$$

The above equation is called law of the wall, and it contains definitions of two dimensionless parameters used in CFD (Versteeg & Malalasekera, 2007). In the equation, u^+ is dimensionless velocity and y^+ is dimensionless distance from the wall. As there is a

linear relationship between velocity and distance from the wall in laminar sublayer, the region is known as linear sublayer (Versteeg & Malalasekera, 2007); (Bertin, 2002).

There is an interim region between laminar sublayer and the inner layer, termed as buffer zone in Figure 2.17. This region provides a gradual transition from laminar to fully turbulent regime, therefore effects of viscosity and turbulence are equally important in this region (Versteeg & Malalasekera, 2007). Outside the laminar sublayer turbulent stresses dominate in log-law layer, therefore they must be included to correctly predict the velocity profile of turbulent part of boundary layer (Moran, 2012). By making an assumption regarding the length scale of turbulence, the standard form of log-law layer can be obtained as follows:

$$u^+ \equiv \frac{u}{u^*} = \frac{1}{k}\ln y^+ + C \qquad \textbf{(2.37)}$$

Numerical values for the constants are found from experiment, where $k = 0.4$ and $C = 5.5$ for smooth walls; wall roughness reduces the value of C. These values for constants are valid for all turbulent flows past smooth walls at high Reynolds numbers (Versteeg & Malalasekera, 2007). It should be noted that logarithmic scale of Figure 2.17 has considerably exaggerated the inner layer and laminar sublayer. The outer layer of the boundary layer profile accounts for 80% to 90% thickness (Bertin, 2002); (Moran, 2012). This outer region of inertia-dominated flows is far from solid boundary, and is free of direct viscous effects (Versteeg & Malalasekera, 2007).

The number of mesh points required to resolve all the details in a turbulent boundary layer can sometimes be too large. Therefore, wall functions can be used in CFD to bridge the regions between wall and fully turbulent flow when regions affected by fluid viscosity are not resolved by the mesh (Chen, 1997). Wall functions are set of semi-empirical formulas that describe the solution variables at near wall region and the corresponding quantities on the wall. The wall functions constitute law of the wall and near wall turbulent quantities formulas. If the value of y^+ is greater than 11.63, the first grid point is considered to be in the log-law region of a turbulent boundary layer. In this region, wall function formula in equation *(2.37*) that is associated with log-law is used to calculate the shear stress and other flow variables. However, when y^+ values are lower than 11.63 for grid points adjacent to wall, CFD applies the laminar stress-strain relationship described in equation *(2.36)* (Versteeg & Malalasekera, 2007).

2.7. Vortex Lattice Method

Vortex Lattice Method (VLM) is one of the earliest numerical methods in which computers were utilised to gain insight into the aerodynamics of an air vehicle. VLM is often used in early design phases as it can rapidly compute the aerodynamic forces and moments of an aircraft (Cummings, 2015). The VLM is a linear aerodynamic method that can only compute accurate solution of small to moderate angles of attack, and flows with low Mach numbers as compressibility effects are neglected in this method. The VLM represents the wing as a surface covered by a grid of quadrilateral panels with horseshoe vortex superimposed on each panel. In Figure 2.18, dashed lines define a panel on the wing and a single horseshoe vortex, represented by *abcd*, is superimposed on the panel. Ludwig Prandtl had used a

horseshoe concept for his lifting-line theory where he replaced a straight rectangular wing with a horseshoe vortex similar to one shown in Figure 2.18 (J.D. Anderson, 2010).

Biot-Savart law can be used to calculate induced velocity at control points of panels by treating each vortex filaments *ab, bc,* and *cd* separately (Bertin, 2002); (J.D. Anderson, 2010). A summation of all control points on the wing, and application of Neumann boundary condition results in a system of linear equations for the horseshoe vortex strengths. The strength of the vortices is linked to wing circulation and pressure difference between upper and lower surfaces of the wing. (Bertin, 2002).

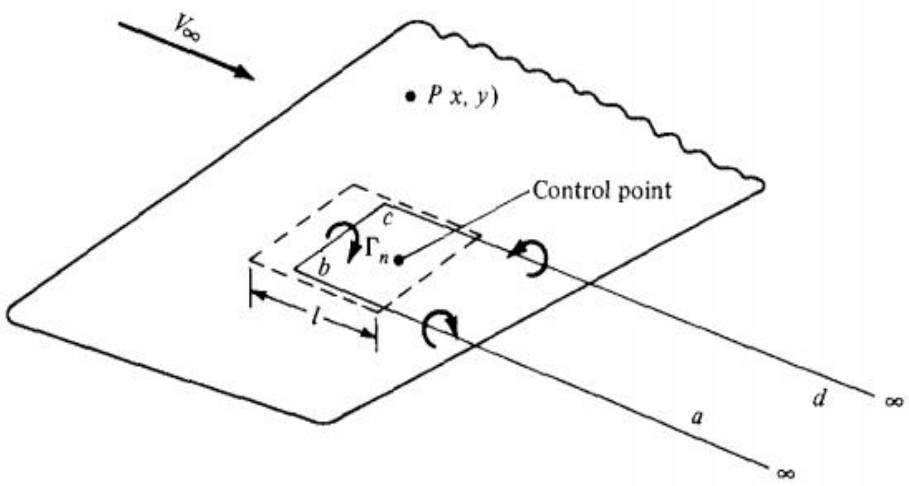

Figure 2.18: Single horseshoe vortex which is part of a vortex system on the wing (J.D. Anderson, 2010)

In a classical Vortex Lattice Method, a planform is divided into lattice of quadrilateral panels and horseshoe vortices are superimposed as shown in Figure 2.19. A bound vortex is placed on each panel, such that distance of this vortex is ¼ from front of the panel. A control point is placed on the centreline of each panel at a distance of ¾ from the front.

The strength of each vortex Γ_n is determined to satisfy the boundary conditions by solving a system of linear equations. This method assumes the flow to be steady, inviscid, incompressible, and attached to the surface of the wing. The vertical displacements occurring on wing or in wake are ignored with the exception of boundary conditions which are determined at control points (Cummings, 2015). The schematic of this implementation is shown in Figure 2.19.

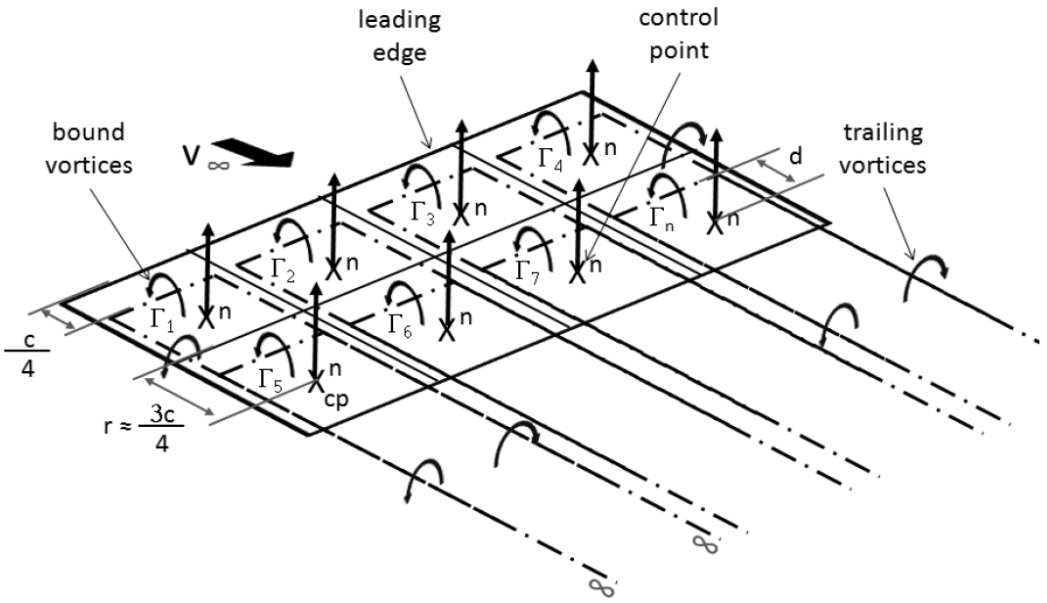

Figure 2.19: The horseshoe vortex layout for a Vortex Lattice Method (Schminder, 2012)

The entire wing is covered by horseshoe vortices, each with different unknown strength Γ_n, as displayed with dashed lines in Figure 2.19. The normal velocity induced by horseshoe vortices at each control point can be calculated using Biot-Savart law. When boundary condition of tangent flow at each control point on the wing is satisfied, a system of linear equations is produced which can be solved for unknown vortex circulation strengths Γ_n.

Then, lift is determined for each panel using the Kutta-Joukowski theorem of a vortex filament (J.D. Anderson, 2010).

According to Helmholtz vortex theorem, the strength of vortex filament is constant along its length and the vortex filament cannot end in the fluid. It must either extend to infinity or form a closed path (Shevell, 1989). The induced velocity of an infinite length of vortex filament strength Γ which represents lifting line surface located at ¼ chord location of the panel can be written as follows

$$U = \frac{\Gamma}{2\pi r} \tag{2.38}$$

Where r is radius of the line, Γ is field strength and U is induced velocity. When we consider a vortex filament with a finite length, the induced velocity can by defined by Biot-Savart law as follows (Bertin, 2002).

$$\overrightarrow{dV} = \frac{\Gamma_n(\vec{dl} \times \vec{r})}{4\pi r^3} \tag{2.39}$$

The equation above can be integrated to produce induced velocity of a vortex filament of finite length. The integrated equation is shown below and its nomenclature is described in Figure 2.20.

$$\vec{V} = \frac{\Gamma_n}{4\pi} \frac{\vec{r}_1 \times \vec{r}_2}{|\vec{r}_1 \times \vec{r}_2|^2} \left[\vec{r}_0 \cdot \left(\frac{\vec{r}_1}{r_1} - \frac{\vec{r}_2}{r_2} \right) \right] \quad \textbf{(2.40)}$$

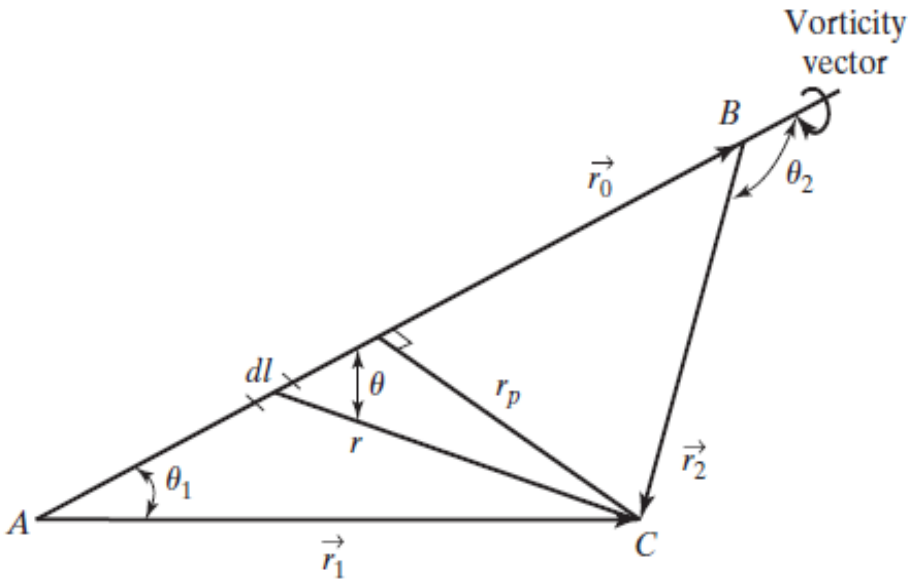

Figure 2.20: Nomenclature for calculating the velocity induced by a finite-length vortex filament (Bertin, 2002)

VLM method can be considered an extension of lifting line theory as wing of an arbitrary shape is divided into smaller panels in this method, and each panel is replaced with a horseshoe vortex of its own. Therefore, a system of linear equations is produced rather than one algebraic equation as is the case with lifting line theory (Liu, 2007). This results in better accuracy in determining the aerodynamic characteristics of configuration under study.

Lifting line theory is restricted to rather simple cases where sweep, dihedral angle or twist in the wing cannot be calculated. The VLM method, however, can take into account such geometrical deviations. The following system of linear equations is produced when the wings of arbitrary shape are divided into smaller panels (Melin, 2000).

$$\begin{bmatrix} w_{11} & w_{12} & . & . \\ w_{21} & .. & . & . \\ . & . & .. & . \\ . & . & . & w_{nn} \end{bmatrix} \begin{bmatrix} \Gamma_1 \\ . \\ . \\ \Gamma_n \end{bmatrix} = \begin{bmatrix} b_1 \\ . \\ . \\ b_n \end{bmatrix} \qquad \textbf{(2.41)}$$

In the equation above, gamma Γ is unknown vortex strength and w is induced velocity at each panel, b on the right side of equation is boundary condition which ensures no flow through condition on the wing surface. The values for vortex strength Γ is determined at each panel using linear equations in question (Melin, 2000). Then, Kutta-Joukowski theorem is applied to calculate the lift at each elemental panel. The Kutta-Joukowski theorem is defined as

$$L = \rho U_\infty \Gamma \qquad \textbf{(2.42)}$$

The overall lift on the wing can be obtained by adding the lift of each elemental panel, and as result lift coefficient can be derived from the lift of the wing (Bertin, 2002); (Melin, 2000).

2.8. Introduction to Optimisation

Optimisation can be described as a process which deals with finding the best result or optimum solution of a problem. In general terms, optimisation theory allows an Engineer to find a best result from a collection of alternatives without having to calculate all possible alternatives (Ravindran, Reklaitis, & Ragsdell, 2006); (Sundaram, 1996). Engineers are always confronted with optimisation problems where they need to balance performance with optimisation. Optimisation problems occur in most Engineering disciplines and some of the common examples of optimisation can include designing an aircraft for minimum weight and maximum strength, finding optimal trajectories of space vehicles, designing of pump and heat transfer equipment for maximum efficiency and so on (Chapra & Canale, 1985); (Arora, 2011).

There are four general approaches that can be used to optimise a system under study: Analytical methods, Graphical methods, Experimental methods and Numerical methods (Antoniou & Lu, 2007). Analytical methods which are based on conventional techniques of calculus cannot be applied to a highly non-linear problem or a problem with multiple parameters. A graphical method can only be used if the parameters or unknowns of the problem does not exceed two. For problems involving only one optimisation variable, the minimum or maximum of the objective function can simply be read from a graph. For most Engineering applications, however, the function to be optimised depends on more than two parameters. Thus, analytical and graphical methods are of limited usefulness for most

Engineering applications. The direct experimentation methods can be used to calculate an optimum performance of a system with several parameters, but this method becomes intractable and costly when all the parameters are adjusted one by one and the performance criterion for each case is measured. The most important approach to optimisation process is considered to be based on numerical methods. In this approach, an optimum solution is achieved by generating a series of progressively improved solutions of parameters of the given problem (Antoniou & Lu, 2007); (Nocedal & Wright, 1999). The major advancement in numerical methods occurred in the early fifties with the advent of a digital computer. As computers became faster and efficient, optimisation techniques advanced rapidly and considerable progress was accomplished in numerical algorithms. As a result of this progress, optimisation problems which were considered too cumbersome to solve only few years ago, can efficiently be solved using present day computing resources (Sundaram, 1996); (Cummings, Morton, & Siegel, 2008).

2.8.1 Optimisation Algorithms

The formulation of a numerical optimisation begins by identifying an objective function. The objective function is a quantitative measure of the performance of the system under investigation (Arora, 2011); (Alonso, LeGresley, & Pereyra, 2009); (Chapra & Canale, 1985). If numerical optimisation method is being used to maximise the heat transfer, we must be able to calculate heat transfer for different design configurations. The objective function depends on certain input parameters of the problem called variables or unknowns. The goal of numerical optimisation is to find the values of variables which will maximise or minimise the objective function of the system. The problem may include constraints which reflect the limitations of the system under study. Thus, optimisation can be summarised as

maximisation or minimisation of a function with subject to constraints on its variables. The action of determining objective, variables and constraints in order to maximise or minimise the performance of a system is known as “modelling” (Nocedal & Wright, 1999). Mathematically, a general optimisation problem can be expressed as follows:

$$max f(X)_{x \in R^n} \qquad subject\ to \qquad g_i(X) = 0,\ \ i = 1, 2, 3, \dots \dots m$$

$$h_k(X)\ \leq 0,\ \ k = 1, 2, 3, \dots . . p$$

- X is the vector of variables or unknown;
- f is the objective function, a quantity which has to be optimised;
- g_i and h_k are the constraints;
- m and p are the number of equalities and inequalities constraints;

Optimisation algorithms can be classified into two main approaches: the gradient based approach is known as a gradient method, and the approach that does not require derivative evaluation is called a non-gradient or direct method (Chapra & Canale, 1985); (A. J. Keane & Nair, 2005). As the name implies, the gradient based methods use either first or sometimes second derivative information to generate efficient algorithm to locate maximum or minimum of a function. Some of the popular gradient based methods include steepest-descent method, conjugate gradient method, Newton’s method, Marquardt’s method and quasi-Newton methods (Chapra & Canale, 1985); (Sundaram, 1996).

Optimisation problems can also be classified by dimensionality. This is done by categorising them into one-dimensional and multi-dimensional problems. One-dimensional problems have a single dependent variable whereas multi-dimensional problems depend on two or more dependent variables (Chapra & Canale, 1985). In this study, the gradient information for the objective function was not available, therefore a derivative-free or non-gradient method was used to investigate the performance of system under study. The problem under study also had more than one dependent variables, therefore multi-dimensional direct search method was implemented for the optimisation purposes.

2.8.2 Direct Search Methods

Direct search methods can be used to solve problems where derivative information is not available for the objective function. These methods have produced exceptional results for the problems where gradient information is not known. A direct search method looks for a set of points around the current point looking for one where value of objective function is maximum or minimum (Lewis, Torczon, & Trosset, 2000); (Chapra & Canale, 1985). There are several approaches in direct search method optimization that can be used to optimize a system. Some of the common one-dimensional optimisation methods include Dichotomous search, Fibonacci search method and Golden-section search. There are some approximation methods that can be used, either in conjunction with direct search methods or on their own, to optimise a system. Those approximation methods are known as Quadratic interpolation method, Cubic interpolation method and Davies, Swann, and Campey method (Antoniou & Lu, 2007).

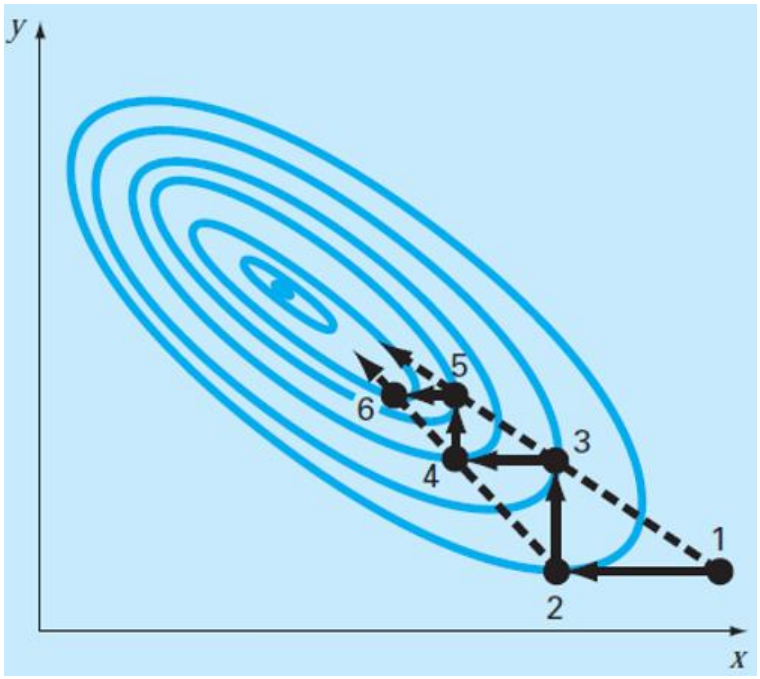

Figure 2.21: A Graphical depiction of pattern search method (Chapra & Canale, 1985)

Multi-dimensional direct methods can be further divided into Random search and Pattern search methods. Random search method evaluates the objective function at randomly selected values of the variables. The maximum of objective function in this method is located by conducting sufficient number of samples. The random search method does not require gradient information but it is deemed to be inefficient because it takes no account of the behaviour of the objective function (Chapra & Canale, 1985); (Davis, 1984). The pattern search method is considered more efficient and still does not require gradient information. In pattern search method, the independent variables are changed one at a time to improve the approximation while other variables or parameters are held constant. Therefore, problem reduces to a sequence of one-dimensional searches as only one variable is changed at a time (Chapra & Canale, 1985); (Lewis et al., 2000). The problem in

this study can then be solved using one of the methods used for solving one-dimensional problems. The method finds minimum or maximum of objective function for one variable at a time and thus cannot be used for global optimisation. Graphically, pattern search method can be illustrated as shown in Figure 2.21. At point 1, y is held constant and variable is varied along x-axis. Next, x is held constant and variable is altered along the y-axis. Points 4, 5, 6 can be generated using a similar method. The alternate points can also be joined using the lines or trajectories 1-3, 3-5 or 2-4, 4-6. These trajectories, known as pattern directions, point in the general direction of the maximum (Chapra & Canale, 1985).

2.9. Previous Studies

In this section, critical review of papers and summary of previous studies on swept wings will be presented. Some of the findings presented here illustrate the advancement of knowledge, while others are presented due to their relevance with the current research. Experimental and computational findings on flow physics of delta wings and flow control of the flowfield will be emphasised due to the reason that present research is mainly concerned with the control of flowfield of the wings closely associated with delta wings. The computational investigations performed in this study offer insight into the results obtained from mixture of inviscid and viscous computational methods. The number of studies conducted on delta wings are numerous as it has been important topic for the research community to shape the future of aviation. The author has made an effort to present both original and modern work of researchers who have pioneered the research on swept wings.

2.9.1 Experimental Findings

Wilson and Lovell (Wilson & Lovell, 1947) were among first researchers to identify some of the fundamental characteristics of highly swept delta wings. They conducted an investigation on DM-1 glider that had triangular plan form with a 60° leading edge sweep. Following the basic tests in Langley full scale tunnel, numerous modifications were made to the glider in an effort to improve its aerodynamic characteristics. The maximum lift coefficient of the original DM-1 glider was increased from 0.61 to 1.01 by mounting sharp leading edges on the glider. Wilson and Lovell found sharp leading edges induce a vortex type flow over the suction surface of the wing that delays the stall to much higher angles of attack.

Peckham (Peckham, 1958) conducted experimental investigations on a series of thick non-cambered slender wings and flat plate slender wings all with sharp edges. The experimental investigations were conducted in a low speed wind tunnel at the Royal Aircraft Establishment. Peckham was one of the first aerodynamicists who obtained comprehensive pressure and balance measurements and published his results. Tests were conducted to understand the effects of planform shape, thickness and aspect ratio at low speeds of delta wings. From his results, he drew conclusion that increasing the aspect ratio and wing thickness moved both attachment line and peak suction line further outboard. Peckham was one of the first researcher to confirm the phenomena of vortex breakdown and he also showed that the position along the vortex at which vortex breakdown occurred depended primarily on a combination of factors including leading edge sweep and the incidence angle of the wing.

Lambourne and Bryer (Lambourne & Bryer, 1959) conducted extensive research on vortex flow separation on swept wings. In one of their experiments, they made measurements over a flat plate at incidence angle of 15°. The plate had a sharp leading edge with a sweep angle of 65°. A 5-tube probe was positioned remotely to provide measurements of static pressure and velocity at numerous positions along the vortex axis. They reported that axial velocity along the vortex flow is higher than the free stream speed and increases considerably as the core of the axis is approached. A favourable pressure gradient was also reported along the vortex core. They (Lambourne & Bryer, 1961) also conducted an investigation into vortex breakdown phenomenon using oil flow patterns. They concluded that low total pressure within the vortex core, coupled with an adverse pressure gradient along the vortex axis can be the fundamental cause of vortex breakdown.

Earnshaw (Earnshaw, 1961) carried out an experimental investigation in a low turbulence wind tunnel on a flat plate delta wing. Measurements were made using five tube yaw meter head at three chord wise positions at an incidence angle of 14.9°. The wing was supported on three vertical struts. It should be noted that large scale velocity variations within the vortex flow were reasonably well established by this time, however little was known about the structure of leading-edge vortices. Earnshaw suggested that primary vortex which results due to the encounter of a sharp leading edge on a swept wing can be divided into three regions: the free shear layer or vortex sheet which emanates from the leading edge and wraps into rotational core, the rotational core where flow is essentially conical in nature and lastly the viscous sub-core where high velocity and pressure gradients are found. A schematic of these three regions is shown in Figure 2.22. It was reported by Earnshaw that axial velocities within viscous sub-core exceed three times the freestream

velocity. These axial velocities are believed to be the cause of large pressure drop on the upper surface of the wing, resulting in high lift and delay of stall angle.

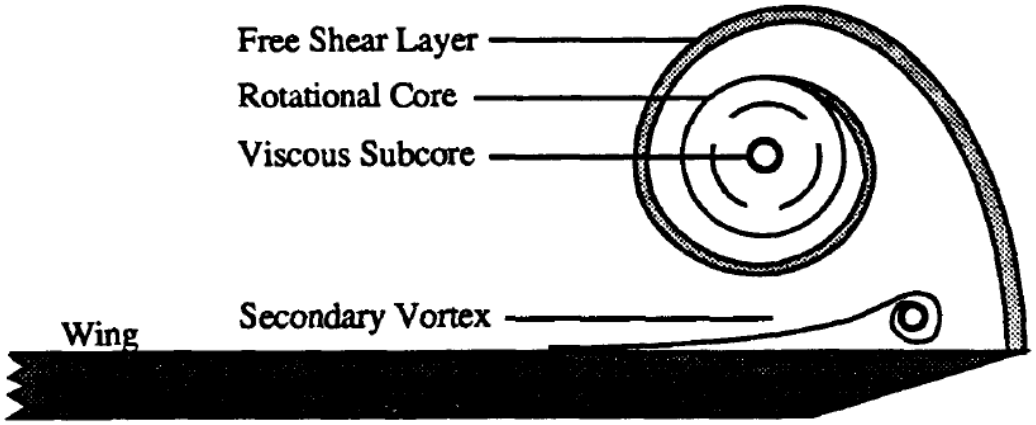

Figure 2.22: Cross section of a leading-edge vortex (S. A. Thompson, 1992)

Mitchell (Mitchell & Délery, 2001) presented an extensive historical review on the research conducted to control the vortical flowfields of swept delta wings. Mitchell divides the flow control of vortical structures of delta wings into two broad categories: passive flow control via mechanical devices or a local action by contouring the surface; and active control using pneumatic flow control techniques. In mechanical devices, he mentions the use of strakes, canards, fillets, leading edge extensions (LEXs), flaps and vortex fences. The pneumatic flow control techniques can consist of various forms of suction and blowing that can include spanwise blowing, leading-edge blowing, blowing along the vortex core and trailing edge blowing. The suction can consist of leeward surface suction, leading edge suction, and suction along the vortex core. According to Mitchell, Henri Werle in 1960 was the first

researcher who applied various flow control techniques to manipulate the flowfield on swept wings.

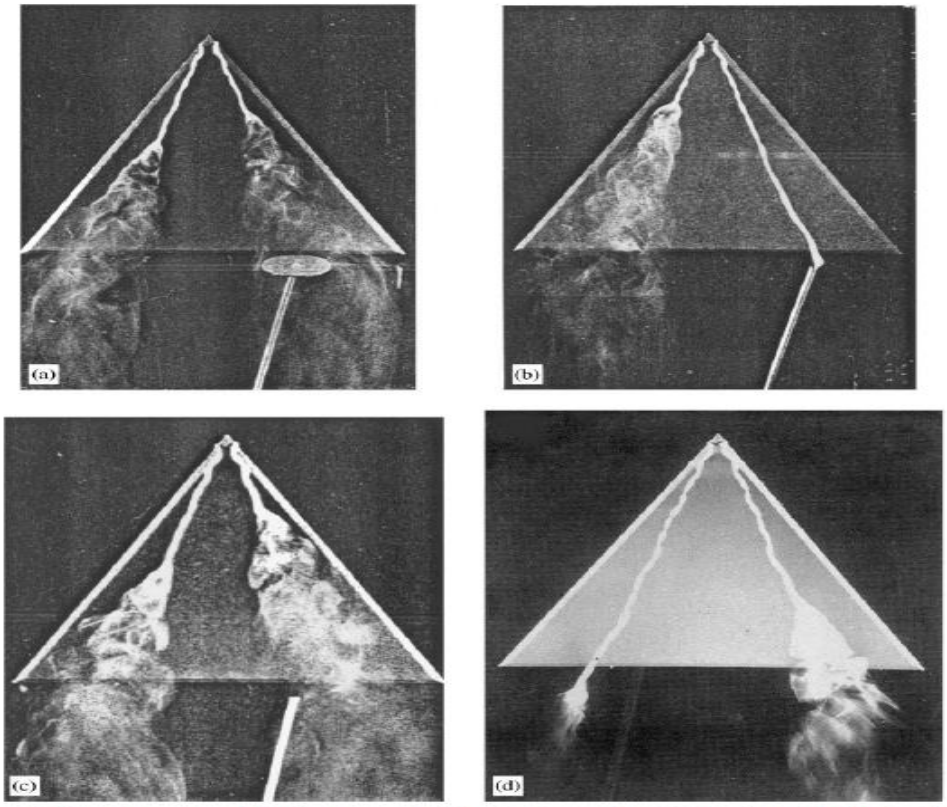

Figure 2.23: Visualisation of four flow control on right side of wing. The left side of wing is uncontrolled. (a) down-stream obstacle. (b) Suction. (c) Blowing opposite the axial velocity of the vortex core. (d) Blowing along the vortex core (Mitchell & Délery, 2001)

Werle conducted investigations by injecting coloured dyes in water tunnel to observe the effect of four different flow control techniques. The outcome of those four techniques when applied to delta wings is shown in Figure 2.23 (a-d). The left side of delta wings in Figure 2.23 present an uncontrolled flow, whereas effect of controlled flow using four different techniques is presented on right side of the wing. It should be noted that in some

cases it is desirable to initiate the process of vortex breakdown therefore flow control using blowing technique can be very useful tool in this regard.

Gursul (Gursul et al., 2007) presented a background of various flow control techniques that have been implemented on delta wings with moderate to high angles of sweep. According to Gursul flow separation, vortex formation, flow reattachment, vortex breakdown, and vortex instabilities are important aspects of flow control. He discusses various flow control techniques that include multiple vortices, control surfaces, blowing and suction, low frequency and high frequency excitation, feedback control and passive flow control with wing flexibility. He argues flexible wings can be used as a passive flow control technique to enhance the lift of swept wing air vehicles. He contends that measurements of aerodynamic forces of delta wings with sweep angles between 40° - 55° have shown that flexible wings can successfully enhance lift and delay stall when compared with the rigid wings of similar geometry.

Buchholz (Buchholz & Tso, 2000) used leading-edge fences and Gurney flap on a 60° delta wing for the purpose of lift enhancement in wind tunnel tests. Lift, drag and pitching moments were measured and flowfield of delta wing was visualised using oil flow patterns. It was observed that both leading-edge fence and Gurney flap can enhance the lift by 5° and 10° respectively. Buchholz believes that suction on the upper surface of the wing was increased due to vortices trap by the leading-edge fence. A Gurney flap is a thin small flat plate attached to the trailing edge, and it can improve the circulation at the trailing edge of the wing.

Rao (Rao, 1979) conducted experimental investigations on a 74° flat plate delta wing to examine the performance of leading edge flaps to control the flow on swept wings. The

primary objective of the research was to improve the efficiency of the basic delta wing by employing different vortex flap arrangements in the lift coefficient range of 0.4 to 0.8. Rao found the drag reductions to be in excess of 30% in that lift coefficient range in comparison to the basic wing configuration. Klute (Klute, Rediniotis, & Telionis, 1996) studied the effect of an apex flap for delaying vortex breakdown at higher angles of attack. He found that apex flap can delay vortex breakdown by 8° beyond the steady flow breakdown incidence angle. Panton (Panton, 1990) and Srigrarom (Srigrarom & Kurosaka, 2000) investigated the effects of geometric modifications to the apex region of delta wings. They observed that wings with higher sweep can also delay the vortex breakdown.

2.9.2 Computational Findings

In the following section, a review of computational studies on swept wings will be presented. With the advent of CFD and the availability of powerful and cheap computational resources, an increasing number of investigations have been performed using computational methods (Crippa, 2008). The computational investigations by research community have been carried out using mixture of computational methods ranging from inviscid Euler to RANS and Unsteady DES to understand the capability of different computational methods to predict vortex separated flows of moderately and highly delta wings. In this section, main results of some the computational studies that are considered relevant towards the current study will be highlighted.

In 1987, a program by the name of International Vortex Flow Experiment on Euler Code Validation was completed. The intention of the program was to produce experimental data necessary to validate CFD codes concerning vortex separated flows. James (James, 1987)

was one of the first researcher to confirm the description of vortex breakdown in an inviscid numerical solution of Euler equations. He compared Euler code predictions with the experimental data provided by the program International Vortex Flow Experiment on Euler Code Validation mentioned above. A delta wing with a sweep angle of 65° was used to compare the experiment results with the predicted coefficients of lift, drag and pitching moment for angles of attack ranging from α = 0° to 25°. The predictions of aerodynamic forces were found to be in good agreement for all cases except for subsonic pitching moments. The effects of vortex breakdown on lift and drag were also accurately predicted using Euler equations but poor pressure coefficients agreement was found in separated flow regions.

Rizzi et al pioneered the computational research of CFD solutions on swept wings. Rizzi and Eriksson (Rizzi & Eriksson, 1985) solved the incompressible Euler equations around a delta wing with a sweep angle of 70°. Their computational results demonstrated the existence of vortex sheet on the upper surface of the wing for the first time. The contour plots of the solution suggest that vortex breakdown was predicted for the first time in a numerical solution of the Euler equations. Rizzi (Rizzi & Engquist, 1987) provided a detailed review on the evolution of CFD with a focus on vortex separated flows around swept wings in their paper. They presented number of computational investigations on swept wings and discussed the methods of implementing CFD on advanced supercomputers.

Fujii (Fujii et al., 1988) performed extensive numerical investigations using Euler and RANS methods to compute the flowfield of double delta wing. Two supercomputers, the CRAY2 at NASA Ames Research centre and Amdahl 1200 at Amdahl Corporation were used to compute three dimensional incompressible flows. To analyse the effects of grid resolution

on the solution, grid independence study was carried out on a series of grids with various levels of refinements. The lift characteristics were same for all types of grids up to the vortex breakdown point. Only solutions of finer grids indicate a change in the slope that resulted from the vortices on both sides of the wing merging into a single vortex. Although Euler predictions showed good agreement with experiment for characteristics of lift coefficients, but it failed to predict separation of leading-edge vortex. RANS solutions showed more realistic results but it was concluded that further grid refinement was required to obtain better quantitative agreement with the experiment.

Newsome (Newsome & Thomas, 1986) used conical delta wings with several cross sectional shapes to compare the solutions between Euler and RANS methods. It was found that viscous RANS equations can describe all relevant physical mechanisms and provide a consistent flow description if adequate grid resolution was used. Euler solutions, however, lack the essential quality of consistency when predicting leading edge vortex separation. Furthermore, Euler method is incapable of predicting the presence of secondary vortices. The cost of evaluating RANS solution when compared with the inviscid Euler equations is only 2% increase in CPU time on same grid. It was concluded that marginal increase in computational cost seems to justify the increase in accuracy.

Cummings (Cummings, Morton, & McDaniel, 2008) and his group performed various time dependent computations using URANS and DES to compute the flowfield around delta wing aircrafts. They identified following factors necessary to carry out high quality time dependent computations: local mesh refinement, grid independence and time step studies, use of sub-iterations for temporal accuracy and the use of appropriate turbulence models for massively separated flows. They believe while it is possible to obtain accurate

time dependent computations around swept wings but computational cost associated with such calculations is much higher than steady state computations. In one of Cummings papers (Cummings & Schütte, 2013) he used RANS, DES and DDES methods to compute the flowfield around rounded leading-edge delta wing with a sweep angle of 65°. The computational results for this investigation were verified with the experiment. Cummings concluded that reasonable predictions of flowfield can be made using RANS turbulence model, but unsteady hybrid methods DES and DDES provide fuller understanding of the flowfield. He recommended researchers to use the method that is appropriate for the level of detail required for the application under study, as computational costs associated with unsteady computations can be high.

A summary of eight experimental cases and ten state of the art CFD solutions on swept wings have been presented by NATO's AVT-WG 080 group (Xing-Zhong & Niek, 2003). A special task group AVT-WG 080 was founded to compile experimental data sets on the behaviour of separated vortex flows on swept wing configurations. Moreover, the task group was tasked to select a reliable experimental database to validate and evaluate different CFD codes against the experimental data.

In this chapter, range of topics that are considered relevant towards this study are covered. The chapter starts with a brief review on flying wing configurations, followed by the description on fundamental aerodynamics of flying wing configurations. The flow physics of separated vortex flows, and repercussions of wing sweep on the flowfield and design of flying wing configurations are covered in detail. Brief introduction on passive and active flow control methods is presented, and the impact of standard passive flow control techniques on RCS is highlighted. The main features of RCS and its impact on stealth air

vehicles are also discussed. High lift devices in the context of passive flow control, and their limitations for flying wing configurations are explained. The section on flow control is followed by the discussion on current role of UVAs. The range of computational methods currently being used to analyse and resolve the aerodynamic problems of flying configurations are elucidated. The chapter also covers theoretical background of CFD and VLM methods, which are implemented in this study to understand the high lift characteristics of flying wing configurations. Brief introduction on optimisation and some of its algorithms is presented. Finally, some of the early experimental efforts to understand the flow physics of separated vortex flows, and the ability of different computational methods to analyse and predict the flowfield of swept wings are highlighted.

Chapter 3. Research Methodology

The investigations on high lift characteristics and lateral flow development over two generic flying wing planforms, termed as configuration 1 and configuration 2 for the purposes of this study, were carried out using a mixture of computational and experimental approaches. One of the configurations under study has moderate leading and trailing edges sweep of $\Lambda = 40°$, whereas other configuration is a cranked shaped highly swept planform with a leading-edge sweep of $\Lambda = 60°$ and trailing edges sweep of $\Lambda = 40°$. Low speed wind tunnel was used for experimental investigations where aerodynamic forces and moments were measured as function of angles of attack. The results of experiment were used to validate and evaluate low and high-fidelity computational methods. Low fidelity computational methods refer to the linear techniques such as Vortex Lattice Method, while non-linear techniques are termed as high-fidelity computational methods such as Euler and RANS. In this section, experiment and computational approaches used for the analysis of clean configurations have been described. It should be noted that range of low and high-fidelity computational methods were utilised to analyse and validate the experimental data. It was considered important to assess the capabilities of both low and high-fidelity computational methods to make a balanced choice for the resolution of the problem in this study.

3.1. Experiment Methodology

3.1.1 Experiment Parameters

An experimental investigation was performed in a low speed wind tunnel using two flat plate scale models, termed as configuration 1 and configuration 2 in this study. The flat plate models are constructed from a thin sheet of aluminium in the Aeronautical laboratory. The models have a thickness of 3mm with sharp edges chamfered at an angle of 45° to promote the formation of separated vortex flows. The models being investigated in this study, configuration 1 and configuration 2 have identical dimensions except the length of root-chord and leading-edge sweep angle. The configuration 1 has a leading-edge sweep angle of $\Lambda = 40°$ and root chord length of 0.4m, while configuration 2 is a cranked-shaped model with a leading-edge sweep angle of $\Lambda = 60°$, and a root chord length of 0.53m. The reference values for the wind tunnel models are summarised in Table 3.1, and detailed dimensions of the models under investigation are provided in Figure 3.9 and Figure 3.10.

The aim of wind tunnel tests is to measure the aerodynamic forces and moments with a high degree of accuracy and reliability. The aerodynamic forces and moments on the model are obtained by using a six-component beam balance. The wind tunnel used for the investigations is a low speed closed return tunnel with a test section size of 0.85m × 1.15m. The test facility has a maximum speed of 36m/s, but it was deemed inappropriate to push the motor to its limits, therefore wind tunnel was not run to its full capacity. The freestream velocity of the wind tunnel was adjusted to approximately 32m/s for the investigations in this study. As was noted earlier, the aerodynamic properties of flying wing planforms with

sharp leading edges are a strong function of the sweep angle, but variation in Reynolds number do not have considerable effect on the aerodynamic properties of the flow. Therefore, velocity of the wind tunnel will have negligible effect on the solution of the problem. The tunnel has a turbulence intensity of 0.5%, and there is a honeycomb mesh upstream of the settling chamber to reduce transverse turbulence. The data acquisition system called picometer is compounded by several items that allow the conversion of physical forces into digital values that can be managed by a computer. The test section has a 6-component beam balance with strut mountings to support the models. The models in this study were mounted on a six-component force balance, and in order to have undisturbed upper surface, brackets were mounted on the lower surface of the model using countersink holes as shown in Figure 3.1. Three components measured the forces in three axes, and the remaining three measured the moments about three axes. It should be noted that wind tunnel models are hung upside-down in the wind tunnel, and models can be yawed in the test facility to assess the lateral stability of configurations under study.

Figure 3.1: Flying wing configuration 2 mounted in low speed wind tunnel

	Configuration 1	*Configuration 2*
Reference Area	0.147068m^2	0.181136m^2
Root Chord	0.4m	0.527701m
Span	0.8m	0.8m
Mean Aerodynamic Chord	0.229149m	0.37m
Moment Reference Point	0.1m	0.23m

Table 3.1: Reference values for the wind tunnel models

3.1.2 Wind Tunnel Calibration

At the start of the experimental investigations, it was deemed necessary to calibrate the balance in order to eliminate any errors in the measurements as fluctuations in the readings provided via the picometer and lack of consistency in the results from previous experiments was a concern. Therefore, it was necessary to establish the extent of the problem by comparing the results of an experiment with known results. The results used for comparison was a test of flat plate model with a sharp leading edge. The model was tested at 32m/s at varying angles of attack. The results of the experiment confirmed the calibration issues with the wind tunnel as there was an inconsistency with the previous

results. Therefore, it was important to resolve the calibration issues of wind tunnel before conducting experiments on real models investigated in this study.

Figure 3.2: Weight applied linearly in order to measure lift and drag

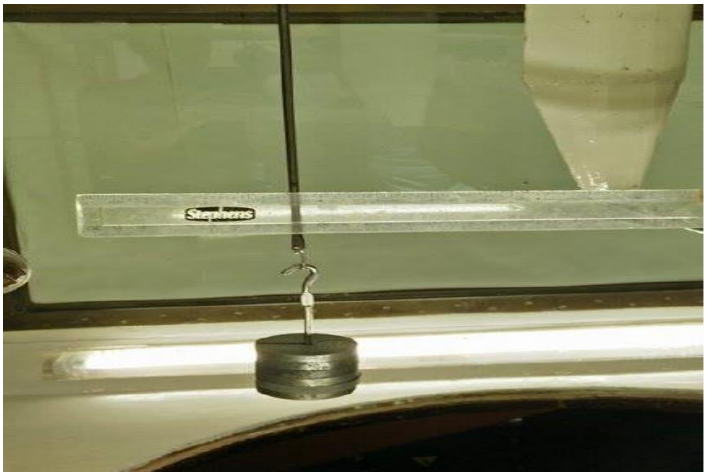

Figure 3.3: Weight linearly applied to measure pitching moments

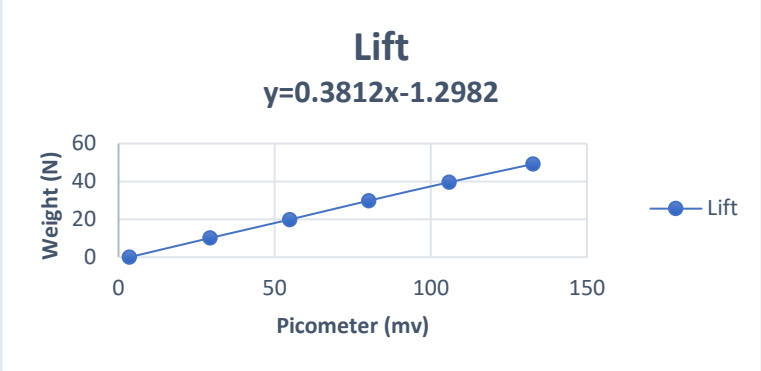

Figure 3.4: New lift calibration with result of 0.3812

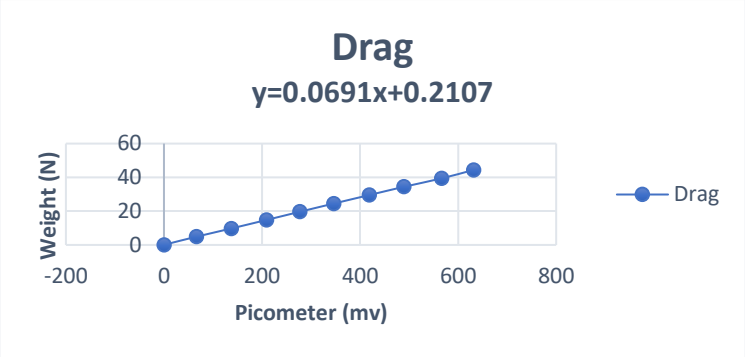

Figure 3.5: New drag calibration with result of 0.0691

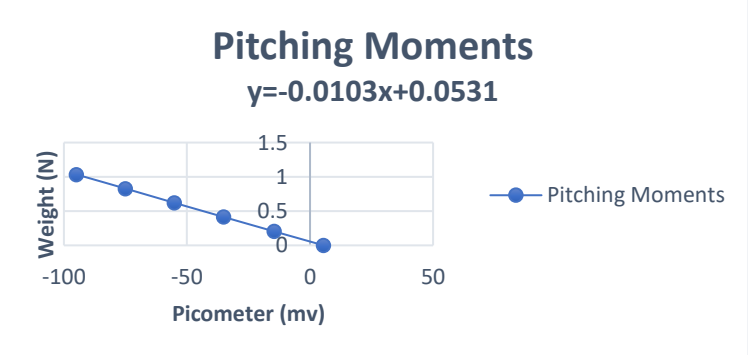

Figure 3.6: New pitching moment calibration with result of -0.0103

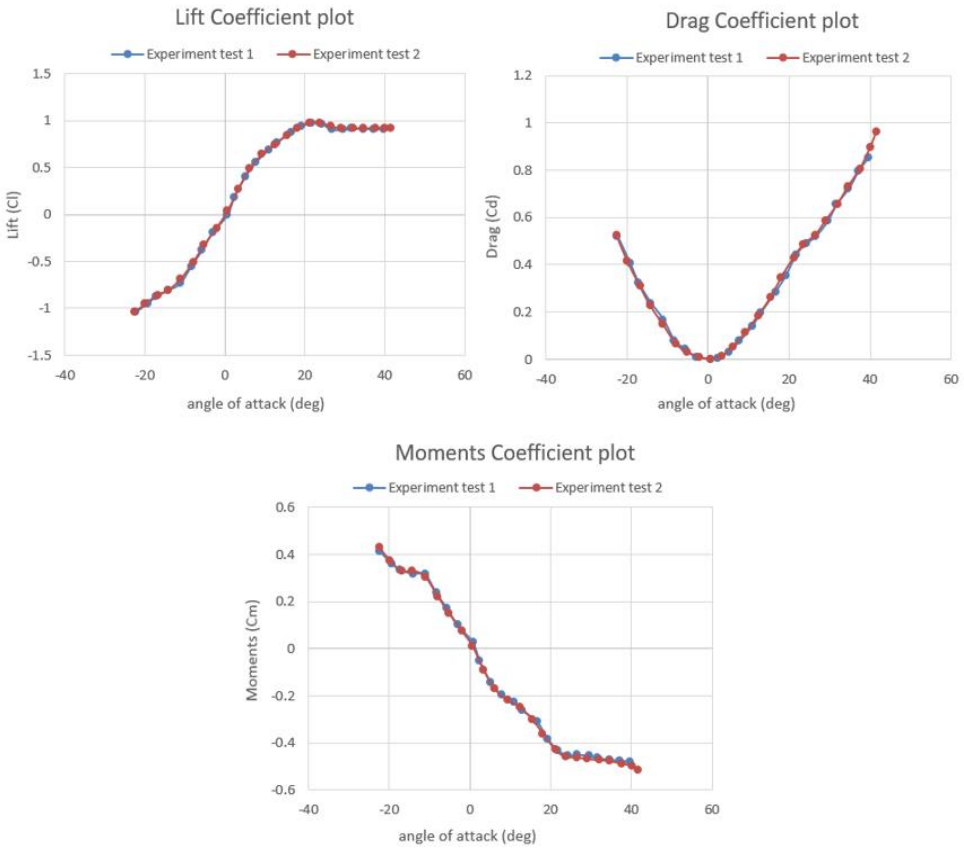

Figure 3.7: Aerodynamic forces and moments comparison between wind tunnel tests for configuration 1

First, simple set of experiments were performed to deduct the calibration values. Lift and drag are read by forces acting vertically and horizontally respectively on the two leading pillars. Pitching moment is read through forces acting on the trailing pillar. When flow passes over the model in wind tunnel, aerodynamic loads and moments are produced by forces exerted on the model. This can be modelled for calibration purposes by linearly applying weight to exert forces in the appropriate directions on the leading and trailing pillars. For lift, a horizontal bar was placed between the two leading pillars. Weight was linearly applied so the force was acting downwards and the resulting mV force was

recorded. To calibrate drag, a pulley system was set up to produce horizontal force as is shown in Figure 3.2. The weight was applied and resulting mV was recorded. Finally, for pitching moment, weight is linearly applied on the trailing pillar as is shown in Figure 3.3.

The results of calibration were plotted and a line of best fit was set to pass through each value as is shown from Figure 3.4 to Figure 3.6 . It should be noted that gradient of the lines replaced the previous calibration values of the wind tunnel. These new calibration values are used in the experimental analysis of the models in this study. The wind tunnel tests were then repeated in order to ensure consistency within experiment solutions as is shown in Figure 3.7. The Figure 3.7 shows aerodynamic coefficients and pitching moments measured in wind tunnel as functions of angles of attack. It can be observed from Figure 3.7 that results from two different experiments have not shown any difference in the solutions of the problem.

3.1.3 Experiment Procedure

At the start of the experiment it is ensured that the wind tunnel is completely unlocked and all the necessary tools for testing are fully functional. The readings of the initial temperature of the tunnel and the atmospheric pressure in the lab are taken as these both will affect the Reynolds number. Initially, incidence angle of the model is set to zero and the output of six component balance are recorded as static or wind off values. The clinometer is used to confirm the angle of incidence of the model. Before the wind tunnel is switched on, values of aerodynamic forces and pitching moments are recorded for each angle of attack. In order to calculate Reynolds number accurately, temperature and betz are recorded during the experiment. The wind tunnel is then switched on and the free

stream velocity is adjusted to approximately 32m/s and the output of six component balance is recorded as dynamic values. The angle of attack is changed by an interval of 2.5° and the dynamic output for each angle of attack is recorded. When flow conditions in the tunnel has stabilised, the data is collected for a period of 20 seconds and within that time, 100 samples points are recorded by the data acquisition recorder. At each angle of attack, the wind off values are subtracted from dynamic values and then multiplied with wind tunnel correction matrix. In order to obtain non-dimensional forces, the data is finally divided by the dynamic pressure and reference area. The spreadsheet of the experimental results is provided in the appendix.

3.2. Computational Methodology

The rapid progress in computer hardware and Computational Fluid Dynamics (CFD) algorithms has made it feasible to numerically investigate and evaluate the flow physics associated with flying wing planforms under consideration in this study (Cummings, 2015). General approach for a computational study has been illustrated in Figure 3.8. The CFD process begins with the geometry, which is either created in mesh generator or imported from an external CAD package. The CAD models forms the framework around which mesh is constructed. CFD code then applies the governing equations of fluid flow to each cell within the mesh. The computer processor communicates information across all the cells and proceeds in an iterative manner towards solving the problem. After considerable computations, a solution is reached where forces and mass flows balance in every cell, and across the whole flow domain. Once the calculation is finished, the CFD solution contains all the pressures and velocities both on and off the surfaces of the object within the flow

domain (Ferziger & Peric, 1999). Although CFD codes are structured around the numerical algorithms that can tackle complex fluid flow problems, but in order to have a confidence in a specific code for the prediction of a flowfield, it is important to verify its accuracy against valid experimental data (John D. Anderson, 1995).

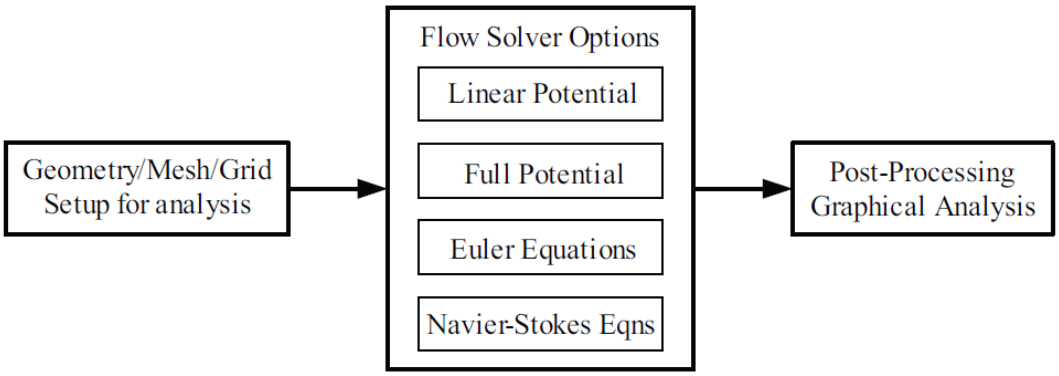

Figure 3.8: Typical functions in a computational aerodynamics system (Liu, 2007)

All CFD computations in this study have been carried out in two types of CFD codes: a commercial CFD code Fluent (ANSYS, 2019) was used to conduct turbulent CFD simulations, and an in-house CFD solver was used to perform non-linear Euler simulations. Fluent solved the compressible, three dimensional Reynolds averaged Navier-Stokes (RANS) equations in a cell centred finite-volume formulation to calculate the solution at hand. The results for clean baseline models were compared with experimental data and Inviscid linear technique called Vortex Lattice Method (VLM) (Tornado, 2019). The flow control investigations of leading-edge and chordwise cavity designs were performed using RANS, and results were compared with wind tunnel tests. Initial efforts were focused on computing and understanding the aerodynamic characteristics of baseline flying wing configurations,

which itself was a challenge due to the complexity of flowfield of flying wing planforms. In the following sections, computational methodology used for the analysis of clean and cavity wings considered in this study have been described.

3.2.1 Geometry and Grid Details

With recent advancements in computing technology, various Computer Aided Engineering (CAE) programmes have become available to design and evaluate the performance of a product. It should be noted that all the models in this study are constructed in an external CAD package SolidWorks. The detailed dimensions of baseline clean wings being investigated in this study can be seen in Figure 3.9 and Figure 3.10. The configuration 1 has a leading-edge sweep angle of $\Lambda = 40°$ and root chord length of 0.4m, while configuration 2 is a cranked-shaped model with a leading-edge sweep angle of $\Lambda = 60°$ and a root chord length of 0.53m, shown in Figure 3.9 and Figure 3.10 respectively. The flying wing models are created in SolidWorks and then exported to a grid generator using Industrial Standard File Format such as IGES.

In this study, both multi-blocks structured and unstructured grids are used to perform the investigations under discussion. Although it takes considerably more effort to generate multi-block structured grids around three dimensional models, but they are widely regarded to be superior to unstructured meshes (Cebeci, 2013). It should be noted that multi-block structured grids were used for the analysis of clean baseline models and flow control studies as they have several advantages over unstructured grids. Multi-block structured grids are aligned in the direction of flow, and as a result they provide more accurate solutions for the boundary layer problems as numerical diffusion is kept to the

minimum. CFD solvers also achieve quicker convergence when grid lines follow the contours of the geometry as is normally the case with structured grids (Ferziger & Peric, 1999). Multi-block structured grids provide much better control to the user than unstructured grids, therefore Engineers can generate precise grids to meet the requirements of the problem under study. These grids use hexahedral elements to fill the volume of the domain, therefore same volume can be filled with fewer elements providing an advantage in time and memory over unstructured grids. Fewer elements within grid result in lower computational times and memory requirements, therefore problem can be calculated in shorter periods of time (J. F. Thompson et al., 1985); (Roache, 1998).

It should be noted that CAE systems grid generator called ANSA was used to generate multi-block structured grids in this study. Three dimensional grids that were used to compute clean wings in this study are shown in Figure 3.11 and Figure 3.12. Only half span of the models was meshed because symmetric boundary conditions are considered for clean and flow control studies. The construction of a suitable grid is an important part in the modelling of the problem, as quality of the mesh determines the accuracy of outcome in the solver. A suitable mesh entails having a finer mesh close to the surface of the wing in order to resolve the viscous effects of the boundary layer. All CFD computations in this study have been carried out in two types of CFD codes: a commercial CFD code Fluent was used to conduct turbulent CFD simulations, and an in-house CFD solver was used to perform non-linear Euler simulations.

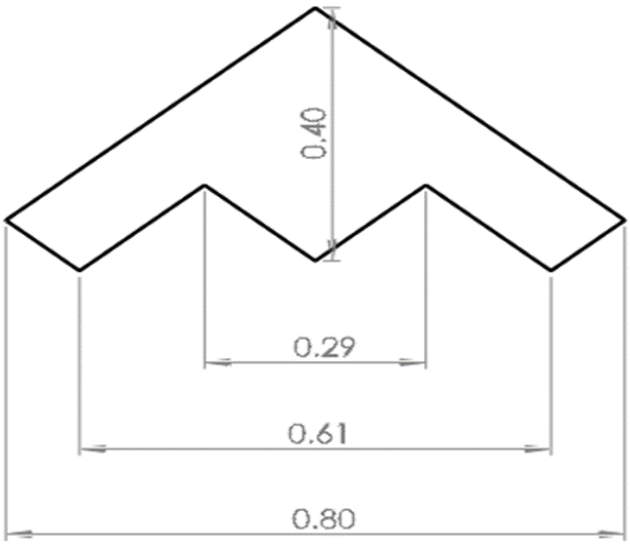

Figure 3.9: Planform view and geometric dimensions of baseline clean configuration 1

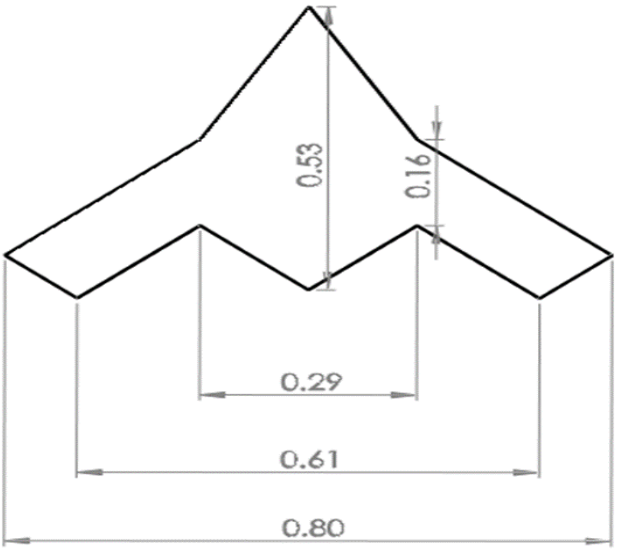

Figure 3.10: Planform view and geometric dimensions of baseline clean configuration 2

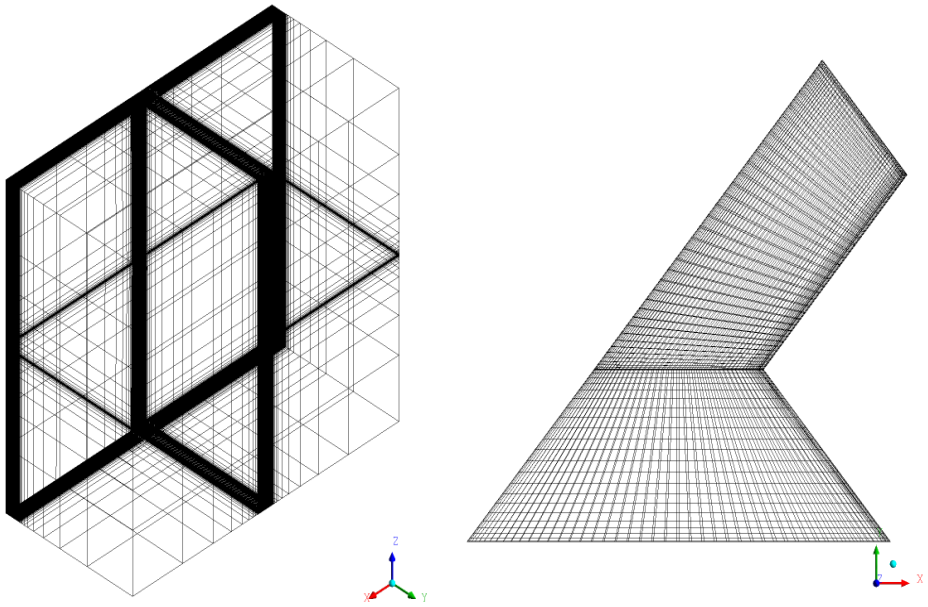

Figure 3.11: Multi-block structured grid for clean configuration 1

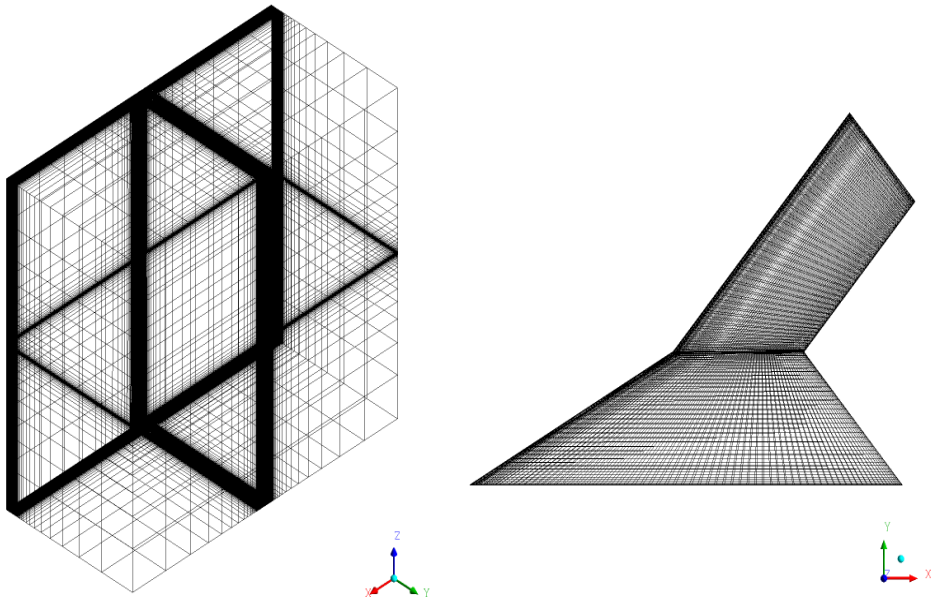

Figure 3.12: Multi-block structured grid for clean configuration 2

	Nodes on UCAV		Max Y^+	C_L	C_D
	Chordwise	Spanwise			
Experiment	-	-	-	**0.93780**	**0.35441**
0.5m	49	63	0.62	0.90282	0.31589
1.0m	56	73	0.57	0.90957	0.31633
2.0m	65	85	0.89	0.91807	0.31796

Table 3.2: Comparing grid refinement results for configuration 1 at incidence angle of 19.2°

	Nodes of UCAV		Max Y^+	C_L	C_D
	Chordwise	Spanwise			
Experiment	-	-	-	**1.13243**	**0.75249**
0.5m	52	61	0.66	1.06686	0.61261
1m	69	81	0.58	1.09242	0.62653
2m	76	89	0.62	1.11015	0.63146
3m	83	98	0.38	1.12047	0.63725

Table 3.3: Comparing grid refinement results for configuration 2 at incidence angle of 29°

The boundary layer is a thin layer close to the solid surface that is dominated by the viscosity of the fluid (John D. Anderson, 1995); (Schlichting et al., 1960). Good initial grid design relies largely on an insight into the expected properties of the flow, and there are no formal ways of estimating the errors introduced by the inadequate grid design for a particular flow. The only way to eliminate the errors due to the coarseness of a grid is to perform a grid dependence study, which is a procedure of successive refinements of an initially coarse grid until key results show little change in the flow (John D. Anderson, 1995); (Pozrikidis, 2017). To ensure grid independent results for this study, three different meshes for configuration 1 and four for configuration 2 were constructed where grid size was increased from coarse to medium and then fine and very fine. The computations for these grids were performed for angles of attack where maximum lift was generated by the corresponding planforms of configurations 1 and configuration 2. Lift and drag coefficients obtained from all the grid dependence computations for both clean configurations are shown in Table 3.2 and Table 3.3 , and their results are compared with the experiment. It can be seen from Table 3.2 and Table 3.3 that successive grid refinements improved the accuracy of the solution for both clean wings. It can be noticed that configuration 1 showed little improvements with the successive grid refinements. This is because flowfield of the configuration 1 is relatively easier to compute, as planform of the wing lacks leading-edge strake and has a moderate leading-edge sweep.

The near wall modelling significantly impacts the fidelity of numerical results as solution variables have large gradients in the near-wall region (Versteeg & Malalasekera, 2007). Therefore, accurate representation of the flow in the near-wall region determines the successful predictions of wall-bounded turbulent flows (Wilcox, 1994). To achieve good

boundary layer resolution, the height of the first cell was placed at $3.0e^{-6}$m for configuration 1, and at $2.54e^{-6}$m for configuration 2. This results in Y^+ values of less than 1 for both configurations in this study, and thus wall function approximations were not used in the solution of the computations. As noted earlier, only limited improvements in the solutions of configuration 1 were displayed with successive mesh refinements, therefore grid with 0.5 million elements was considered of sufficient accuracy for the computations of full flight envelop with angles of attack ranging from $-10 \leq \alpha \leq 40$. For configuration 2, however, the flow is considerably more complicated due to the presence of leading-edge strake and a higher leading-edge sweep. The successive mesh refinements have shown improvements in the solutions of the problem but considering limited computing resources at hand, grid with 2 million elements was selected for the computations of full range of angles of attack. Although, grid of 2 million elements do not provide mesh independent solution for all angles of attack, but it is considered of sufficient accuracy for the current study as meaningful results can be obtained with this grid.

3.2.2 Boundary Conditions

One of the most integral part of the CFD problem is accurate application of boundary conditions (Versteeg & Malalasekera, 2007). The flow variables have to be specified on the boundaries of the physical model as boundary conditions, therefore accurate representation of boundary conditions is critical. In this study, no-slip wall boundary condition was enforced at the wing surface, side-wall was set as symmetry and rest of the domain was computed as Riemann Invariants which is called pressure far-field boundary in the Fluent solver. Symmetry boundaries require no in-put and they can be used to reduce the computational time, but geometry and flowfield must be symmetric for the application

of this boundary condition. The wall boundary condition applies no-slip conditions on the surface of the wing, indicating that velocity of fluid is zero at the wall. The pressure far-field boundary condition is a non-reflecting boundary condition which is based on the introduction of Riemann invariants. The characteristics of the variables for this boundary condition are determined at the boundaries of the domain. Pressure far-field boundary condition can only be applied when computations are run using compressible flow conditions, therefore problem must be computed using the ideal gas law. The computational investigations in this study were based on subsonic flows, therefore comparison with other types of boundary conditions was considered necessary. To achieve this objective, incompressible flow conditions alongside velocity-inlet as the boundary condition were computed, and results are compared with experiment and compressible flow conditions as shown in Table 3.4. The Table shows the comparison of lift and drag coefficients for the incidence angle of 19.2˚. Compressible flow conditions were computed with pressure far-field as the boundary condition, whereas velocity-inlet was used for the computations of incompressible flow conditions. It was established from the computational investigations that compressible flow conditions which were computed using pressure far-field as the boundary condition provided slightly better accuracy for the solution of the problem when compared against experiment. Moreover, compressible flow conditions that were computed using pressure far-field boundary condition achieved faster convergence for the solution of the problem when compared with the computations of incompressible flow conditions. Therefore, pressure far-field was used as the boundary condition for the all the computations in this study.

	Nodes on UCAV		Number of cells	Max Y^+	C_L	C_D
	Chordwise	Spanwise				
Experiment	-	-	-	-	**0.93780**	**0.35441**
Far-field	0.5m	49	63	0.62	0.90282	0.31589
Velocity-Inlet	0.5m	49	63	0.57	0.90918	0.31616

Table 3.4: Comparison of compressible and incompressible computations wherein solutions for far-field and velocity-inlet boundary conditions are analysed for configuration 1

	Nodes on UCAV		Number of cells	Max Y^+	C_L	C_D
	Chordwise	Spanwise				
Experiment	-	-	-	-	**1.13243**	**0.75249**
10c	76	89	2047880	0.62	1.11015	0.63146
15c	77	90	2047880	0.52	1.10854	0.63072

Table 3.5: Comparison of far-field boundaries placed at 10c and 15c from the wing for configuration 2

The size of the domain for the computations of the problem is an important factor which should be taken into the consideration when external flow problems are being investigated. In this study, the exterior or far-field boundaries have been placed at the

length of 10 chords (10c) from the wing that is fixed at the centre location of symmetry boundary condition. There is however, no rule of thumb to establish the correct distance of exterior boundaries. In the far-field, the disturbances must vanish to infinity, and the pressure must be continuous everywhere in the domain. If far-field boundary is placed too close to the wing, this can result in non-physical solution (Liu, 2007). Therefore, it was considered vital to establish the correct position of the exterior far-field boundary. To achieve this objective, two computational investigations with identical flow conditions were performed. In one of the computations, the far-field boundary was placed at the length of 10 chords (10c) from the solid-surface, while in other computational investigation the boundary was located at the length of 15 chords (15c). The results of these computational investigations are presented in Table 3.5. The coefficients of lift and drag were obtained at the incidence angle of 29˚, and results are compared with experiment as shown in Table 3.5. The computational investigations of this study have established that there was a negligible change in results when far-field boundary was moved further out and placed at the length of 15 chords (15c) from the wing. In reality, computational investigation with 10 chords (10c) length have produced marginally better results when compared with the investigation of 15 chords (15c) as shown in Table 3.5. In addition to that, faster convergence for the solution of the problem was observed when the computational analysis of 10 chords (10c) length was carried out. Therefore, far-field boundary was placed at the length of 10 chords (10c) from the surface of the wing for all the computations in this study.

3.2.3 Solver Settings

Fluent has an option for the user to choose from either Pressure solver or Density based solver. As the name suggests, the pressure solver is based on the solution of pressure property of the flow and is the default option in Fluent. The pressure solver is considered sufficient for most of the fluid flow problems. However, for compressible and external flow computations, density-based solver generally provides better accuracy. The two numerical solvers under discussion employ a similar discretisation process, but pressure solver is different than density-based solver in that it solves the governing equations sequentially. In other words, the equations are segregated from one another when solution is being calculated. The density based solver solves all the equations simultaneously, and consequently it consumes more memory (Zikanov, 2010). For this study, pressure solver was tested in the beginning of the research but eventually density-based solver was adopted for all the computations, as it provided more accurate solutions.

Three dimensional problems in CFD take a long time to provide a converged solution. Therefore, in order to reduce computational time, fluent solvers have implemented parallel processing capabilities. Parallel process splits the mesh and data into multiple partitions, then each partition is assigned to a different compute node or a processor. Each node solves a single partition and information is passed back and forth across all partitions using a Message Passing Interface (MPI) library. Therefore, solution to large scale three dimensional CFD problems that are not feasible to process on a single CPU due to hardware restrictions, become possible by splitting the mesh into smaller segments. Each segment of mesh is then allocated to a different compute node where solution is processed. Although solution time is reduced as the number of compute nodes are increased in the

simulation but parallel efficiency can be affected if ratio of communication between different compute nodes is greater than the computation itself. Therefore, in order to gain benefits of turnaround time, the computational grid has to be large enough (Schminder, 2012). In this study, the parallel processing capabilities of the solvers were utilised on local machines for all the computations, and thus computational time of the problems was reduced considerably. It should be noted that four computer nodes were selected for the computation of grids with 0.5 million elements and eight computer nodes were used for other bigger mesh sizes.

In this study air is used as a fluid material with density following the ideal gas law, and one equation Spalart-Allmaras turbulence model is used for all the computational investigations. In Fluent the upwind scheme has the option to choose from either first order upwind scheme or second order upwind scheme. The first order upwind scheme makes it prone to numerical errors, therefore second order upwind scheme has been used for the discretisation of the computations.

Discretisation is a process in which partial differential equations are transformed into algebraic equations to solve for the values of the flowfield variables at discrete locations in space and time (John D. Anderson, 1995). There are many discretisation schemes available in CFD but most common methods are: Finite difference (FD), Finite volume (FV) and Finite element (FE) methods. Other discretisation schemes such as boundary element method, cellular automata and spectral schemes are used for the special classes of problems in CFD. On a very fine grid, each type of method can produce the same solution but some methods are considered more suitable to some classes of problems than others. Discretisation process produces large system of non-linear algebraic equations, and the difference

between discretised equation and the exact one is called the truncation error (Ferziger & Peric, 1999). Most CFD codes use FV or FE methods as they are better suited for modelling the flow past complex geometries. The FV method applies integral form of the conservation equations at the centroid of each cell to calculate the solution variables (Versteeg & Malalasekera, 2007).

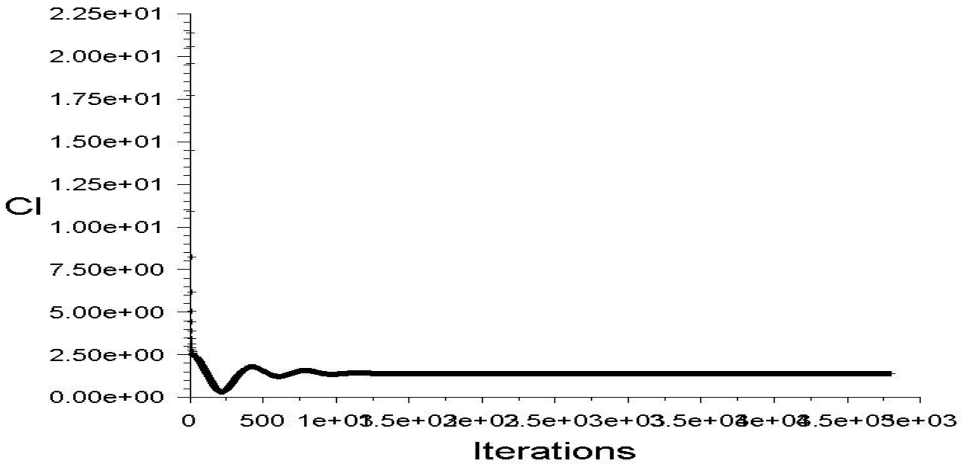

Figure 3.13: Coefficient of lift solution monitor for configuration 2 at incidence angle of 30°

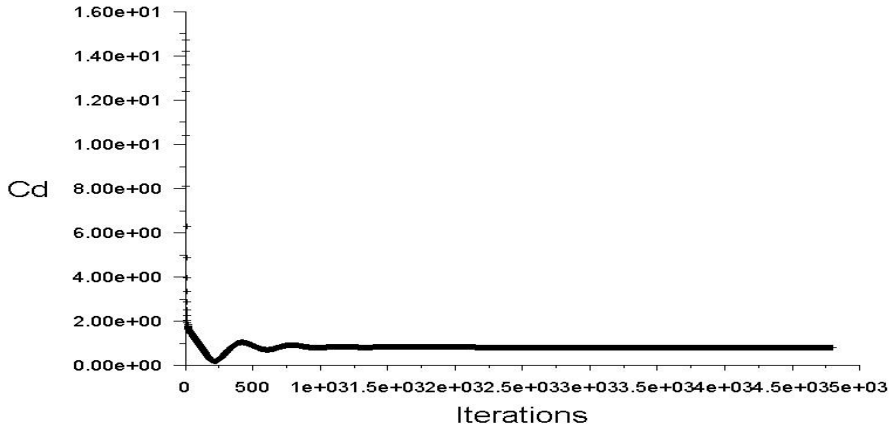

Figure 3.14: Coefficient of drag solution monitor for configuration 2 at incidence angle of 30°

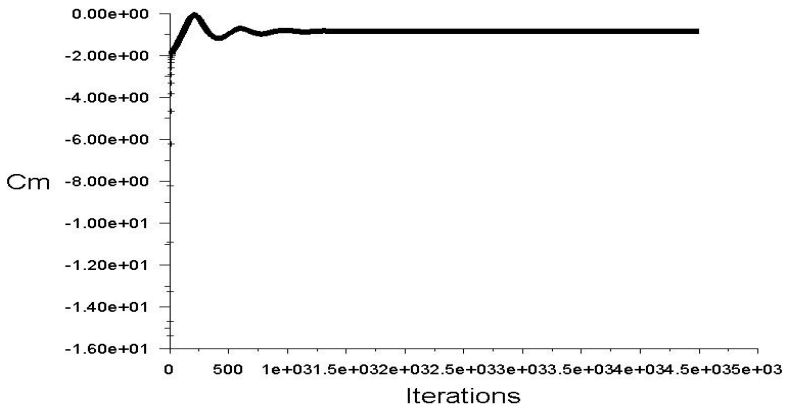

Figure 3.15: Moments coefficient solution monitor for configuration 2 at incidence angle of 30°

The solution methods in this study are based on implicit scheme with Roe-FDS as flux type, and a higher order accuracy is achieved in Fluent using finite volume formulation. The standard initialisation is computed from far-field boundary condition for all the computations under investigation. The solution of steady state RANS equations is achieved in an iterative manner, and the convergence criteria for all the discretised equations for the clean models using structured grids was set to be 10^{-3}. It should be noted that different convergence criteria were used for the computations of unstructured grids. The information regarding unstructured grids will be provided in the relevant section of the thesis. It is important to decide when to stop iterative process as accuracy and efficiency of a solution depends on it (Ferziger & Peric, 1999). Although, all the computations have achieved minimum convergence criteria of 10^{-3}, but in order to assess the convergence of the solution, aerodynamic forces and moments were monitored for all the computations as the solution progressed to its convergence criteria. Solution can only be considered converged when key parameters within problem show negligible change as solution

progresses to its convergence criteria (John D. Anderson, 1995). In this study, coefficients of lift, drag and pitching moments were monitored for all the computations in order to confirm the convergence of the solution as shown from Figure 3.13 to Figure 3.15.

3.3. Vortex Lattice Method Approach

The Vortex Lattice Method (VLM) investigations in this study were performed using a software called Tornado. The VLM is based on linear theory and such analysis can be useful to the designers at early stages of air vehicle design (Cummings, 2015). The program Tornado is based on VLM linear theory and is an open source software written in Matlab, ensuring code portability across all Operating Systems. Aerodynamic forces and moments can be obtained from Tornado in a reasonably straight forward manner. Tornado has a user interface that allows the user to interact directly with the programme. The functions within Tornado are displayed in the form of text menus. There are following four main menus in Tornado: Input operations, Lattice operations, computation operations and lastly Post processing and interactive operations. The first two menus are part of the pre-processor of the code, second menu is the solver of the code and third menu is where post processing of the data is done. There is another menu termed as Auxiliary operations, which contains help files and release information of the code. Tornado version 135 that was released in 2010 has been used for all VLM computations in this thesis. In this study, geometry parameters and boundary conditions for configuration 1 and configuration 2 planforms were defined in pre-processor of the code by answering the sequence of questions.

Figure 3.16: VLM mesh generated in Tornado for Configuration 1

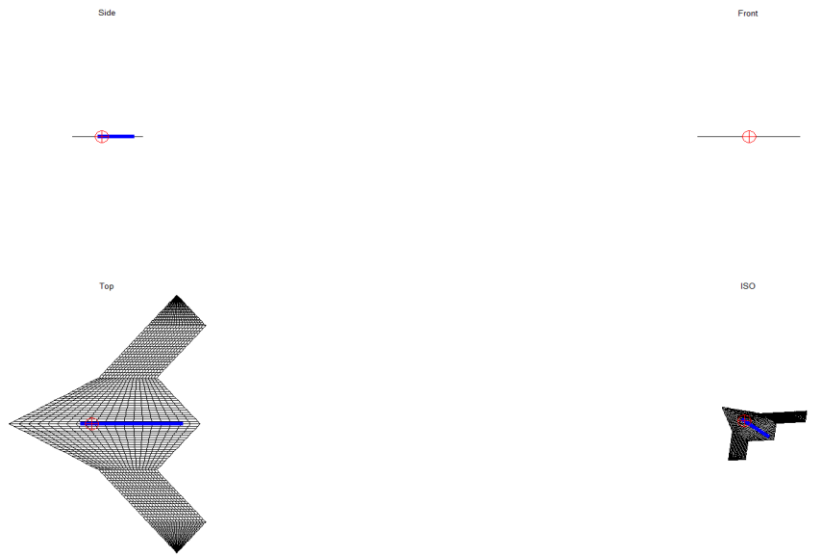

Figure 3.17: VLM mesh generated in Tornado for Configuration 2

The mesh was generated under lattice operations menu that has two types of wake solvers: freestream following wake is a Tornado method, and fixed wake is a standard VLM method. The main difference between the two methods is that Tornado has a freestream following wake which can be influenced by the angles of attack and sideslip, while standard VLM method lacks this functionality. The wake coming off control surfaces and trailing edges of air vehicle is flexible and changes shape according to flight conditions. Therefore, Tornado method represented more realistic flow conditions and was chosen for the computations of this study. Figure 3.16 and Figure 3.17 show different views of VLM mesh that was generated in pre-processor menu of Tornado for both clean configurations under study. Computations were performed under "Computation operations" where sequential state parameter sweep menu was chosen, and solution for angles of attack ranging from α = -20˚ to 40˚ was obtained. In this module, the solver applies Neumann boundary conditions and data is converted into forces and moments within each panel for the calculations of main results. The results are then converted from body to wind axes, and aerodynamic coefficients are computed. The computed results are displayed both numerically and graphically in Post processing menu. The results can either be compared within Matlab or exported as a text file.

In this chapter, research methodologies used to investigate high lift performance and flow physics of two flying wing planforms have been described. One of the flying wing planforms has a moderate leading-edge sweep, while other is a cranked shaped with a higher leading-edge sweep. Experiment methodology describes the experiment procedure that was carried out to investigate the high lift performance for both flying wing planforms. The reference values used to evaluate aerodynamic coefficients and moments of the models

have been presented. The results of the experiment were used to validate and evaluate high and low fidelity computational methods. The computational methodologies used to investigate high lift performance and development of spanwise flow of clean and cavity wings have been explained. The solutions of grid dependent studies and different boundary conditions have been discussed. The mesh details and solver settings used to investigate clean wings have also been provided. In the end of the chapter, the procedure to use VLM code Tornado was explained.

Chapter 4. Flow Visualisation of Clean Wings

4.1. Problem Description

In this section, experimental and computational investigations were carried out on two flying wing configurations, shown in Figure 4.1, to investigate the capability of inviscid and viscous flow methods to predict the high-lift characteristics, and to analyse the lateral flow development over the outboard sections of the wings under study. In particular, high lift characteristics involving vortex separated flows were investigated experimentally in subsonic wind tunnel facilities. One configuration shown on the left side in Figure 4.1 has leading and trailing edges sweep of Λ = 40°, and a chord length of 0.4m is called configuration 1 in this study. The other configuration with a leading-edge strake and shown on the right in Figure 4.1 has a higher leading-edge sweep of Λ = 60°, trailing edges sweep of Λ = 40°, and a root chord length of 0.53m is termed configuration 2 for the purpose of this study. It was considered essential to conduct comprehensive analysis on clean configurations to obtain an understanding of the flow physics of flying configurations with moderate and high leading-edge sweeps, and to evaluate the ability of CFD and VLM codes to predict separated vortex flows, before implementing a flow control mechanism.

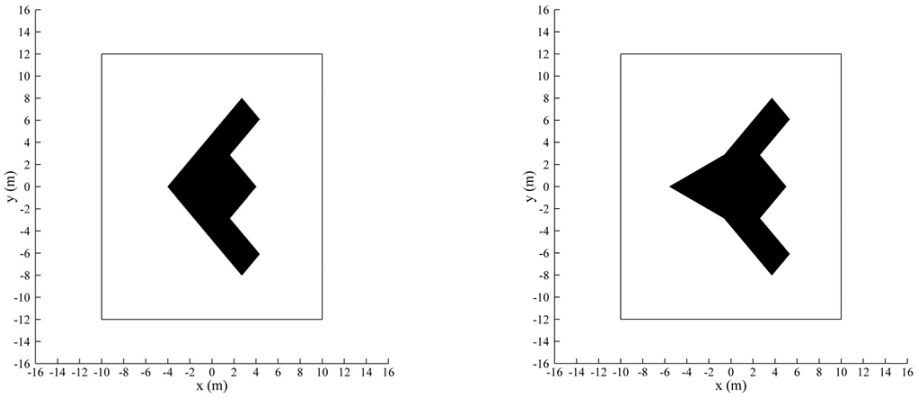

Figure 4.1: Flying-wing planform geometries used for experimental and computational investigations: 40° configuration (left); and 40° with 60° cranked configuration (right)

To determine the aerodynamic behaviour over a range of incidence angles, investigations were conducted on low to post stall angles of attack regimes to include the formation of leading-edge vortices, the onset of vortex breakdown, and the onset of fully separated flow. Experiment tests were conducted in a low speed wind tunnel where aerodynamic forces and moments were measured as function of incidence angles. The wind tunnel tests on flying wing planforms have served the two-fold purpose of elucidating relevant flow phenomena, and providing experimental data for the validation and evaluation of computational methods. The computational methods for the predictions of vortex separated flows can be categorised into lower order methods such as Vortex Lattice Method, and higher order methods such as inviscid Euler and viscous RANS. In this study, computational approaches ranging from Vortex Lattice Method to Euler and viscous Computational Fluid Dynamics (CFD) were employed in order to evaluate the flow physics on flying wing configurations and to validate the experimental data. It is essential to evaluate the accuracy of different computational methods at this stage of the work, so that

a correct approach for future work can be determined. Therefore, a range of computational methods were tested and evaluated on baseline clean configurations in this section of the study. Accurate predictions and understanding of vortex separated flows using computational methods is important for future UCAV concepts, and CFD has a great potential to add in this quest (Görtz, 2005).

The wing with a leading edge strake is often termed as a cranked model, and the crank refers to the break in the leading edge sweep (McCormick, 1995). Experimental investigations on the two models demonstrated that planform with a higher leading-edge sweep can delay the stall angle by 9°. Moreover, it generates higher lift in comparison to wing with a moderate sweep. Highly swept root strakes of configuration 2 provide a combination of separated vortex flows inboard and more conventional flows outboard. This arrangement compensates for the loss of lift on outboard wing sections as the leading edge strake of the wing generates an extra vortex on the suction side of the wing (Barnard & Philpott, 2010). However, it should be noted that the complexity of the flowfield also grows considerably due to the presence of an additional lifting surface in configuration 2, and as a result this planform requires significantly more elements to resolve the flowfield in comparison to configuration 1. For flow control studies, however, only half span of the model was meshed, taking advantage of the symmetric conditions. Therefore, configuration with a higher leading-edge sweep was considered more suitable planform for the flow control studies.

For the predictions of control surface efficiency and yaw stability of the flying wing planform, full span of the model must be computed as the flowfield is not symmetrical. Therefore, considering the computational resources at hand, planform with a moderate

sweep was considered more appropriate choice for the computations that require the full span of the wing to be computed. The computations under discussion deal with the prediction and evaluation of trailing edge control surfaces efficiency and yaw stability of the flying wing configuration.

4.2. Results and Discussion

In this section, linear computational results performed with Tornado, and non-linear computational results investigated with in-house and commercial CFD codes will be discussed and compared with experiment. For all viscous computations, fully turbulent flow was assumed and one equation Spalart-Allmaras turbulence model was used to close the governing equations. The reference values used for all the computations in this study are summarised in Table 4.1. It should be noted that only half span of the wing was computed, therefore reference area values for the wings have been halved. The freestream conditions are provided by the wind tunnel tests where Mach number was 0.1 and the Reynolds number based on aerodynamic mean chord length was 5×10^5. The wings under study have a thickness of 3mm with sharp leading edges, and their edges are chamfered at an angle of 45° to promote the formation of separated vortex flows on the upper surface of the wing. The focus in this part of the research has been on grid refinement and boundary condition studies, including testing of different turbulence models for the wings under investigation. Although, results of these initial investigations are not part of this thesis but they ultimately led to the decision to choose a balanced approach.

	Configuration 1	*Configuration 2*
Reference Area	0.073534m^2	0.090568m^2
Root Chord	0.4m	0.527701m
Span	0.8m	0.8m
Mean Aerodynamic Chord	0.229149m	0.37m
Moment Reference Point	0.1m	0.23m
Elements	523770	2020788

Table 4.1: Reference values for CFD computations

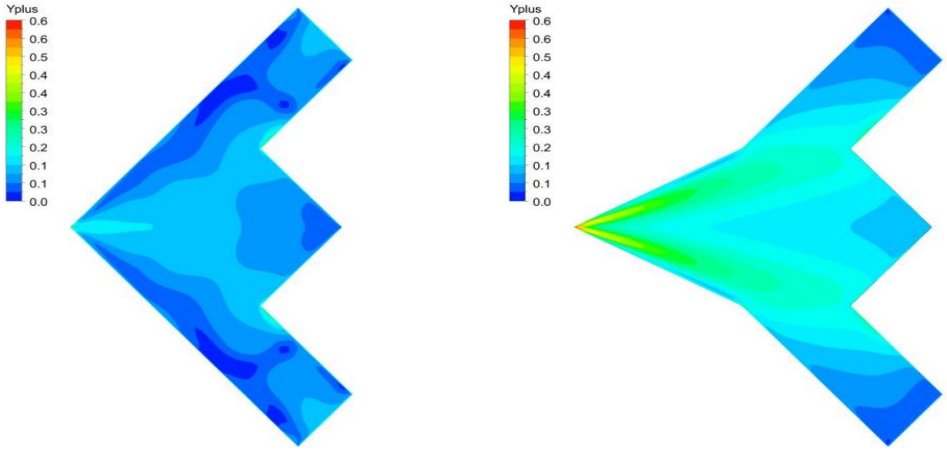

Figure 4.2: Y^+ distribution on suction sides of configuration 1 (left) and configuration 2 (right) at an angle of attack of α = 30˚

The Figure 4.2 shows the Y^+ distribution on the upper surfaces of both configurations at an incidence angle of $\alpha = 30^{\circ}$. It can be seen in Figure 4.2 that Y^+ values for both configurations are below 1. This results in adequate resolution of boundary layer for both configurations in this study. Therefore, wall functions of CFD solver have not been used to estimate the solution variables near the surface of the wings. Aerodynamic lift coefficients were measured in wind tunnel as functions of angles of attack ranging from $-20^{\circ} \leq \alpha \leq 40^{\circ}$, to compare the lift performance of two configurations under study as shown in Figure 4.3. The sweep angle can be changed on a flying wing planform to produce a family of similar flying wing configurations. The aerodynamic characteristics of flying-wing configurations are shown to be a strong function of the sweep angle (Siouris & Qin, 2007). Figure 4.3 shows significant increase in lift at higher angles of attack when leading edge sweep of configuration 2 is increased to $\Lambda = 60°$. Additionally, stall angle was delayed to a higher incidence angle of $\alpha = 30°$, and consequently this makes the planform with higher leading edge sweep more suitable for the analysis and control of lateral flow development on the upper surface of the wing. Changing the sweep angle of a wing should be considered carefully, as it can have a considerable impact on radar cross section signature, aerodynamics, size, and cost of the air vehicle (Okonkwo & Smith, 2016). One of the main advantages of high wing sweep is that it can delay the shockwave formation to higher Mach numbers when air vehicle is cruising at high speeds. Moreover, swept wings are less susceptible to flutter, and they can resolve the potential Centre of Gravity (CG) problem when CG is expected to be too far aft or forward on flying wing configurations (Gudmundsson, 2014a).

Figure 4.4 outlines the pressure distribution of two configurations at incidence angle of α = 20°, and it can be noticed that strength of the leading-edge vortices is significantly stronger on planform with a higher leading-edge sweep. When the wing becomes highly swept, as is the case with configuration 2, high lift performance is enhanced due to the formation of stronger leading-edge vortices at the apex of the wing. Higher wing sweep with a longer chord is generally preferred for reduced radar cross section, and for the integration of propulsion system. On the other hand, higher wing sweep increases structural weight and there are also stability and control implications that should be taken into account at the design stage (Coppin, 2014).

The predicted coefficients of lift, drag and pitching moments of two configurations under investigation in this study are shown from Figure 4.5 to Figure 4.7, and results are compared against experimental data. The charts of aerodynamic forces and pitching moments show the angles of attack range from α = -10˚ to 40˚. It can be seen from Figure 4.5 that lift coefficient plots for both configurations show a linear behaviour up to the angles of attack where wings stall occurs. The drop-in lift starts appearing after the stall angles of attack regime, but unlike the deep stall at high Reynolds number as is the case with rectangular and other planform wings, the stall is not abrupt which is the main characteristics of flying-wing configurations (J.D. Anderson, 2010). It be noticed that drop in lift for configuration with a moderate wing sweep is even less abrupt than for configuration with a higher wing sweep as is shown in Figure 4.5. RANS and Euler methods predict the non-linear part of lift coefficient well but VLM shows a small offset for configuration 2.

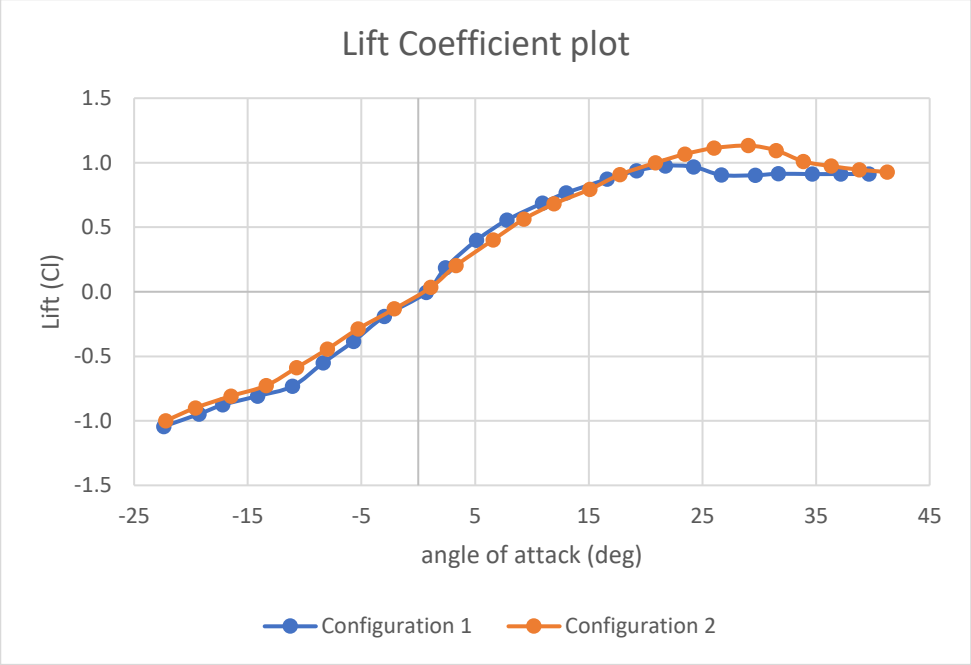

Figure 4.3: Experiment coefficient of lift comparison between configuration 1 and configuration 2 for flat plate models

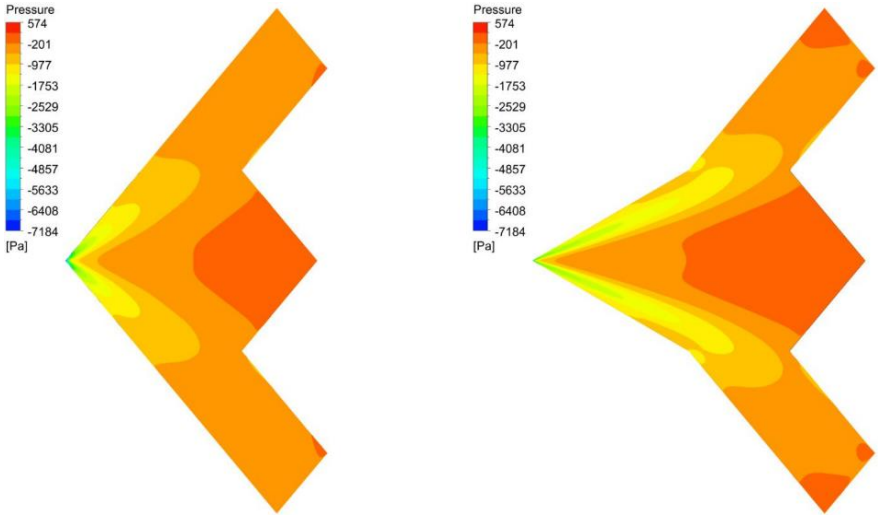

Figure 4.4: Pressure distribution comparison between configuration 1 (left) and configuration 2 (right) at incidence angle of α = 20°

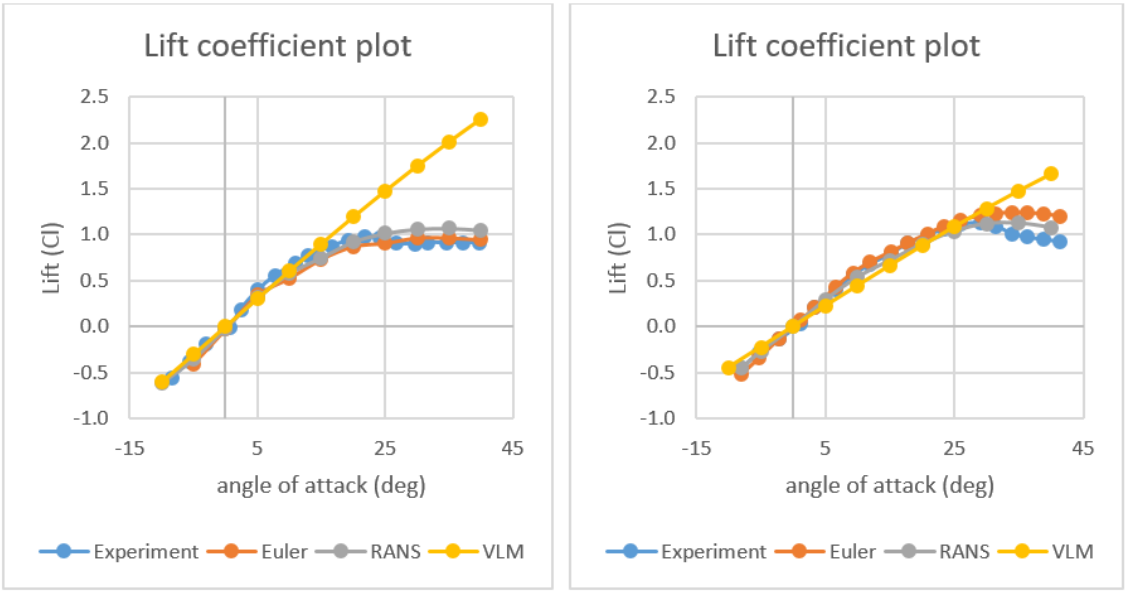

Figure 4.5: Lift coefficient vs angle of attack are shown: 40° configuration 1 (left) and 40° with 60° strake configuration 2 (right)

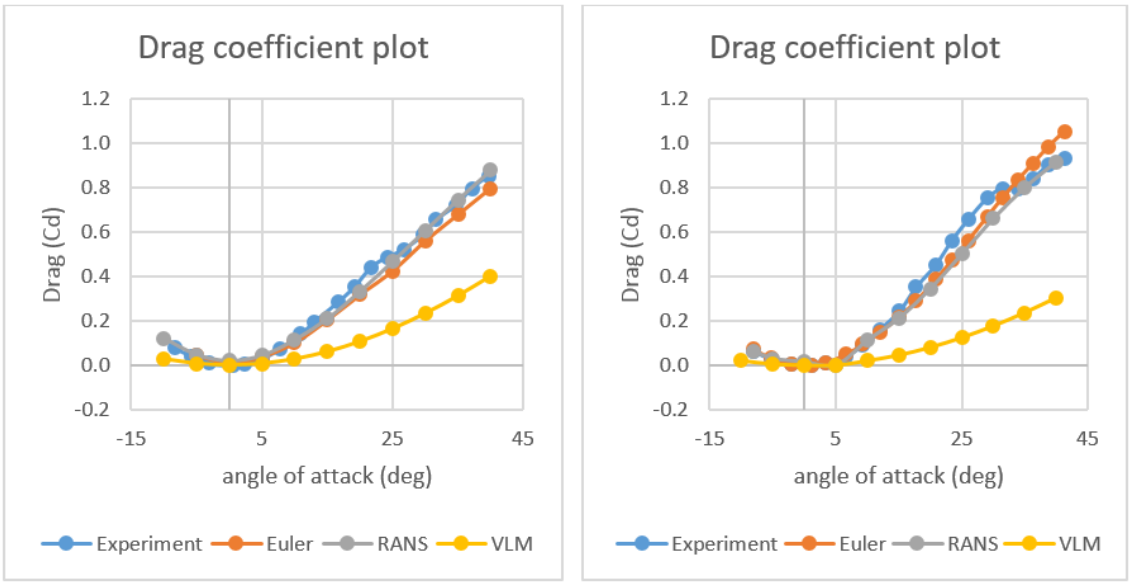

Figure 4.6: Induced-drag coefficient vs angle of attack are shown: 40° configuration (left) and 40° with 60° strake configuration (right)

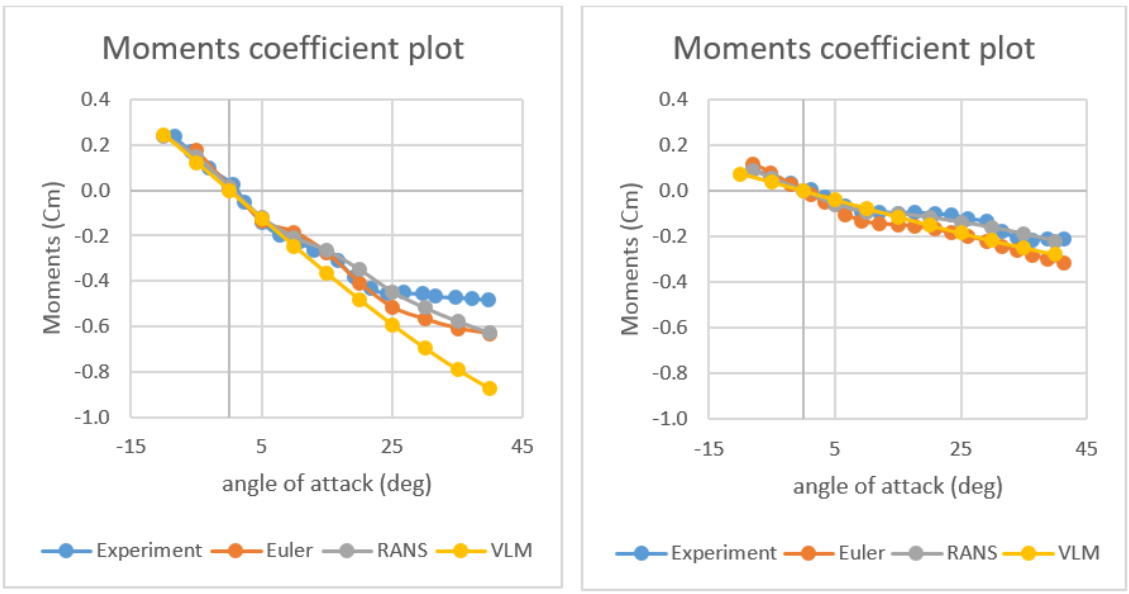

Figure 4.7: Pitching-moment coefficient vs angle of attack are shown: 40° configuration (left) and 40° with 60° strake configuration (right)

It can be seen from moment plots that moment coefficient decreases with increase in incidence angles. The VLM predicts only linear variation of lift and pitching moments with incidence angle, and substantially under-predicts the induced drag. It can be observed from Figure 4.6 that there are differences in drag values at moderate angles of attack but the overall characteristics of the experiment plot is captured well by non-linear computations of Euler and RANS methods. Drag at high incidence angles is predicted particularly well by RANS method. The VLM method assumes the flow to be fully attached to the surface of the wing, and that is not the case for the configurations under investigation. Therefore, VLM approach does not predict the induced drag accurately in this study as is shown in Figure 4.6. Computations using the Euler equations are better able to capture the behaviour of separated vortex flows, and the maximum-lift characteristics. Results

obtained from a RANS method generally give a similar level of agreement with experiment to the Euler results, but the flow separation and the associated non-linear behaviour appear a little later than in the experiment. It can be noticed that Vortex Lattice Method is not suited for highly separated flows as it can only predict linear behaviour of flows at low angles of attack. The primary motive of this study is to predict and control vortex separated flows at moderate to high angles of attack, therefore VLM approach will not be suited for the flying wing configuration considered in this study. Considering the accuracy of RANS method and computational resources available for the work to be undertaken, it was decided that CFD RANS will be more appropriate choice to predict separated vortex flows of highly swept flying wing configuration in this study.

The flying wing configuration with a higher wing sweep was chosen for the analysis and control of lateral flow development on the upper surface of the wing, as this planform generates higher lift and delays the stall angle of attack by nearly 9° as is shown in Figure 4.3. The objective of this study is to control the lateral flow development on the outboard sections of a highly swept wing at medium to high angles of attack in order to exploit the high lift generated by the leading-edge vortices of the flow. Therefore, planform with higher stall angle was considered more practical wing planform to carry out such investigations. The computational investigations on configuration 2 were performed to capture the main characteristic features of the flow as is shown from Figure 4.8 to Figure 4.12. The visualisation of the vortex system and Mach number distribution on the upper surface of the wing are shown in Figure 4.8 and Figure 4.9. It should be noted that results under discussion are calculated for angles of attack ranging from $\alpha = 5°$ to $\alpha = 20°$, and 4 cross section slices along the wing are positioned at 0.2%, 0.4%, 0.6% and 0.8% of the chord

length. The Figure 4.8 shows the slices of pressure coefficient contour on the surface of the wing. This plot enables us to observe the influence of the vortex system on the upper surface of highly swept wing at range of angles of attack. It can be observed that flow separates from the leading-edge and rolls into two vortex sheets of rotating fluid for entire range of angles of attack but the influence of leading-edge vortex is weaker for lower angles of attack. It can be noticed from Figure 4.8 that vortices start as small shear layers but grow in size extending from the apex to the trailing edge of the wing. The outer layer has increased in diameter with distance from the apex to the trailing edge of the wing as can be seen in Figure 4.8. The Figure 4.9 shows the increase in Mach number between the primary vortex core and the upper surface of the wing which is the cause of low pressure on the upper surface of the wing. This pair of vortices is the cause of high lift and delay in wing stall to higher angles of attack over the highly swept wings.

In CFD absolute helicity is used for the calculation of primary vortex Iso surface. Absolute helicity is the value of dot product of velocity and vorticity. The Figure 4.10 shows the plots of absolute helicity based Iso surface in which phenomenon of vortex breakdown has been exhibited. Vortex breakdown on the surface of the wing can create large changes in pitching moments which can affect the stability of air vehicle. As was noted earlier in the thesis that vortex increases in velocity and energy with the angle of attack, and at low angles of attack the vortex breakdown transpires near the trailing edge of the wing without affecting the vortex lift of the wing. However, at a certain point, a sudden decrease in the strength of the primary vortex occurs. It can be observed from Figure 4.10 that vortex breakdown first occurs near the trailing edge of the wing, and then moves forward as the angle of attack in increased. When vortex breakdown reaches the apex of the wing, a

further increase in angle of attack results in loss of coherent vortex flow leading to total flow separation.

The vortical flowfield of configuration 2 was visualised using vector plots and surface streamlines as depicted in Figure 4.11 and Figure 4.12. To visualise more realistic flowfield conditions, configuration 2 with symmetrical aerofoil profiles is presented in this section. A vector plot is a display of vector quantity at grid points showing both magnitude and direction. The area of interest in the Figure 4.11 is the outer sections of the wing where lateral flow can clearly be observed. It can be noticed that intensity of lateral flow increases with higher incidence angle of α = 20°.

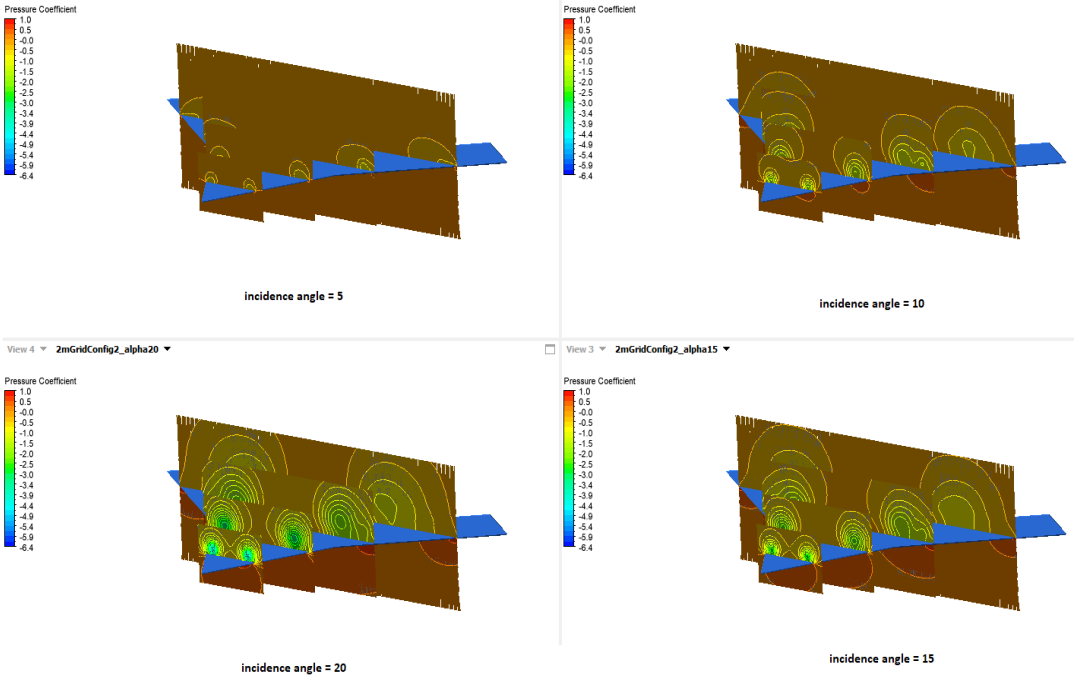

Figure 4.8: Visualisation of the vortex system on the upper surface of configuration 2 for incidence angles from α = 5° to α = 20°

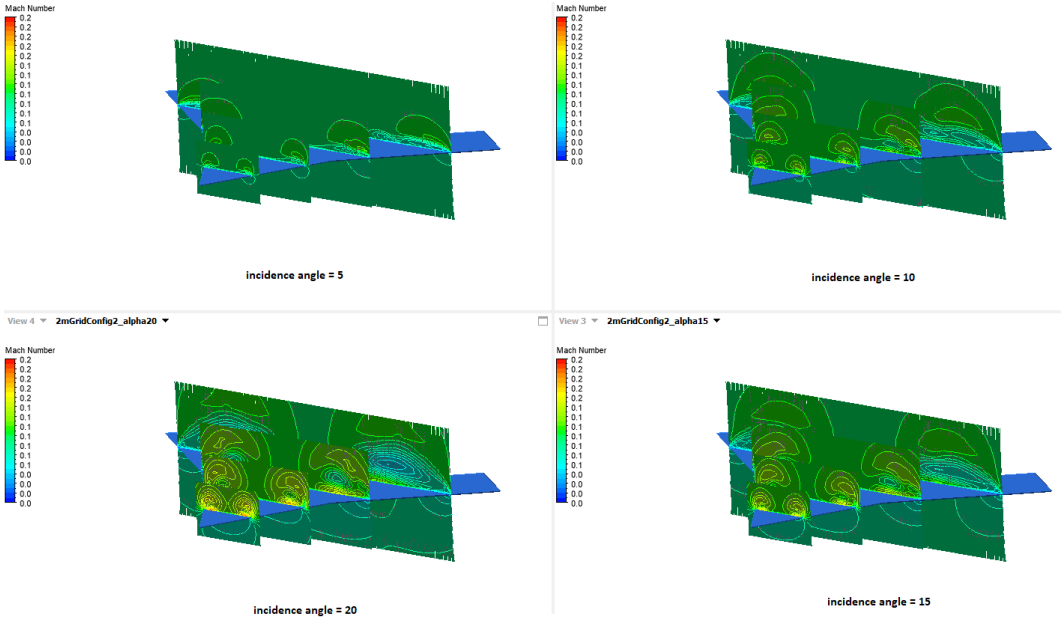

Figure 4.9: Mach number distribution on the upper surface of configuration 2 for incidence angles from α = 5° to α = 20°

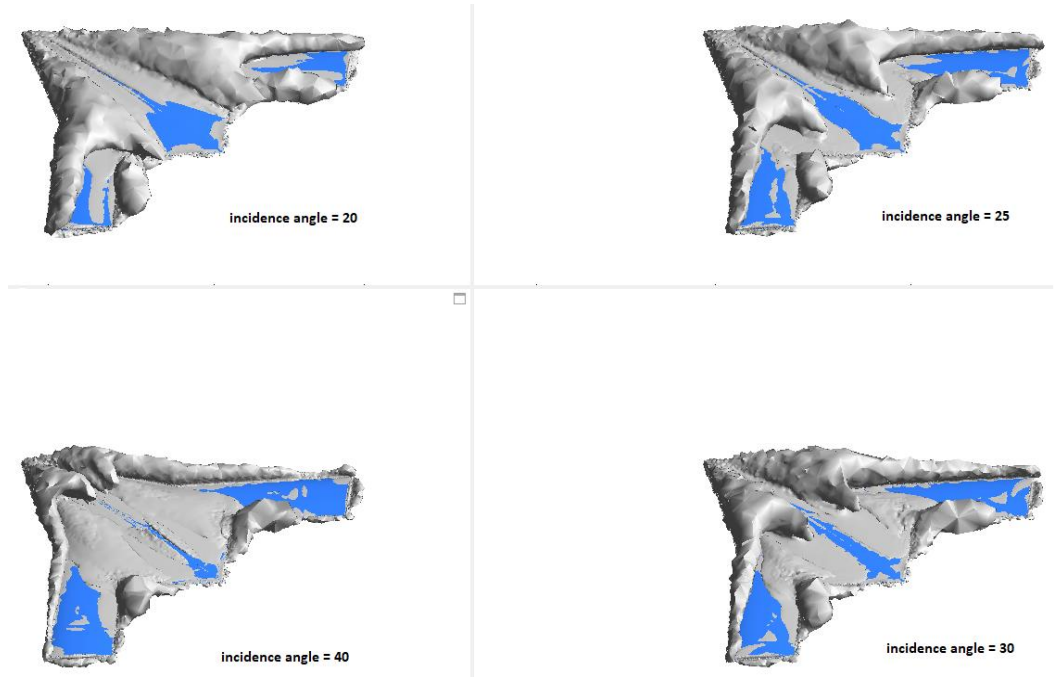

Figure 4.10: Absolute helicity based Iso surface for incidence angles of α = 20° to α = 40°

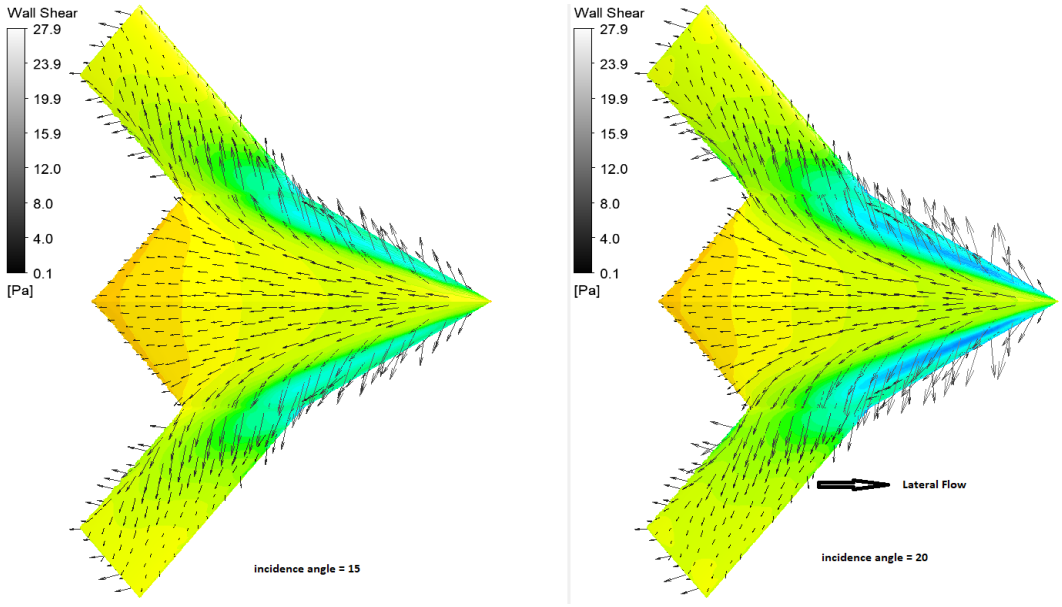

Figure 4.11: Plots of pressure coefficient distribution and wall shear vectors at incidence angles of α = 15° and α = 20°

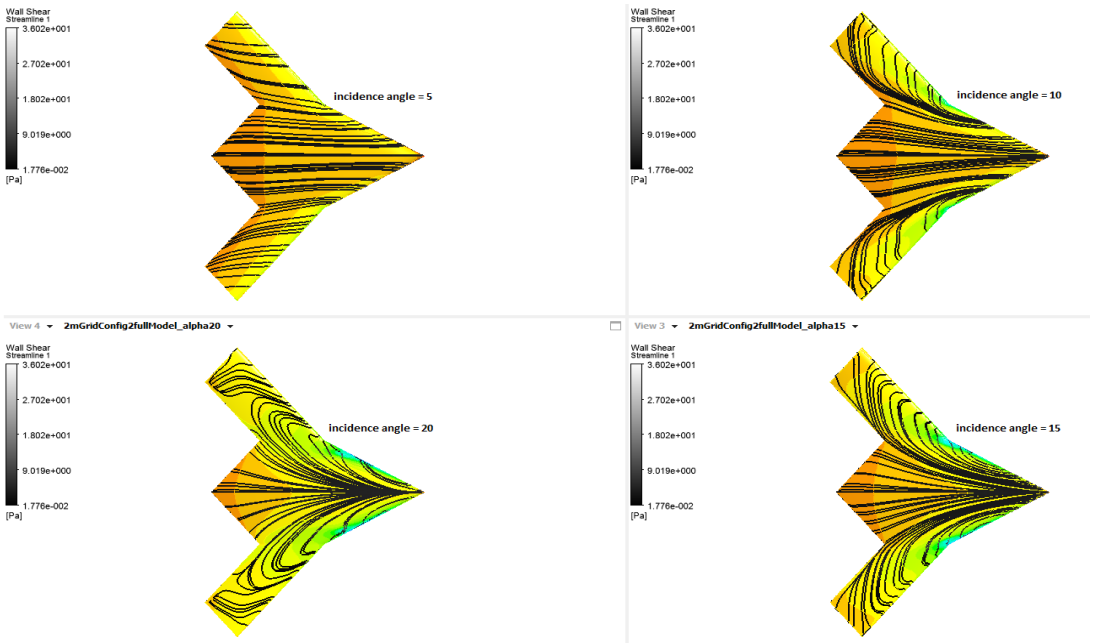

Figure 4.12: Pressure distribution and surface streamlines on upper surface of configuration 2 for incidence angles from α = 5° to α = 20°

In CFD, an illustration of streamlines is another excellent tool for examining the nature of a vortex system on flying wing configurations. A streamline is defined as a curve whose tangent is in the direction of velocity vector at that point (J.D. Anderson, 2010). As was noted earlier, high leading-edge sweep of flying wing configurations promotes separated-vortex flows on such planforms. Leading edge vortices enhance the lift and delay the stall to higher angles of attack, but this additional lift cannot be exploited due to the forward migration of spanwise flow to the outboard sections of the wing. To visualise the vortex separated flows on configuration 2, static pressure distribution and friction streamlines are presented on upper surface for angles of attack ranging from $\alpha = 5^{\circ}$ to 20° as shown in Figure 4.12. The Figure 4.12 provides an improved understanding of what happens to the vortical flowfield as angle of attack is increased from $\alpha = 5^{\circ}$ to 20°. It can be noticed that flow is attached to the surface of the wing when angle of attack is $\alpha = 5°$. However, the large region of attached flow spanning the upper surface of the wing reduces significantly with increase in angle of attack. It can be observed from Figure 4.12 that as angle of attack is increased the migration to the outboard portions of the wing becomes considerably more severe. This results in loss of lateral control as trailing edge control surfaces cannot produce the control forces required to have an effective roll control of air vehicle (Shevell, 1989). The primary motive of this research is to control the lateral flow development on the outboard sections of a highly swept flying wing configuration, so that lateral control of air vehicle at medium to high angles of attack can be enhanced.

In this chapter, high-lift performance of two clean flying wing configurations was measured in a low-speed wind tunnel and compared with predictions using Vortex Lattice Method (VLM), Euler and RANS approaches. The VLM approach predicts a linear variation of lift and

pitching moment with incidence angle, and substantially under-predicts the induced drag. Computations using the Euler equations are better able to capture the separated-vortex flow behaviour and the maximum-lift characteristics. Results obtained from a RANS method generally give a similar level of agreement with experiment to the Euler results. The flowfield of highly swept flying wing configuration was visualised using cross section slices, helicity plots based on iso surfaces and surface streamlines on the upper surface of the wing. It was observed with the help of surface streamlines and vector plots that intensity of spanwise flow on a flying wing configuration increases with the angle of attack.

Chapter 5. Predictions of Stability and Control

5.1. Problem Description

This chapter covers two main topics: first influence of the deflection of trailing edge control surfaces on aerodynamic forces and pitching moments of configuration 1 are computationally analysed; second directional stability of configuration 1 is assessed by making RANS and VLM predictions at sideslip angle of β = 30°. RANS and VLM predictions of directional stability are compared against experiment. The configuration 1 is a generic flying wing configuration with moderately swept leading and trailing edges. The basic geometrical parameters of this flat plate model have been provided in Chapter 3 of this thesis. The planform shape has leading and trailing edges sweep of $\Lambda = 40^{\circ}$. To reduce radar cross section signature, flying wing configurations use flat-faceted surfaces and avoid conventional flight controls which makes an aerodynamic stability and control a special problem (Kermode, 2012). As conventional elevator and rudder are absent from flying wing configurations, it is of particular interest to evaluate and predict pitch and yaw characteristics of such air vehicles.

In this chapter, first RANS predictions of deflected control surfaces of configuration 1 are compared with a clean wing. It should be noted that computational results of clean wing

have already been validated against experiment in chapter 4 of this thesis. The chapter further delves into computational investigations of directional aerodynamics of the flying wing configuration with moderately swept leading and trailing edges. The yaw stability of configuration 1 is assessed by conducting CFD RANS and VLM computations at sideslip angle of $\beta = 30°$, and comparing the predictions of both approaches with experiment. The grid resolution study of two flying wing planforms with high and moderate leading-edge sweeps has established in earlier part of the research, that configuration 1 with moderate leading-edge sweep requires significantly less elements to produce grid independent solutions. For the computations considered in this chapter, full span of wing must be computed to evaluate the efficiency of trailing edge control surfaces and to assess the yaw stability of the wing, as the flow of such computations is not symmetrical. If the wing with high leading-edge sweep is computed for the analysis of trailing edge control surfaces and yaw stability, it will result in considerable increase in computing resources for the resolution of the problem. Therefore, considering the computational resources at hand, configuration 1 was considered more convenient choice for the study in this section.

5.2. Computational Details

5.2.1 Geometry and Grid

The CAD models with deflected control surfaces and clean model for comparison and validation purposes, were constructed in CAD package Solidworks. The assembly suite of Solidworks was used alongside Part suite to construct the CAD model with deflected control surfaces used in this study. The basic dimensions of clean wing are provided in

Chapter 3 of this thesis. The Figure 5.1 shows the control surface deflected up at an angle of 10° with the basic dimensions of the trailing edge control surface. The control surface in question has a cut out of 25% of the local chord. It should be noted that only half span of the wing is shown in Figure 5.1, but full span was computed to predict the efficiency of trailing edge control surfaces.

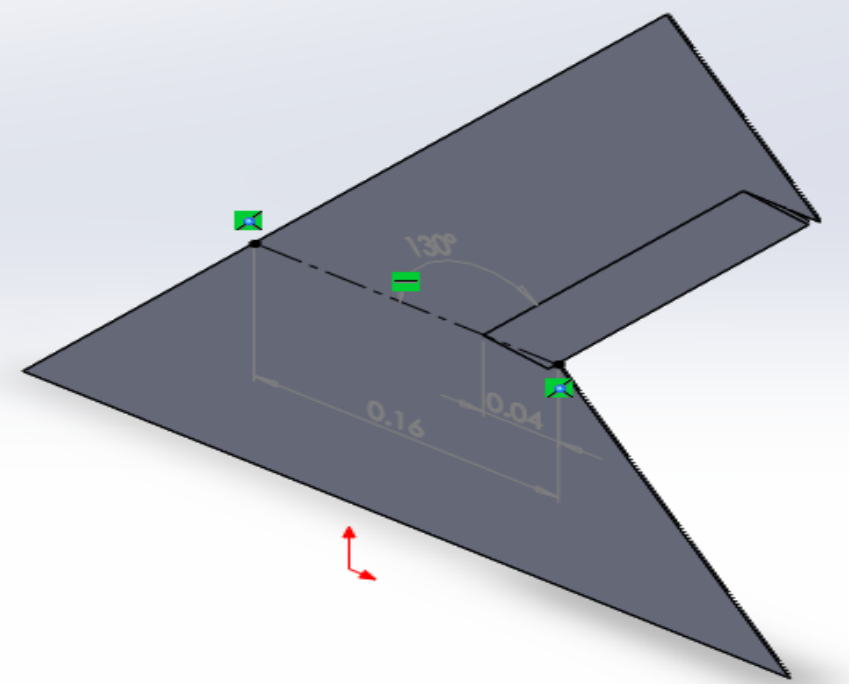

Figure 5.1: Trailing edge control surface deflected up at an angle of 10° on configuration 1

The basic planform shape has leading and trailing edges sweep of $\Lambda = 40^{\circ}$. The flat plate model has a thickness of 3mm with a sharp leading edge, and its edges are chamfered at an angle of 45° to promote the formation of separated vortex flows on the upper surface of the wing. Aerodynamic coefficients and moments for configuration 1 are scaled using the reference area of S_{ref} = 0.1471m^2, and mean aerodynamic chord of C_{ref} =0.2291m. The

chord length of the model is 0.4m long, and moment reference point is located at quarter of chord from the apex of the wing.

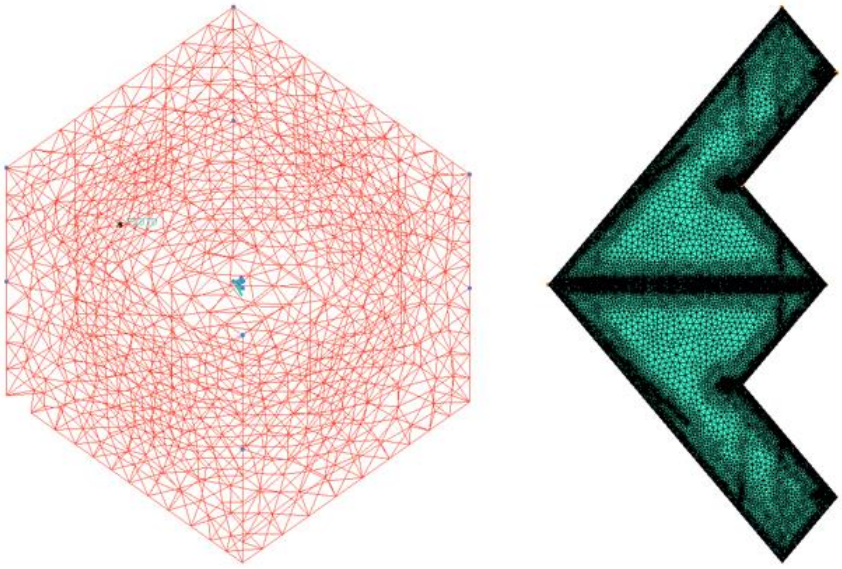

Figure 5.2: Topology of unstructured grid used in this study for Configuration 1

Model	Clean	Control Surface - UP	Control Surface - Down	Yawed
Elements	1904248	1885688	1942532	1904248

Table 5.1: Number of elements used for the computations of control surface and clean wings

In this chapter, ICEM grid generator was used to construct unstructured grids around clean and control surface wings. It should be noted that clean and control surface wings were

computed using similar grid sizes as is shown in Table 5.1, and moreover identical CFD setup was used for the wings to justify their comparison in an acceptable manner. The computational domain is 10 times the chord length of the wing in all directions. The mesh was mirrored in ICEM to represent the full span of the wing for RANS predictions. This doubles the mesh size to around 2 million elements as is shown in Table 5.1. A high-resolution mesh as is shown in Figure 5.2 is constructed on the leading edges of the models in order to resolve the onset of vortical flows. To capture the effects of viscous boundary layer on the solution, prism mesh is generated near the surface of the wing. The grids have a growth rate of 1.40 with 20 prismatic layers, providing Y^+ values of around 1. The basic topology of unstructured grids used in this study is shown in Figure 5.2.

5.2.2 Solver Settings

The freestream conditions for the computations are provided by wind tunnel tests, where Mach = 0.1, and Reynolds number based on aerodynamic mean chord length is $Re = 5\times10^5$. The solver settings of CFD computations are set to match the freestream conditions of wind tunnel tests. The CFD code in this study is run in steady RANS mode assuming fully turbulent conditions, using one equation Spalart-Allmaras turbulence model for the solution. A variety of turbulence models are available in Fluent, but for this study Spalart-Allmaras was considered to be the best choice after testing other commonly used turbulence models. Density based solver with parallel processing capability is used to reduce the computations time. Fluent employs a cell centred finite-volume formulation to solve the governing equations. Two types of boundary conditions are used in these computations: the wall boundary with no slip condition is imposed at the surface of the wing and pressure far-field is used for rest of the domain. Air is computed as a fluid with

density following the ideal gas law and viscosity of air is computed with three coefficient method of Sutherland law. Second order upwind scheme is used for spatial discretisation with Green-Gauss node-based method, and Roe-FDS as flux type. Standard initialisation was computed from far field boundary. The convergence criteria for these computations is set to be 10^{-5}, and in addition aerodynamic coefficients and moments are monitored to ensure convergence of the solution. It should be noted that all the simulations in this study have achieved minimum convergence criteria set for the solver. The computations were carried out using steering with full multi-grid initialisation to achieve faster convergence.

5.3. Stability and Control Results

This section presents two set of results for a moderately swept generic flying wing configuration, termed as configuration 1 in this study. RANS approach is used to compare the computational predictions of deflected control surface wings with the clean configuration. Furthermore, yaw stability of clean configuration is analysed by performing CFD RANS and VLM computations at the sideslip angle of $\beta = 30°$. It should be noted that configuration 1 was chosen for the aerodynamic analysis of control surfaces and yaw stability because full span of wing must be represented, thus mesh requirements are doubled to calculate the problem under consideration. As configuration 1 requires considerably less computational resources to achieve grid independent solution, it was considered more convenient choice to undertake the study in question. The configuration 1 has no leading-edge strake and has moderate leading and trailing edges sweep, therefore grid independent solution can be achieved with relatively fewer number of elements.

Trailing edge control surfaces increase or decrease maximum lift by changing the camber of the wing (Gudmundsson, 2014b). Flying wings combine the functions of elevators and ailerons into one set of flight control by deflecting them up or down in unison to provide pitch control (J.D. Anderson, 2010). There are various types of trailing edge control surfaces in use on aerial vehicles (J.D. Anderson, 1998). The control surface considered in this study is a simple high lift surface that only moves through rotation as is shown in Figure 5.1. This ensures that there will be no change in the gap between trailing edge and the control surface when control surface is deflected. The Figure 5.3 compares predicted aerodynamic coefficients and pitching moments as functions of angles of attack between deflected control surfaces and clean wings. To investigate the influence of control surfaces on aerodynamic forces and moments of clean configuration, both trailing edge control surfaces are deflected as elevators up and down at an angle of 10°. The Figure 5.3 shows the angles of attack range from α = -20° to 40°. It can be seen that difference in aerodynamic coefficients due to elevator deflection is captured very well by RANS predictions. When control surfaces are deflected down at an angle of 10°, consistent increase in aerodynamic coefficients can be noticed in Figure 5.3. Similarly, when control surfaces are deflected upwards, steady decrease in aerodynamic coefficients was observed. The extension of control surfaces not only affect aerodynamic forces but also the pitching moments as is shown in Figure 5.3. There was a corresponding increase and decrease in pitching moments when control surfaces were deployed either in up or down position. This shift in pitching moment can be trimmed by an adequately sized stabiliser or elevator on conventional air vehicles, but on flying wing configurations it can be problematic. Therefore, the shift in pitching moment should be considered at the design stage to minimise its impact on the control of air vehicle.

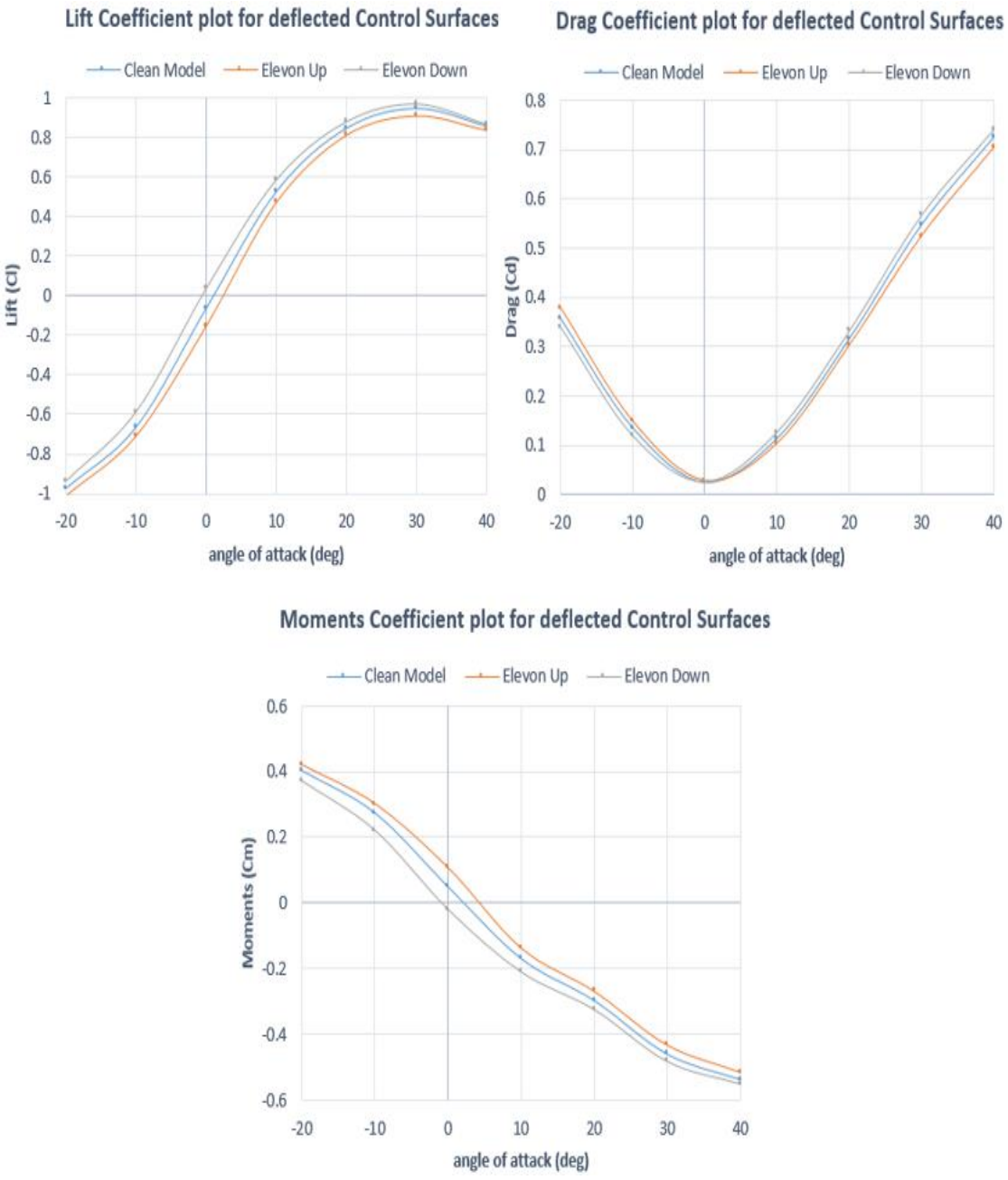

Figure 5.3: Aerodynamic coefficients and moments comparison between clean and control surface models with respect to angle of attack

The trailing edge control surfaces considered in this study is an effective and inexpensive means of increasing and decreasing lift of a flying wing configuration. However, it produces relatively low changes in aerodynamic coefficients when deflection is in the range of 10°, and also when it is compared with more sophisticated trailing edge devices (Gudmundsson, 2014b).

For the yaw control of a flying configuration, differential drag is normally applied on one of the wings to change the sideslip angle of air vehicle. This is achieved by deflecting one control surface up and the other down, usually referred as split flap deflection (Tomac & Stenfelt, 2014). The nonlinear characteristic of complex flow structures of flying wing planforms become severer at non-zero yaw angle conditions (Shim & Park, 2013). The yaw stability of configuration 1 in this study is investigated at sideslip angle of $\beta = 30°$ with zero control surface deflection, and results are compared with the experiment. The configuration 1 was mounted on a 6 components internal balance connected to the rear sting, and the data was collected for aerodynamic forces and moments as a function of alpha with a fixed sideslip angle of $\beta = 30°$. The data was measured for angles of attack ranging from $-20° \leq \alpha \leq 40°$, and results were compared with steady RANS and VLM computational approaches as shown in Figure 5.4. The Figure 5.4 shows the variations of aerodynamic forces and moments with angle of attack and fixed yaw angle of $\beta = 30°$. It has been found by researchers including Tomac (Tomac & Stenfelt, 2014); (Kerstin et al., 2012); (Shim & Park, 2013) that yaw moments for flying wing configurations in sideslip angles are highly non-linear and time dependent computations are required to capture non-linearity and unsteadiness of yaw moments.

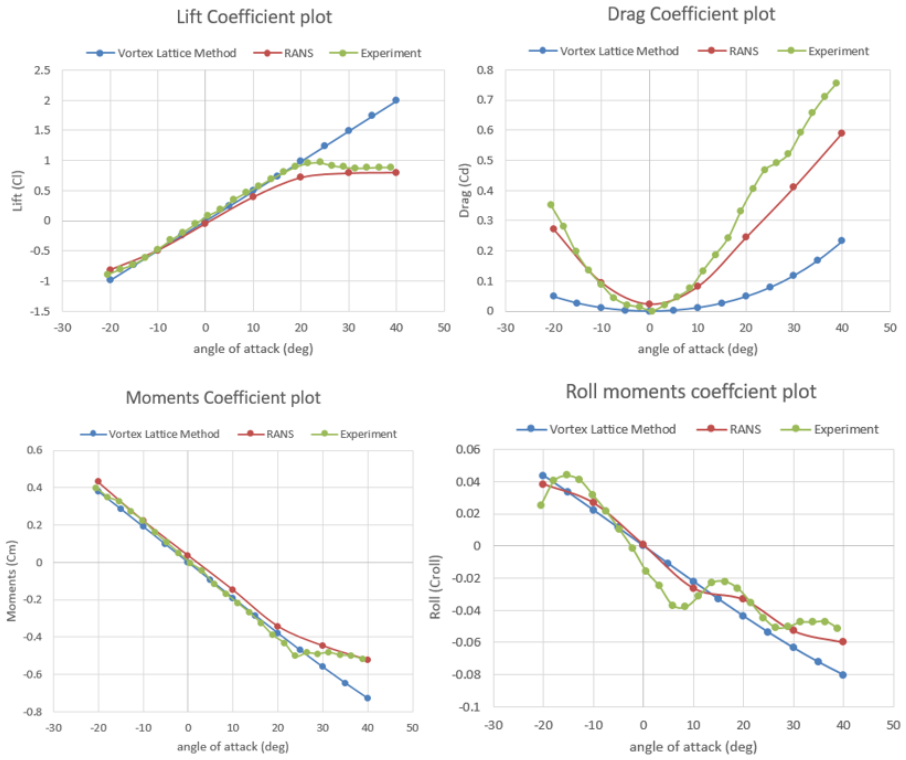

Figure 5.4: Aerodynamic forces and moments for configuration 1 in sideslip angle of 30°

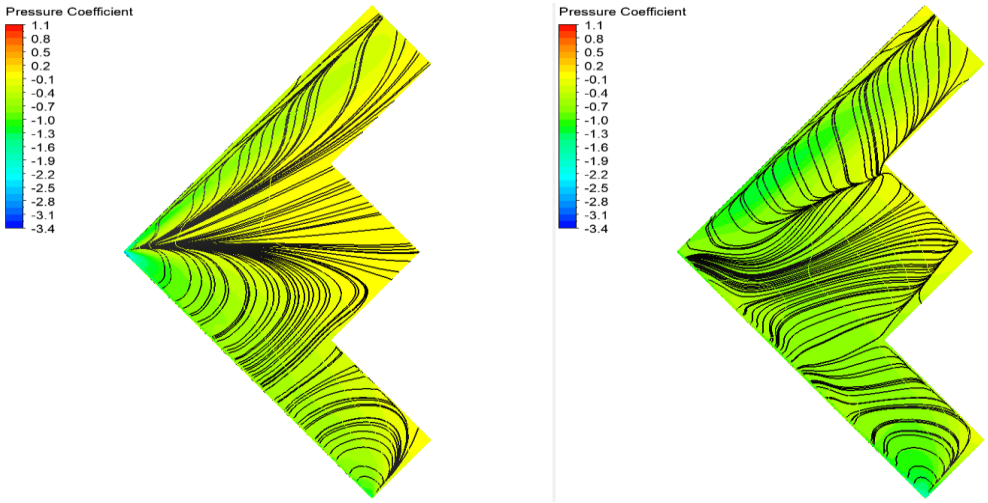

Figure 5.5: Pressure distribution and skin friction lines for alpha = 10° and beta = 30° (left); alpha = 20° and beta = 30° (right)

Although lift in Figure 5.4 is slightly under-predicted by RANS method, but the non-linearity is captured well even for high angles of attack where the flowfield is highly separated and complex. The VLM only predicts the linear variation of lift and pitching moments with respect to incidence angle. The regions where flow is predominately attached are predicted well by VLM for lift and pitching moments, but it under-predicts the induced drag considerably. CFD RANS and VLM fail to capture the non-linearity of rolling moments but the trend is predicted reasonably well by RANS computations. Time dependent computations are required to accurately capture the non-linearity of rolling and yawing moments for flying wing configurations in high sideslip angle (Tomac & Stenfelt, 2014) as is the case in this study. The Figure 5.5 shows pressure distributions and surface skin friction lines to visualise the flowfield of configuration 1 at incidence angles of 10° and 20°, and in a sideslip angle of $\beta = 30°$. The flowfield visualisation provides an essential understanding of the flow characteristics on windward and leeward sides when wing is in sideslip angle. It can be observed from the streamline pattern that symmetrical flow structure of flying wing planform has substantially deteriorated with the yaw angle of $\beta = 30°$. Presence of strong spanwise flow can be observed only on one side of the wing, and the nature of separations are quite different for the two angles of attack under consideration. When angle of attack is $\alpha = 10°$, there are two coherent leading-edge vortices emanating from the apex of the wing, but those vortices have merged into a single much stronger vortex for the incidence angle of $\alpha = 20°$. When angle of attack is increased to $\alpha = 20°$, the flow structure of leading-edge vortices begins to deteriorate. Friction line plots provide useful understanding of underlying flow physics of the flying configuration even though there are small discrepancies present in CFD results.

In this chapter, results for two types of investigations are presented: first RANS method is used to predict the efficiency of trailing edge control surfaces; second yaw stability of flying wing planform is assessed at sideslip angle of β = 30°. The angle of deflection of trailing edge control surfaces for RANS computations was ±10°, and results were compared with the clean wing. RANS captured the influence of control surfaces deflection well by showing corresponding increase and decrease in aerodynamic coefficients and moments when control surfaces were deflected up and down. Yaw stability of wing was analysed by predicting aerodynamic coefficients and moments as functions of angles of attack, and by visualising the flowfield with the help of surface streamlines. The predictions of aerodynamic forces and moments were compared against experiment. Lift and drag coefficients are slightly under-predicted by RANS method, but non-linearity is captured well even for high angles of attack. The VLM only predicts the linear variation of lift and pitching moments with respect to angles of attack. The trend of rolling moments curve was captured well by RANS predictions. The results show that steady RANS approach can predict aerodynamic forces and moments of a flying wing configuration with moderate sweep fairly accurately. For rolling moments, trends are predicted reasonably well with steady state computations even for high angles attack where flowfield is complex. Nevertheless, time dependent computations are required to accurately capture the non-linearity and unsteadiness of rolling and yawing moments.

Chapter 6. Flow Control

6.1. Flow Control Description

This chapter on flow control covers two main topics. First leading-edge and chordwise slots are investigated using CFD RANS to analyse the development of lateral flow on the outboard sections, and to predict high lift characteristics of a highly swept flying wing configuration. The results of RANS predictions are verified with experimental data measured in a low speed wind tunnel. The second part of the chapter covers computational investigations of configuration 2 with deflected control surface to ascertain whether chordwise slots in the wing improved the lift coefficient at high angles of attack upon control surface deflection. This CFD investigation was performed to obtain the change in lift due to flap deflection with and without chordwise slot to quantify the effectiveness of slots for lift enhancement.

It should be noted that words slot and cavity have been used interchangeably in this thesis but they both refer to same concept. Leading edge slots were first considered as early as 1921 by G. V. Lachmann and a British aircraft designer Sir Frederick Handley Page. Their experimental investigations on leading-edge slots established that lift coefficients can almost be doubled by adding leading edge slots to aircraft wings (Barnard & Philpott, 2010).

The principle of a slotted wing was successfully patented and practically implemented on early aircraft designs by Handley Page Ltd (Lachmann, 1924). The original idea behind a slotted wing was to lower landing speeds of aircraft by enhancing the maximum lift coefficients (Kermode, 2012). If an aircraft can operate at low stall speeds during landing and take-off, the length of runway can be reduced (Gudmundsson, 2014b); (Shevell, 1989). It should be noted that although leading-edge slots have been used on straight wings and low speed aircraft to enhance the lift of air vehicles, to the author's knowledge they have never been used to maximise the performance of control surfaces on highly swept flying wing configurations. The author has not found any literature on flying wing configurations where chordwise slots have been used for the purpose of passive of flow control.

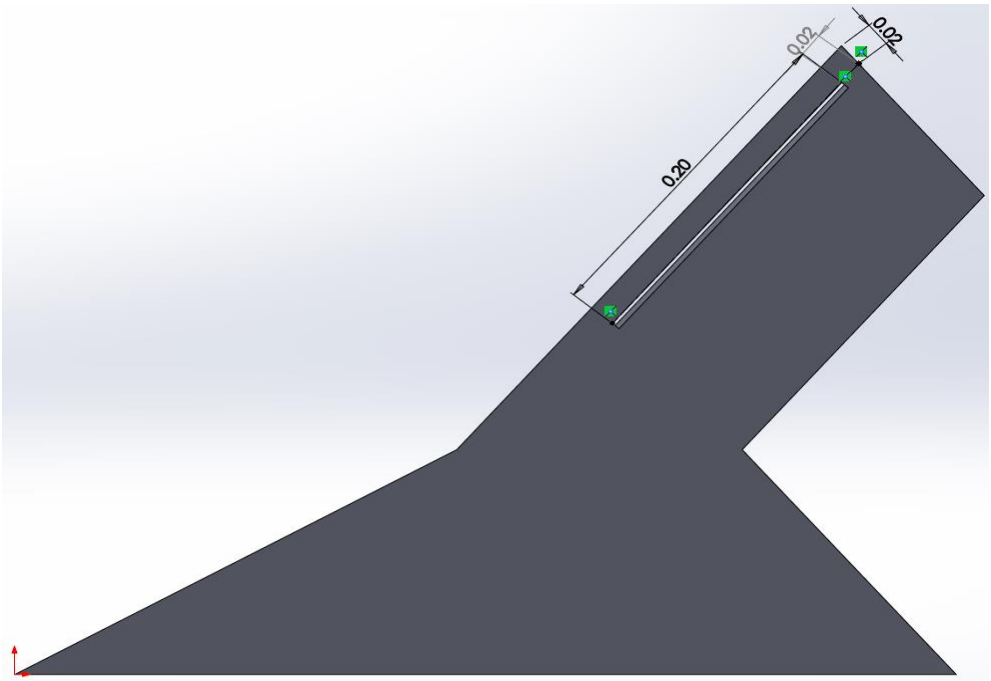

Figure 6.1: Dimensions of leading-edge slot on highly swept flying wing called configuration 2 in this study

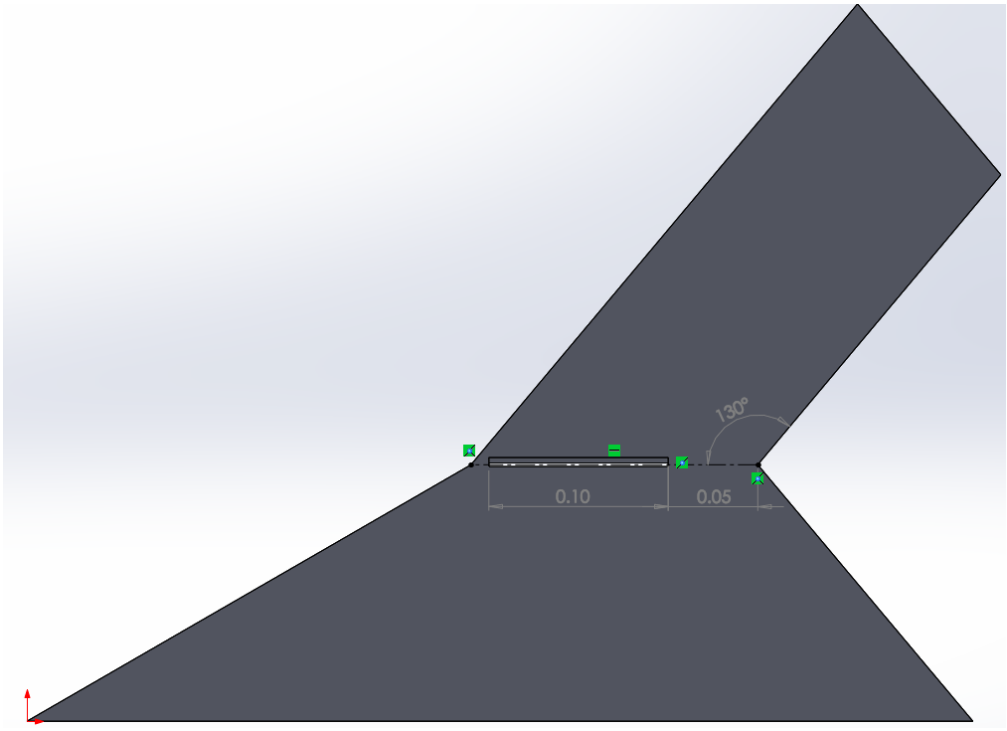

Figure 6.2: Dimensions of chordwise slot on highly swept flying wing called configuration 2 in this study

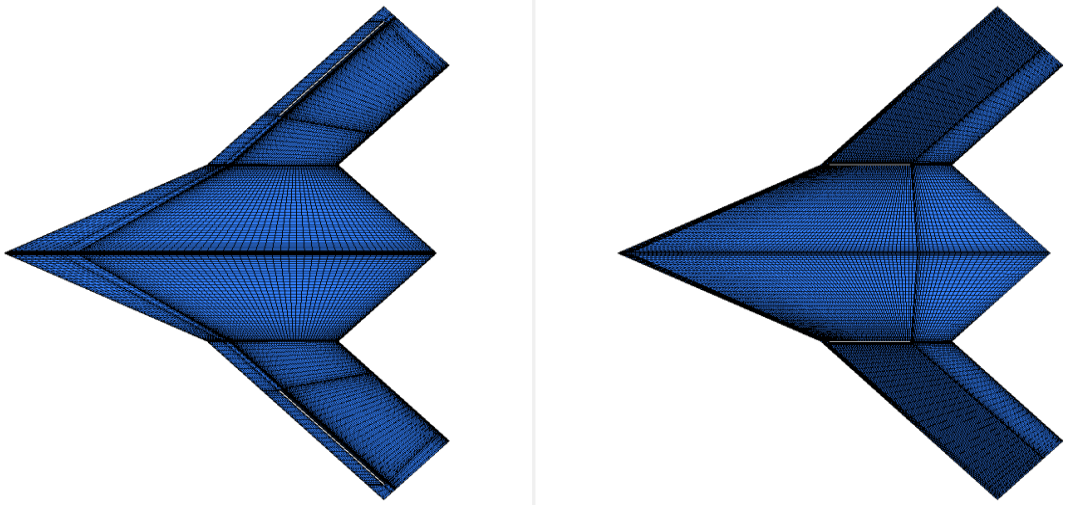

Figure 6.3: Meshed configuration 2 with leading-edge slot (left); chordwise slot (right)

In this study, computational investigations were performed using leading-edge and chordwise slots to analyse the capabilities of these two designs to control the development of viscous lateral flow on the upper surface of the wing at medium to high angles of attack. The dimensions of leading-edge and chordwise cavities used for the investigations are shown in Figure 6.1 and Figure 6.2 respectively. Both leading-edge and chordwise cavities have a width of 2mm with chamfered edges at an angle of 45°. Leading-edge cavity has a length of 0.20m and is placed at the distance of 20mm from the tip and leading edge of the wing as is shown in Figure 6.1. Chordwise cavity has a shorter length of 0.1m in order to accommodate installation of control surfaces over the trailing edge of the wing. Chordwise cavity was placed at the distance of 50mm from the trailing edge and is inclined at an angle of 130° with respect to the trailing edge as is depicted in Figure 6.2.

Model	**Clean**	**Leading-edge cavity**	**Chordwise cavity**
Cells	2078600	2006120	2010956

Table 6.1: Number of elements used for clean, leading-edge and chordwise slot wings for flow control investigations

Multiblock structured grids that have grid topology similar to clean wings were generated around leading-edge and chordwise cavity wings with approximately 2 million elements. It should be noted that baseline clean wing also has a grid of approximately 2 million elements as is shown in Table 6.1. The mesh of leading-edge and chordwise cavity wings

generated for flow control study is shown in Figure 6.3. Every effort was made to generate a mesh similar to clean wings in order to have a reasonable comparison between clean and cavity wings. The boundary conditions and solver settings used for both clean and cavity wings were identical. The description of boundary conditions and solver settings have been provided in Chapter 3 of this thesis.

Once CFD results had established that wing with chordwise slot was more suitable to control the lateral flow on the outboard sections of the wing, it was important to determine whether chordwise slots in the wing improved the lift coefficient upon control surface deflection. To achieve this objective, computational analysis was performed on four types of wing designs: clean wing, clean wing with deflected control surface, wing with chordwise slot but zero deflection and lastly wing with chordwise slot and control deflection. The Figure 6.4 shows the four types of wings used for computational analysis in this study. The control surface for the wings in Figure 6.4 is deflected to 30°. The control surface has a cut out of 25% of the local chord. Only half span of the wings is shown in Figure 6.4 but full span was computed to predict the lift coefficients of the wings. The basic dimensions of clean wing are provided in Chapter 3 of this thesis and the dimensions of chordwise slot have been provided in earlier part of this chapter. For this study, ICEM grid generator was used to construct unstructured grids around all wing designs as is shown in Figure 6.5. All the wing designs were computed using similar grid sizes as is shown in Table 6.2. The mesh was mirrored in ICEM to represent the full span of the wings for the calculation of lift coefficients. To capture the effects of viscous boundary layer on the solution, prism mesh was generated near the surface of the wing. The grids have a growth of rate of 1.40 with 20 prismatic layers.

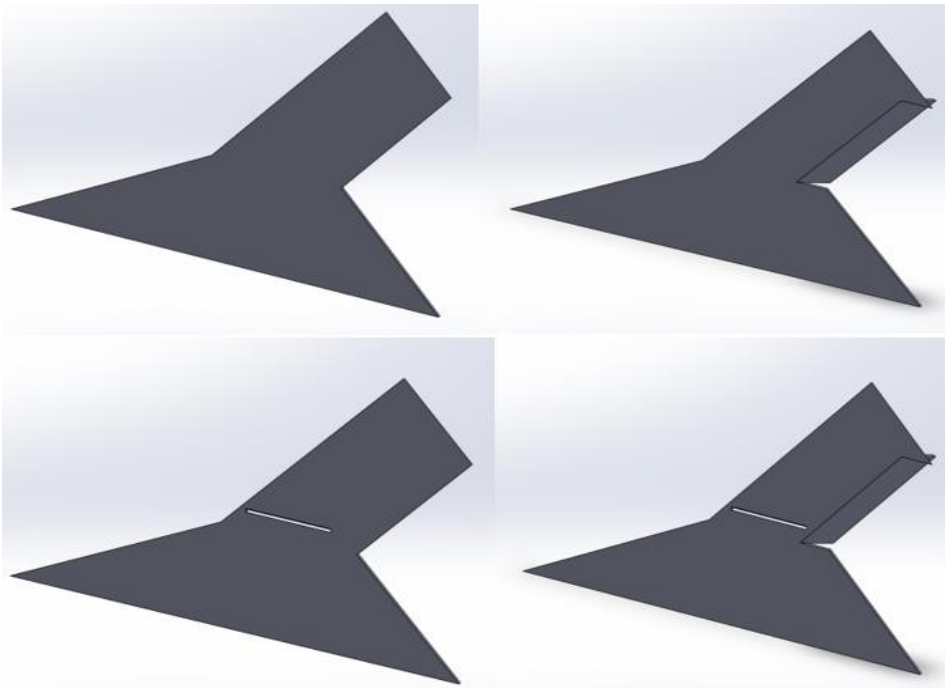

Figure 6.4: Wings used for the calculations of coefficients of lift

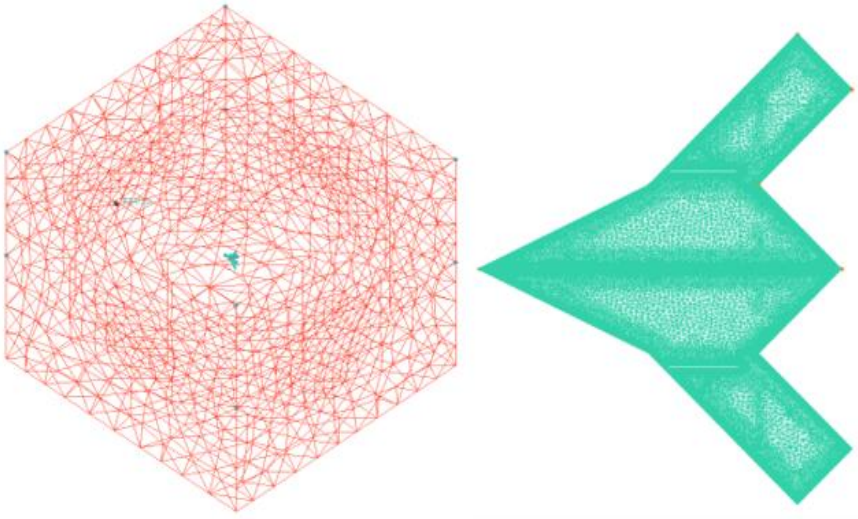

Figure 6.5: Topology of unstructured grid used for highly swept wing

Model	Clean	Clean with Deflected CS	Chordwise Slot	Chordwise Slot with Deflected CS
Elements	2210276	2402778	2155671	2358177

Table 6.2: Number of elements used for the computations of wings

6.2. Flow Control Results

The leading edge flap has been used in the past to increase the maximum lift coefficient and delay the stall angle to a higher angle of attack (J.D. Anderson, 2010); (Kermode, 2012); (Gudmundsson, 2014b). In present study, however, the leading-edge slot was used for the purpose of passive flow control on a highly swept flying wing configuration. Although leading edge flap or slat could also be used to delay boundary layer separation by adding steady stream of fresh airflow, but it should be avoided on a flying wing configuration as it can have adverse effect on RCS of air vehicle (Barnard & Philpott, 2010); (Tomac & Stenfelt, 2014). An alternative to slat was to cut a slot near the leading edge of the wing to form a slotted wing as shown in Figure 6.3. The slots are easier to construct on a flying wing configuration and are less likely to give operational troubles than movable flaps. Furthermore, they have a reduced RCS in comparison to leading edge flap as they lie flush with the surface of the wing. The reason behind the construction of a leading-edge slot was

to route high pressure air through the gap in order to create an airflow barrier for the lateral boundary layer on the upper side of the wing. This will result in fresh stream of airflow taking place through the gap of a leading-edge cavity on upper surface of the wing in addition to the primary flow (Kermode, 2012); (J.D. Anderson, 2010) (Gudmundsson, 2014b). The idea was to have a secondary stream of airflow on the upper surface of the wing that would create an airflow barrier for lateral flow and energise the boundary layer behind the leading-edge slot, and thus route more airflow over the trailing edge control surfaces of air vehicle.

To verify the results of RANS computations, leading-edge slots were constructed on a highly swept flying wing configuration to conduct an experimental investigation in a low speed wind tunnel. Aerodynamic forces and moments were measured as functions of angles of attack and results were compared with clean baseline wing. This served two-fold purpose of elucidating relevant high lift characteristics of a slotted wing and provided experimental data for validation and evaluation of computational methods. The leading-edge slot in this study has chamfered edges at an angle of 45° to boost the flow of air from lower to upper surface of the wing. The CFD computations of leading-edge slot wing were performed using RANS, and predictions are compared with experiment as shown in Figure 6.6. The Figure 6.6 shows the angles of attack range from α = -8˚ to 40˚. The purpose of this computational investigation was to determine the effect of leading-edge cavity on high lift characteristics of a highly swept flying wing configuration. It can be noticed from Figure 6.6 that predicted RANS results show good agreement with the data obtained from low speed wind tunnel tests. The general trends of RANS predictions compare well with the experiment, but a small decrease in aerodynamic forces was observed for predicted results above incidence

angle of 10°. It can also be observed from Figure 6.6 that RANS have slightly over-predicted the values for post stall angles of attack regime. The results of experiment have shown a slightly higher maximum lift coefficient for the model with a leading-edge cavity in comparison to the clean wing, but induced drag and pitching moments have produced results similar to the clean baseline wing.

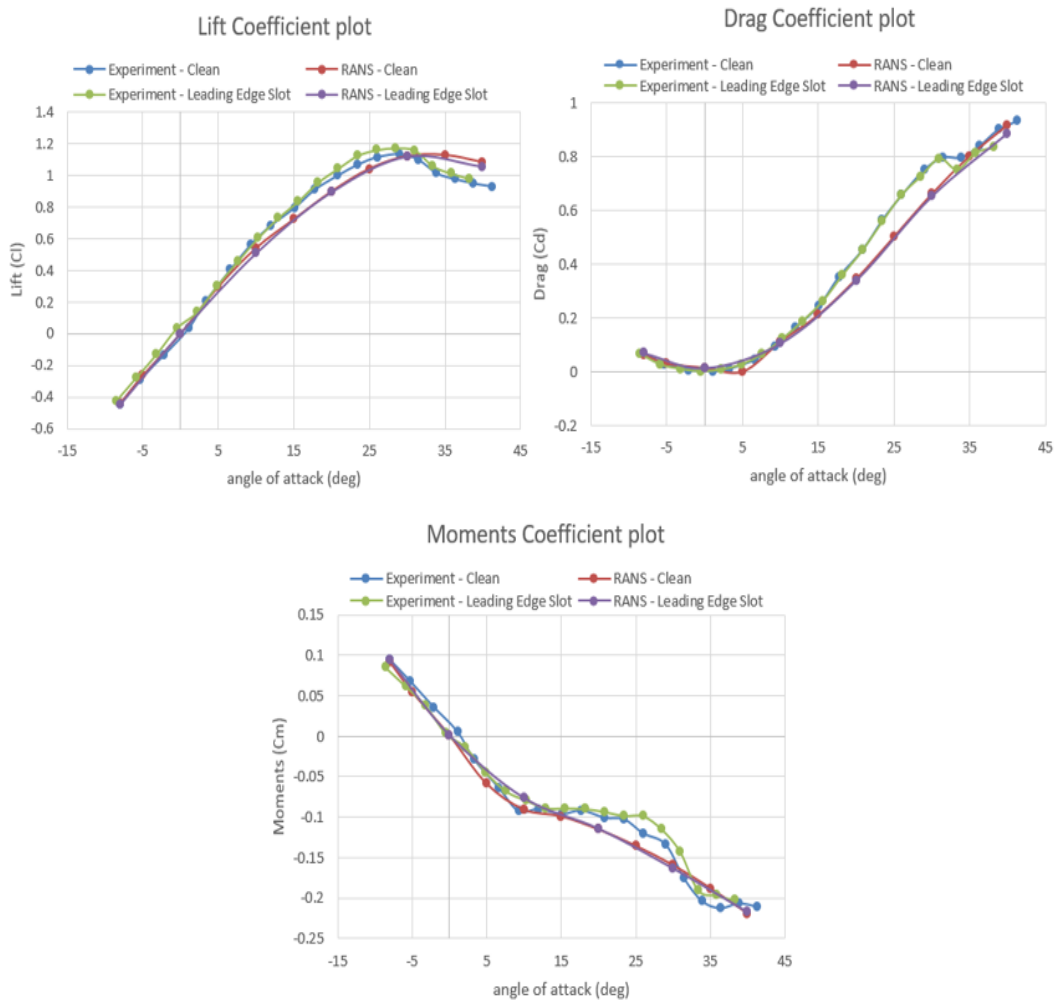

Figure 6.6: Comparison of aerodynamic coefficients and pitching moments between clean and leading-edge slot models

Although fixed slots provide same level of increase in maximum lift coefficients as moveable slots or flaps but they considerably increase the drag of air vehicle at cruise speeds (Bamber, 1939). If cavities are permanently open, the extra drag at high speeds is a disadvantage. Therefore, for high speed cruise conditions, cavities either can be fitted with a closing valve device (Lachmann, 1924), or cavities may be interconnected to control surfaces in such a way that cavities open only when control surfaces are deflected. The cavities should remain closed when control surfaces are in neutral position (Kermode, 2012). The device in question should not be in a form of a leading-edge extension as it will have an adverse effect on RCS signature. It seems probable from the results of the leading-edge cavity in Figure 6.6 that maximum lift coefficient of the device can still furthered be improved by varying the width, gap and position of the cavity in relation to leading edge of the wing. Having said that, flying wing planform experiences highly separated flows on the upper surface of the wing, and the lift will not increase unless the flow can be made to follow the curvature of the wing (Gudmundsson, 2014b). As is the case with conventional leading edge flap, a proper leading-edge cavity must be created so that it ejects a flow nearly parallel to the suction side and sits at the right position in relation to leading edge of the wing (Kermode, 2012).

As was noted earlier, the purpose of this study is not to increase maximum lift coefficient, but to create an airflow barrier on the upper side of the wing to reduce the intensity of forward migration of leading-edge vortices to the outboard sections of the wing. More airflow over control surfaces of the trailing edges of the wing will enhance the lateral control of the vehicle at moderate to high angles of attack regimes. The flowfield on the upper surface of a slotted flying wing configuration was visualised using surface

streamlines, and results were compared with clean baseline wing. The lines showing the direction of fluid flow at a particular moment are called streamlines (Kermode, 2012). A streamline is the path followed by a particle of an oil drop when air blows it in a steady airflow, but one streamline cannot cross another (J.D. Anderson, 2010). Figure 6.7 shows pressure distribution and surface streamline comparison between clean and leading-edge cavity wings at an incidence angle of 5°. When streamlines are shown together it indicates increased velocity, and when streamlines are wide apart it represents decreased velocity. When streamlines converge, it means the fluid has accelerated and it has detached from the surface of the wing. On the contrary when they diverge, it indicates decelerating airflow and the associated rise in the pressure (Johnson, 1998). It can be observed from the streamline pattern in Figure 6.7 that fluid has converged near the upper part of leading-edge cavity, thus re-energising the boundary layer and channelling more fluid towards the control surfaces which are mounted on trailing edges of the wing. The leading-edge cavity was found to be effective only for low angles of attack regime when angle of attack was in the range of $0 \leq \alpha \leq 8°$, and its effectiveness reduced considerably for medium to high angles of attack. The streamline patterns indicated that leading-edge cavity will not be a suitable method for the lateral flow control of the wing at moderate to high angles of attack when intensity of spanwise flow to the outboard sections of the wing grows in strength with angles of attack.

To control the lateral flow development of separated vortex flows on upper surface of the wing at medium to high angles of attack, a novel approach of chordwise cavity was implemented on a highly swept flying wing configuration.

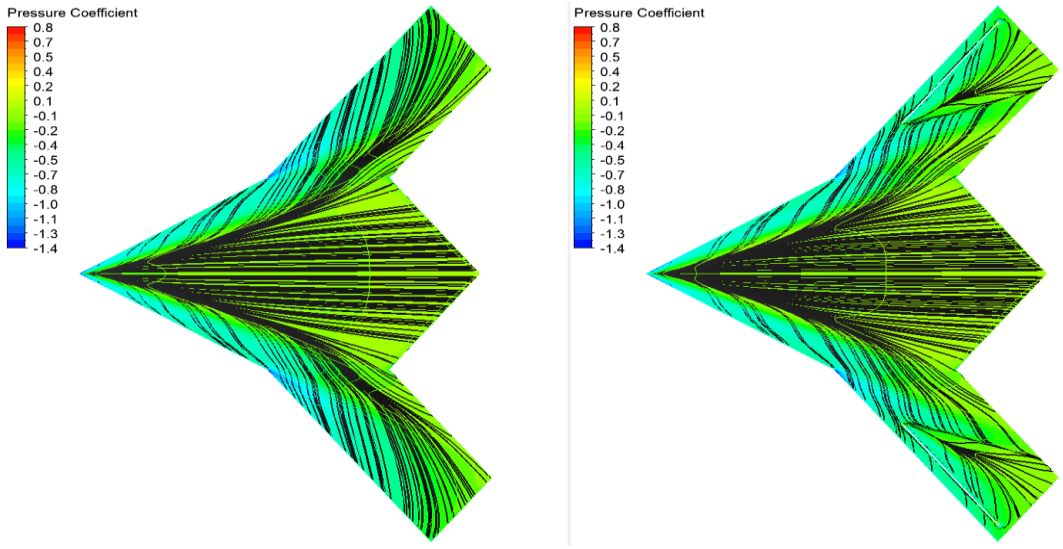

Figure 6.7: Pressure distribution and surface streamlines comparison between clean and leading-edge slot models at incidence angle of 5°

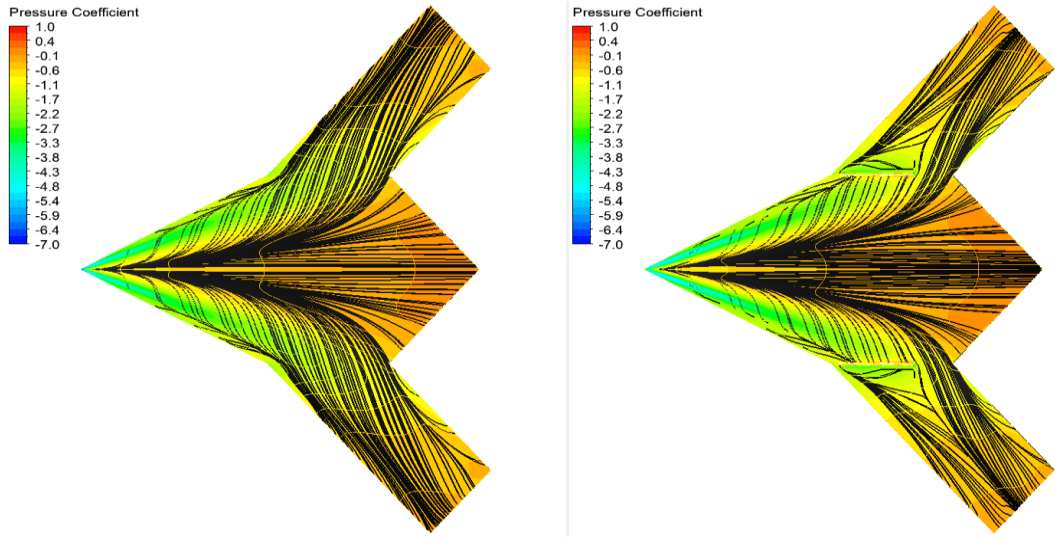

Figure 6.8: Pressure distribution and surface streamlines comparison between clean and chordwise slot models at incidence angle of 20°

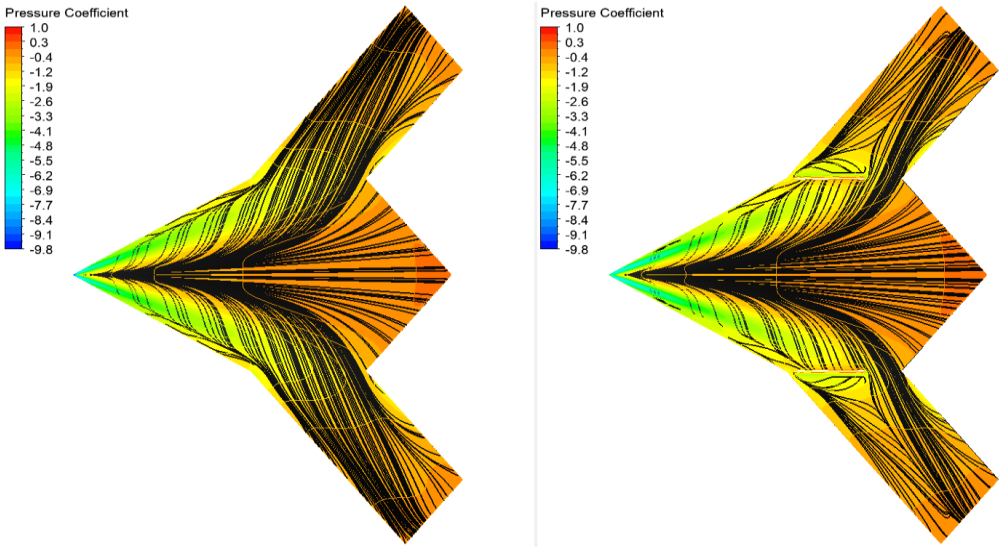

Figure 6.9: Pressure distribution and surface streamlines comparison between clean and chordwise slot models at incidence angle of 25°

As described earlier, the chordwise cavity has a width of 2mm, length of 0.1m and has chamfered edges at an angle of 45°. The research in general has focused on using fences or thin plates which project up from the wing to prevent the spanwise flow on the upper surface of a flying wing configuration. Wing fences divide the wing in separate sections, and therefore prevent the thickening of spanwise boundary layer on the upper surface of the swept wing (Barnard & Philpott, 2010). The vertical surfaces, however, must be avoided as they create a detrimental effect on RCS of the wing, and are not recommended if aircraft needs to have a stealth feature to avoid detection. The advantage of chordwise cavity is that it lies flushed with the surface of the wing, therefore it is going to have a reduced RCS signature when compared with a vertical or a deflected surface on a flying wing configuration. Figure 6.8 and Figure 6.9 show pressure distribution and surface streamline comparison between clean and chordwise cavity wings at the incidence angles of 20° and

25°. The streamline pattern shows a formation of a vortex behind chordwise cavity of the wing in both figures. This vortex stimulates the flowfields of the configuration under study in the opposite direction, and as a result more airflow is routed to the control surfaces of the wing. It can be observed from the streamline pattern that only a small amount of fluid has moved to the outboard sections of the wing, and a considerably higher amount of fluid was routed to the tips of the wing. More airflow towards the tips of the wing will result in more effective control of the spoilers of an air vehicle at medium to high angles of attack. The spoilers are vertical plates that deflect upwards to increase the drag of an air vehicle upon landing (Barnard & Philpott, 2010); (Kermode, 2012). They can also be used to enhance lateral control of air vehicle but they too can have adverse effect on RCS, therefore they should not be used when aircraft needs to avoid detection. Streamlines pattern further illustrates that higher amount of fluid has moved over to the trailing edge control surfaces of chordwise cavity wing in comparison to the clean wing. Results of flow control have indicated that chordwise cavity method can be used to limit the intensity of spanwise flow to the outboard sections of the wing at moderate to high angles of attack. If more airflow is routed over trailing edge control surfaces, the lateral control of the wing will become more effective. Therefore, it was decided that further investigations into the optimisation of chordwise slot needs to be carried out in order to maximise the effectiveness of trailing edge control surfaces.

However, before the optimisation of chordwise slot is performed it was important to determine whether chordwise slots in the wing improved the lift coefficient at high angles of attack upon the deflection of control surface. Therefore, CFD investigations were carried out to obtain the change in lift coefficients so that effectiveness of chordwise slots can be

quantified. Two sets of CFD analysis were conducted for this purpose. For the first set of CFD analysis, angle of attack was fixed at 20° while control surface was deflected from α = 5° to α = 30°. Figure 6.10 shows the difference in lift coefficients between clean and chordwise cavity wings when control surface is deflected in the range of α = 5° to 30°. For the second set of CFD analysis, angle of attack was changed from α = 15° to α = 25° while control surface was fixed at an angle of 5°. The Figure 6.11 shows the angles of attack range from α = 5° to 25° with a constant control surface deflection of 5°.

Figure 6.10: Lift difference comparison between wings with and without chordwise slot at constant angle of attack of 20°

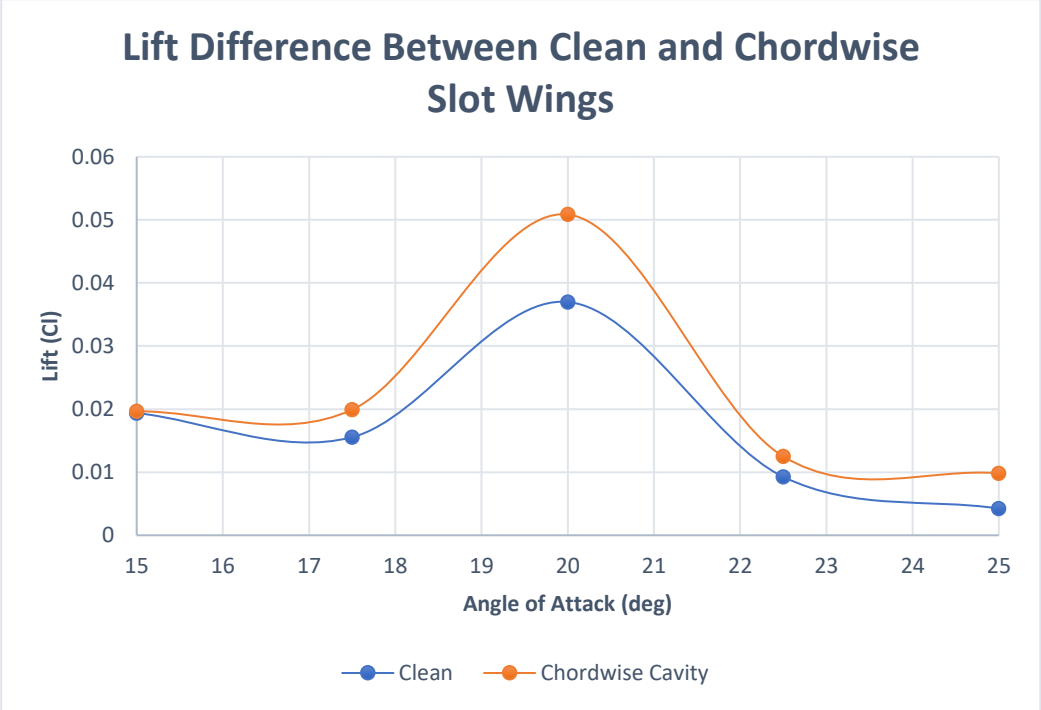

Figure 6.11: Lift difference comparison between wings with and without chordwise slots at constant control deflection of 5°

The lift difference is the increase in the lift of the wing when the control surfaces are deflected to the downside. It can be observed from the plots that the change in lift when the control surfaces are deflected increases for the wings with chordwise slot. It can be seen in Figure 6.11 that maximum difference in lift occurs at an incidence angle of 20°. It is seen that percentage increase in lift is significant over a range of angles of attack and control surface deflections but the total increase in lift is still very small. However, this still demonstrates that the operationality of the control surfaces at high angles of attack is improved when the chordwise slot is present.

In this chapter, high lift performance of a wing with leading-edge cavity was measured in low speed wind tunnel and compared with RANS predictions. This served two-fold purpose: first effect of leading-edge cavity on the high lift characteristics of flying wing configuration was analysed, second it verified the computational predictions. The leading-edge cavity did not show considerable increase in lift because swept wing considered in this study experiences highly separated flows on the upper surface of the wing. The leading-edge cavity has to be at the right position in relation to the leading edge of the wing, and the flow has to follow the curvature of the wing for the maximum lift to increase. The purpose of this study, however, was not to increase the maximum lift of the wing, but to control the development of lateral flow on the upper surface of the wing. The development of viscous lateral flow on the upper surface of the wing was visualised using streamlines. It was found that the leading-edge cavity improved the flow control for the low angles of attack regime but was ineffective for a highly swept flying wing configuration at medium to high angles of attack. In contrast, the streamline pattern for the chordwise cavity wing indicates that the lateral flow can be controlled by this approach at high angles of attack. Therefore, the chordwise cavity design was investigated further in order to control the lateral flow development at medium to high angles of attack. The second part of the chapter covers computational investigations on a highly swept wing with deflected control surface to ascertain whether chordwise slots in the wing improved the lift coefficient upon control surface deflection. It was observed that the change in lift when control surfaces are deflected increases at high angles of attack for the wings with chordwise slot.

Chapter 7. Numerical Optimisation

7.1. CFD Approach to Optimisation

In this study, gradient information for the objective function was not available, therefore Pattern Search method was implemented to optimise the chordwise cavity under study. The Pattern Search method does not require gradient information of the objective function, and it is considered more efficient than Random Search method (Chapra & Canale, 1985). The objective function depends on the certain input parameters of the problem called variables (Moler, 2004); (Ravindran et al., 2006); (El-Sayed, Sun, & Berry, 2005), and the target of the study is to find the values of variables that will maximise the objective function of the chordwise cavity. In the Pattern Search method, independent variables or parameters are changed one at a time to improve the approximation while other variables are held constant (Ravindran et al., 2006). The researchers in the past have successfully used different kinds of methods such as leading-edge flaps to add a fresh stream of air in order to overcome an excessive adverse pressure gradient of the boundary layer over the aft portion of the wing (Barnard & Philpott, 2010); (Kermode, 2012) (D. F. Anderson, 2000). Therefore, a fresh stream of air was added using a chordwise cavity in this study in an effort to overcome the adverse pressure gradient of the lateral boundary layer on a highly swept flying wing configuration.

The objective of this optimisation process was to maximise the mass flow rate normal to trailing edges of the flying wing configuration. Mass flow rate can be defined as the mass of substance that passes through a surface per unit of time. More airflow over the control surfaces of trailing edges will result in enhanced lateral control of the air vehicle at moderate to high angles of attack. In order to achieve this objective, four parameters were identified which can maximise the mass flow rate over the trailing edge of the vehicle. Those four parameters are: location, width, length and the angle of trajectory of the chordwise cavity relative to the freestream. It should be noted that the angle of trajectory of the chordwise cavity was measured with respect to the trailing edge of the wing as is shown in Figure 7.5. The strategy adopted for the optimisation process was to change one parameter at a time to improve the approximation while other parameters were held constant. As only one variable was changed at a time, the problem reduced to a sequence of one-dimensional searches that were solved using the Pattern Search method in conjunction with an interpolation method.

It should be noted that each parameter was varied over constant intervals while other three parameters were held constant. The method finds minimum or maximum of objective function for one variable at a time and thus cannot be used for global optimisation. The objective function which is mass flow rate for this study was calculated normal to the trailing edge of the wing for each step. First location of the cavity where maximum mass flow rate is produced was determined by changing the location of the chordwise cavity to 8 different positions, shown in Figure 7.1. The position of the cavity was changed over the intervals of 0.03m from the inner part of the trailing edge as is shown in Figure 7.5, while the other three parameters were held constant. Having established the

optimum location of the cavity, the width of the cavity was varied to 0.5mm, 1mm and 2mm as shown in Figure 7.2. The larger the width of the chordwise cavity the higher the drag penalty, therefore it was considered necessary to have the width of the cavity as small as possible. As a width of 2mm showed mass flow results similar to 1mm with only a marginal increase for the latter, the chordwise cavity with 1mm width was chosen for further optimisation computations. Similarly, the cavity length was altered to 0.06m, 0.08m and 0.1m as shown in Figure 7.3, and CFD computations were carried out to calculate the mass flow rate for each length adjustment. It was established that a cavity with the longest length provided the maximum mass flow rate normal to the trailing edge of the wing. The length of the cavity was not increased any further in order to provide sufficient room for the installation of trailing edge control surfaces. Finally, the trajectory angle of the chordwise cavity was varied from $\theta = 50^{\circ}\ to\ 140^{\circ}$ with respect to the trailing edge of the wing, while the other three optimised parameters were held constant. Figure 7.4 shows some of the cavity angles investigated for the optimisation process. It should be noted that the mass flow rate was calculated and compared for each step, and only the maximum value of the mass flow rate was used to compute the next parameter of the optimisation process.

After going through the first iteration of CFD computations to find best parameters of the chordwise cavity, it was established that a cavity with the following parameters will generate maximum mass flow rate normal to the trailing edge of the wing: the location of the cavity was at location 2 and in terms of distance it was placed at 0.03m from the inner edge of the trailing edge of the wing as shown in Figure 7.5, the width of the cavity was $w = 1mm$, length of cavity was $l = 0.1m$, and the cavity was inclined at an angle of $\theta =$

130° with respect to the trailing edge as shown in Figure 7.5. The same process was repeated for the second iteration of CFD computations but the dimensions of the parameters that were obtained during first iteration of CFD computations did not change, so the procedure had found best possible solution after one iteration of computations. Therefore, CFD computations were carried out on the chordwise cavity with the optimised parameters shown in Figure 7.5, and the results were compared with the clean wing.

It should be noted that mass flow rate for each parameter was calculated by inserting three lines along the trailing edge of the wing as shown in Figure 7.6. The three lines in question were placed at the distance of 2mm, 4mm and 8mm from the surface of the wing, and 30 data points were collected for each line along the trailing edge. First, average normal velocity of the lines was calculated using the following relationship:

$$U_n = Ucos\theta + Vsin\theta \qquad \textbf{(7.1)}$$

where U_n in the above equation is the average normal velocity, and θ was calculated to be 32.7° for the wing under study. The average normal velocity was then converted into mass flow rate by multiplying it with density of air, and the area of three lines over the trailing edge of the wing. The lines were placed at these locations to collect data close to and further away from the surface of the wing. This was done to get better understanding of flowfield in these regions.

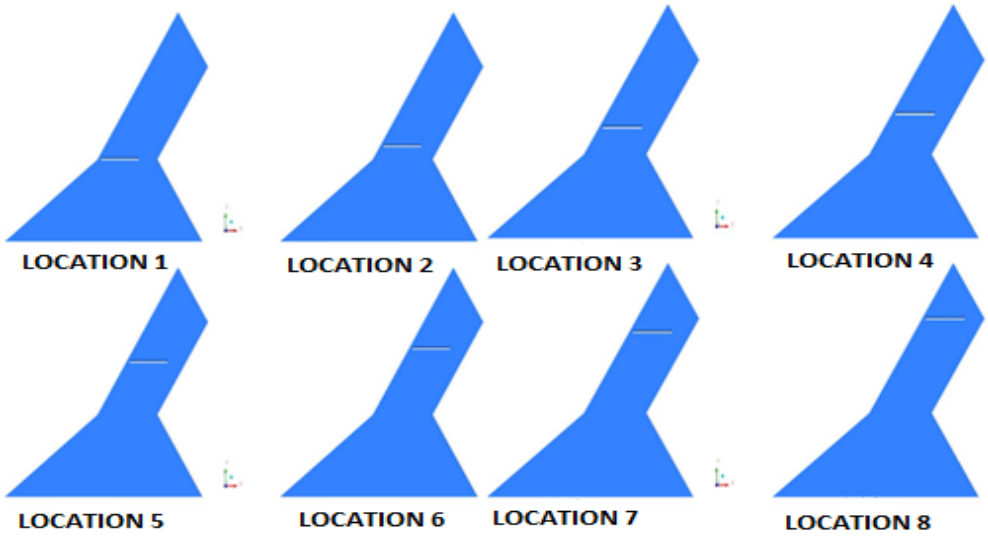

Figure 7.1: Positions of chordwise slot for the optimisation analysis, Locations 1 - 8

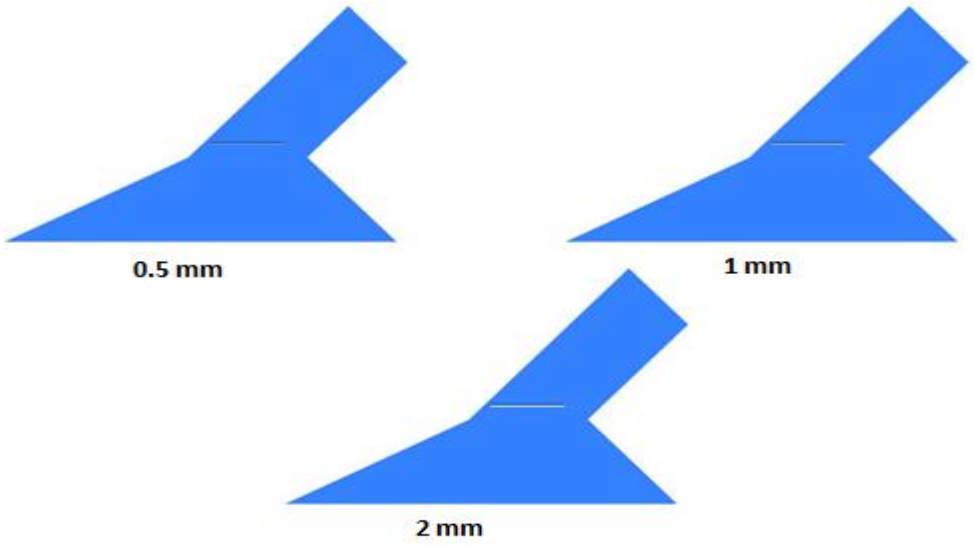

Figure 7.2: Widths of chordwise slot for the optimisation analysis, 0.5mm - 2mm

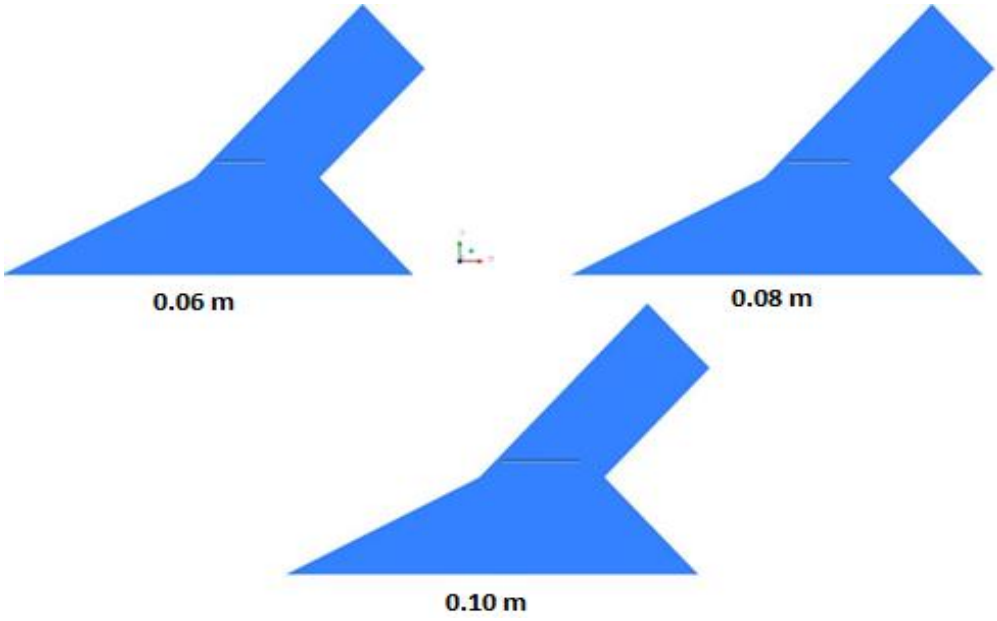

Figure 7.3: Lengths of chordwise slot for the optimisation analysis, 0.06m - 0.10m

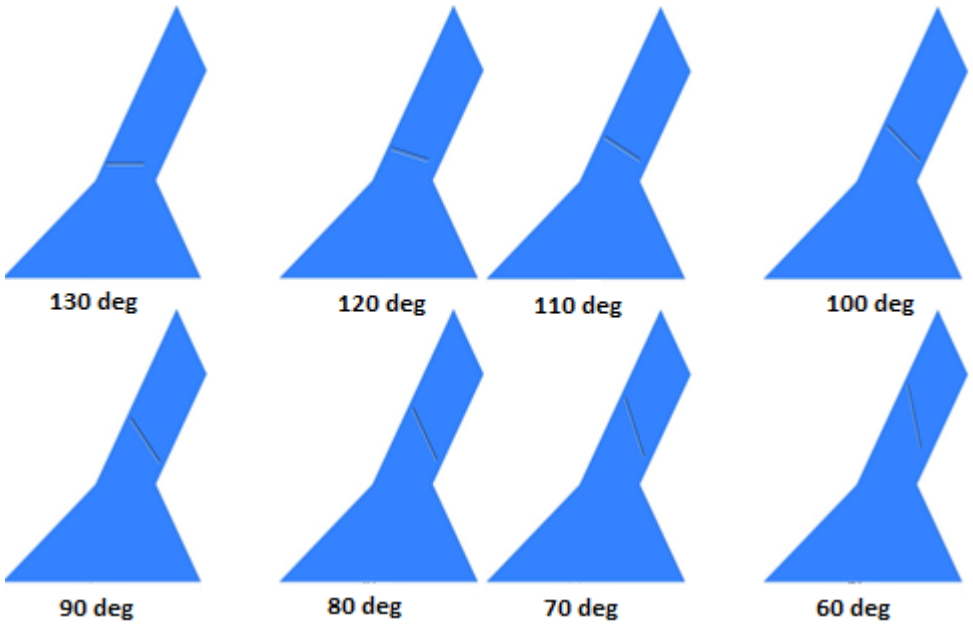

Figure 7.4: Angles of chordwise slot with respect to trailing edge for the optimisation analysis, 130° - 60°

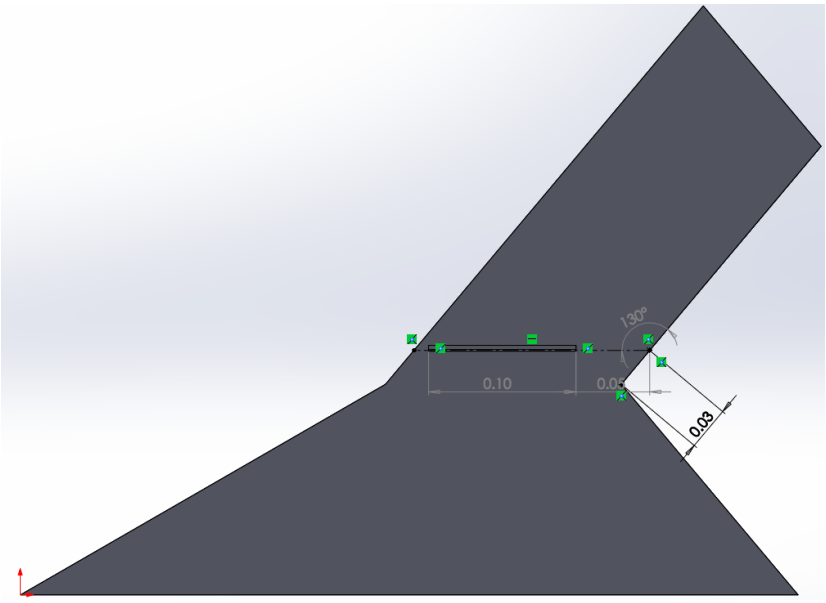

Figure 7.5: Dimensions of optimised chordwise slot

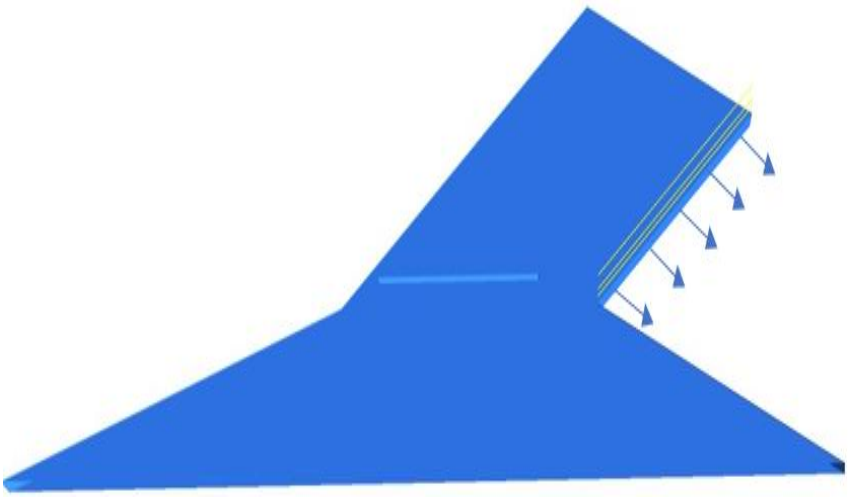

Figure 7.6: Horizontal lines on the trailing edge of chordwise slot wing that were used to calculate mass flow rate of the wing

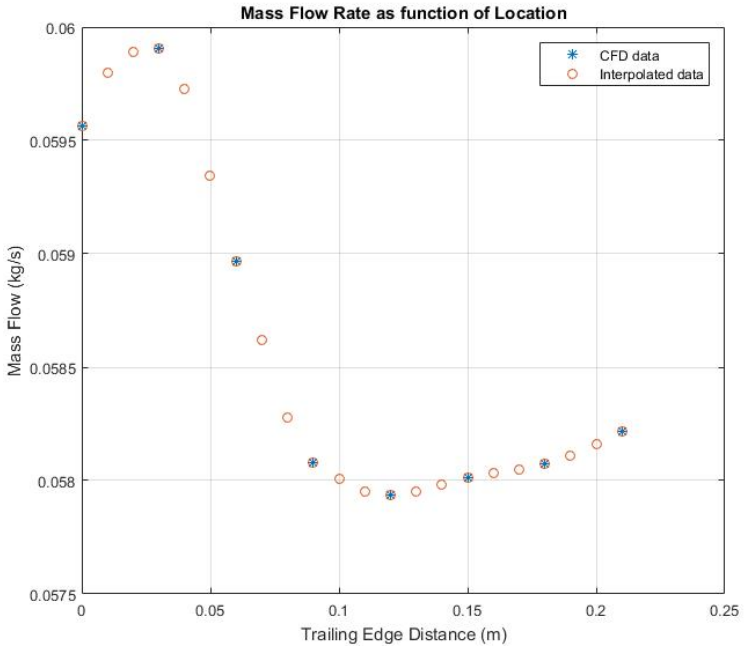

Figure 7.7: Mass flow rate as a function of location with interpolated data

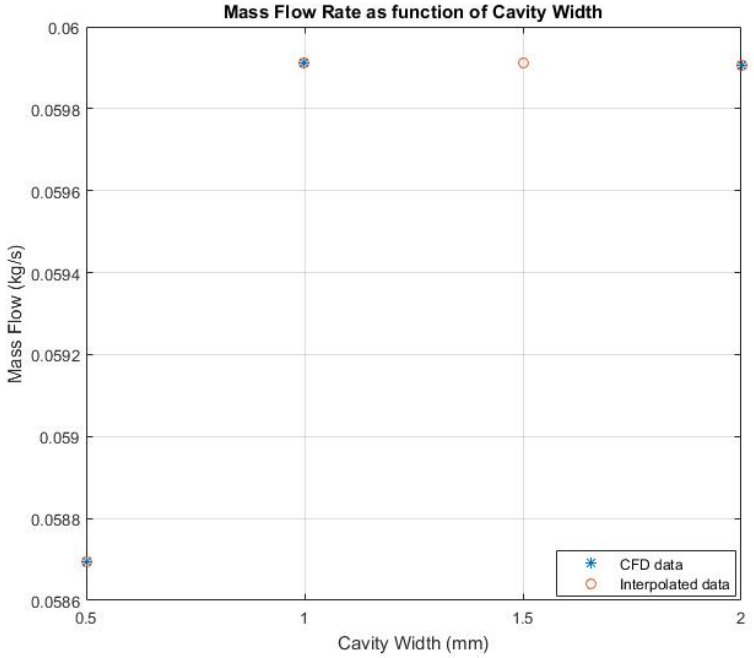

Figure 7.8: Mass flow rate as a function of location with interpolated data

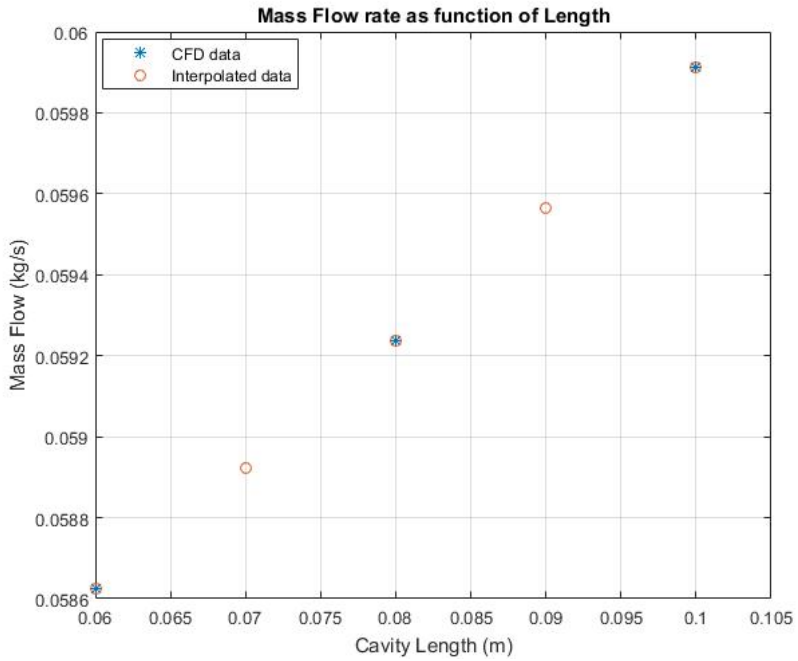

Figure 7.9: Mass flow rate as a function of length with interpolated data

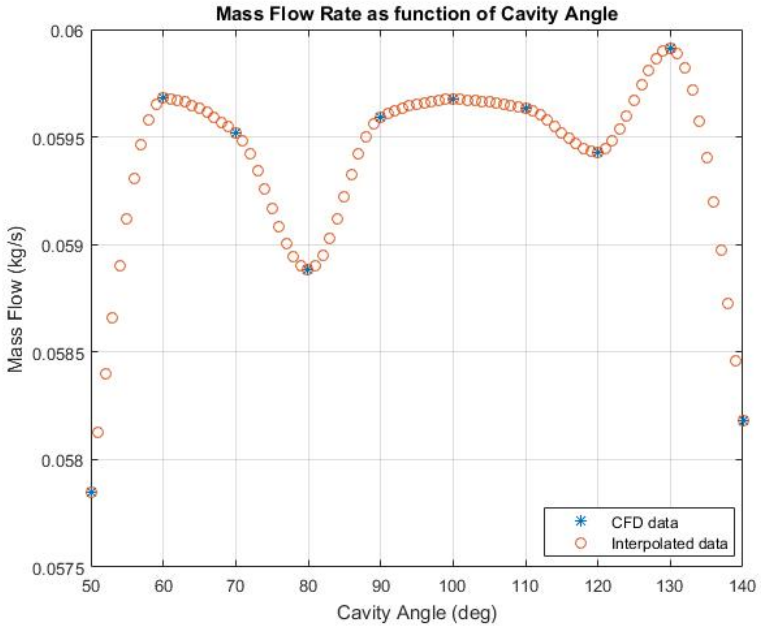

Figure 7.10: Mass flow rate as a function of cavity angle with interpolated data

Three lines as opposed to one were used to get better understanding into behaviour of flow over a bigger region of the trailing edge surface. As noted earlier, first the average normal velocity of the lines was calculated as is depicted by the arrows in Figure 7.6, and then it was converted into mass flow rate. Pattern Search method in conjunction with an interpolation code was used to determine the optimum parameters for the optimisation of the chordwise slot. An interpolation code was written in Matlab for the optimisation problem of the chordwise cavity to estimate the values between known CFD data points. Matlab function “pchip” was implemented for the interpolation of the data. The acronym pchip stands for “piecewise cubic Hermite interpolating polynomial”, and it was developed by Fred Fritsch and his colleagues around 1980 but the function was made part of Matlab in early 90s (Moler, 2004). If both function values and first derivative is known for a set of data points, then piecewise cubic Hermite interpolation can be used to reproduce the data (Moler, 2004). The Matlab function pchip is a shape preserving interpolant which never overshoots the data locally. The behaviour of pchip slope is determined by two data points on either side of a particular interval and the function ignores the points further away (Moler, 2004). The results of mass flow rate for all four parameters with interpolated data points are shown from Figure 7.7 to Figure 7.10. It should be noted that these mass flow rate results were obtained by placing three lines at the distance of 2mm, 4mm and 8mm on the upper surface of the wing. The bottom surface of the wing showed negligible difference in mass flow rate between clean and chordwise cavity wings, therefore bottom surface was ignored at this stage of optimisation process. The maximum value of mass flow rate for each parameter in the above charts was used to design an optimised chordwise cavity to control the spanwise flow of the wing. The computational results of the optimised

chordwise cavity model were compared against the baseline clean wing to understand the effect of chordwise slot on mass flow rate over the trailing edge of the wing.

7.2. Computational Details of Optimised Wings

The results obtained from Pattern Search optimisation were used to design two optimised chordwise cavity wings and their results were compared against clean configurations. One of the chordwise cavity wings is a flat plate model and other one is based upon Gottingen 444 (GOE444) aerofoil profile sections shown in Figure 7.11. Three wings with different aerofoil sections were computationally analysed for this study, but GOE444 was chosen for the purpose of optimisation as it produced results similar to the flat plate wing. It should be noted that clean wings in this study have identical grid sizes and CFD setup to chordwise cavity wings so that computational solutions can be compared with reasonable confidence. The highly separated flowfield of flying wing configurations coinciding with the development of lateral flow on the upper surface of the wing make it challenging to predict and analyse the flow physics accurately. Fluent solver was used to calculate compressible, three dimensional Reynolds Averaged Navier-Stokes equations in a cell centred Finite-Volume formulation to predict and analyse the flowfield of flying wing configurations in this study. As the flowfield for these configurations is highly turbulent, Spalart-Allmaras (S-A) turbulence model was used to close the governing form of the equations. In the following sections, information regarding setup of CFD computations will be provided and results will be compared with clean wings.

7.2.1 Geometry and Mesh Details

The CAD models of both flat plate and GOE444 configurations were created in Solidworks, and are shown in Figure 7.11. Geometrical parameters of this highly swept flat plate configuration are provided in section 3.2.1 of this thesis. It should be noted that the wing with thickness has identical geometric parameters as configuration 2, but is comprised of a Gottingen 444 (GOE444) aerofoil profile sections. GOE444 is a symmetrical aerofoil and has a maximum thickness of 5.6% at 30% chord. The aerofoil section has a blunt leading-edge which promotes separated-vortex flows at moderate to high angles of attack, resulting in enhanced lift generation. The planform has a leading-edge sweep of $\Lambda = 60^{\circ}$ and trailing edges has a sweep of $\Lambda = 40^{\circ}$. The optimised chordwise cavity has a width of $w = 1mm$, length of $l = 0.1m$, and it is inclined at an angle of $\theta = 130^{\circ}$ with respect to trailing edge of the wing. The edges of the cavity are chamfered at an angle of 45° in order to aid the airflow so that it flows from the lower to upper surface of the wing. The GOE444 wing has fillet edges of 2mm radius with a circular profile on the edges of its chordwise cavity. In this study, ANSA grid generator was used to create structured multiblock meshes around flat plate wing, and ICEM was used to generate unstructured grids around GOE444 wing. Only half span of models was meshed because symmetric boundary conditions are considered for both clean and chordwise cavity wings. The size of the computational domain was 10 times the chord length of the wings in all directions. In order to capture boundary layer effects, the height of the first cell normal to the solid surface was close enough to ensure suitable Y^{+} values on all grids in this study. Higher cell resolution was used on the leading edges of the wings in order to correctly resolve the onset of vortical structures.

Mesh parameters of all computational grids used in this section for optimisation study are provided in Table 7.1. Multiblock structured grids were generated for flat plate wings and unstructured grids were used to mesh the wings with GOE444 aerofoil sections. For structured multiblock grids, the height of the first cell normal to the surface of the wing was 3×10^{-6}m, yielding Y^+ values of approximately 1. The grids in question have a growth rate of 1.34 providing approximately 2.6 million cells as shown in Table 7.1. The chordwise cavity wing also has a Y^+ of approximately 1 with the exception of a small part on the edge of the cavity. The first cell spacing for unstructured grids normal to solid surface was 4×10^{-7}m. The growth rate of 1.40 with 20 layers of prism mesh provided maximum Y^+ values of approximately 1, shown in Table 7.1. It should be noted that Y^+ values for both flat plate and aerofoil chordwise cavity wings were observed to be higher than 1 in very small section of the cavity. The Figure 7.12 and Figure 7.13 show Y^+ values of higher than 1 only on the edges of chordwise cavity, while rest of the wings surface has Y^+ values below 1 for both flat plate and GOE444 chordwise cavity wings. The mesh topology used for multiblock structured grid was very similar to the topology used for clean wings in section 3.2.1 of this thesis. The basic topology of unstructured grids used for GOE444 wings is shown in Figure 7.14.

Figure 7.11: Flying wing configurations with optimised chordwise slot: Flat plate model (left); GOE444 aerofoil profile wing (right)

Model	Mesh Type	Cells	Growth Ratio
Clean – Flat Plate	Structured	2620144	1.34
Cavity – Flat Plate	Structured	2677550	1.34
Clean – GOE444	Unstructured	2012051	1.40
Cavity – GOE444	Unstructured	2070888	1.40

Table 7.1: Mesh parameters of Flat Plate and GOE444 wings used for computational analysis

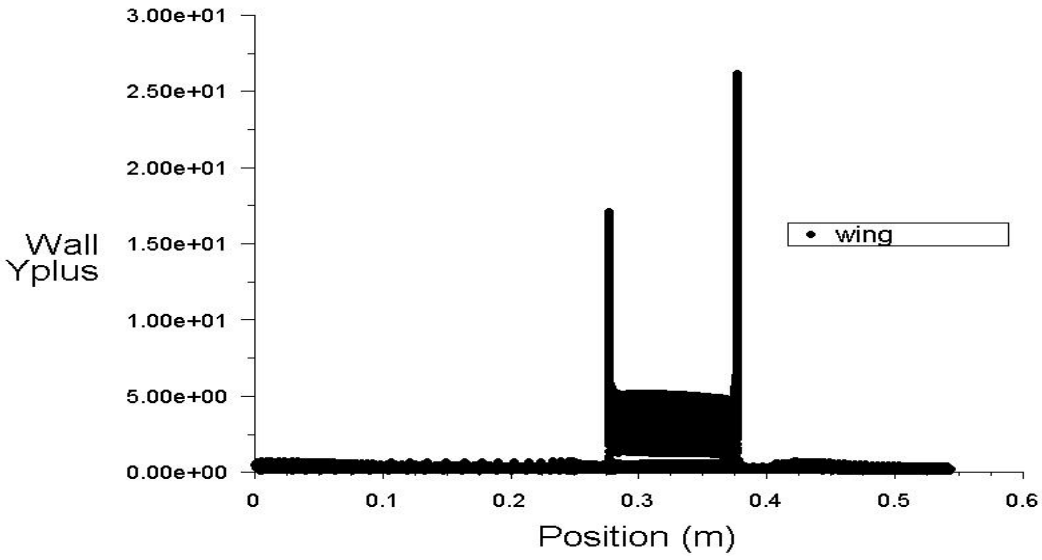

Figure 7.12: Y^+ values for optimised flat plate slot wing at incidence angle of 30°

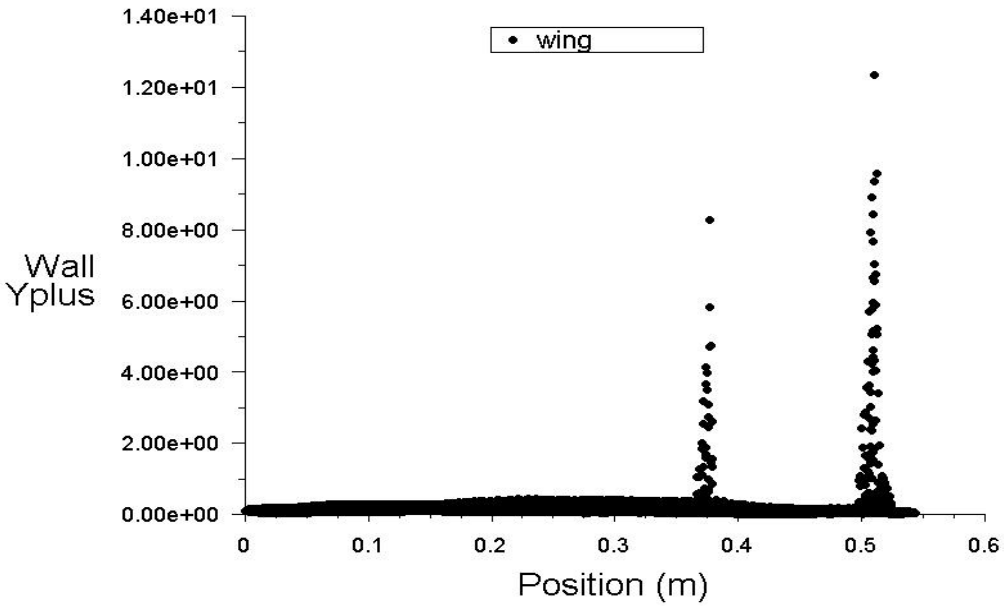

Figure 7.13: Y^+ values for optimised GOE444 slot wing at incidence angle of 30°

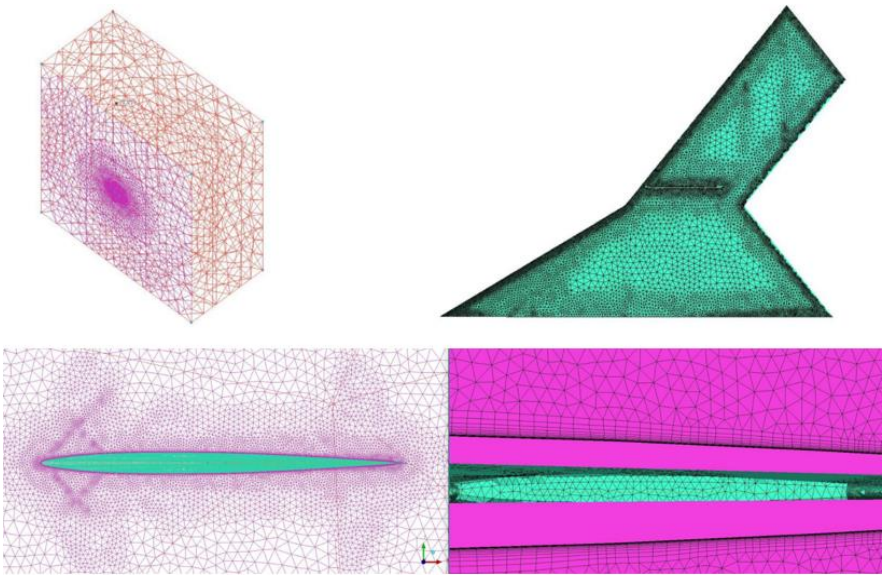

Figure 7.14: Topology of unstructured grid for GOE444 wing

Prism mesh was generated near the surface of the wing for these unstructured grids in order to efficiently resolve the effects of the boundary layer. Tetrahedral elements are used to resolve the space between final layer of prisms and the outer far field boundary. Unstructured grid has a smooth transition from a finer grid with elements of small sizes near the surface of the wing to a coarse grid with elements of bigger sizes at the far field boundary regions as shown in Figure 7.14.

7.2.2 Solver Settings

Low speed CFD computations were set to match the free stream conditions of the wind tunnel experiment. Density based solver in Fluent was used to for the all the computations of optimisation problem in this study. Parallel processing capabilities of the solver were used on local machines to reduce the computation time. Air was used as a fluid with density following the ideal gas law and viscosity of air was computed with thee coefficient method of Sutherland law. For the computations of optimisation analysis, three kinds of boundary conditions have been used: symmetry for the plane of symmetry, the wall boundary with no slip condition was imposed on the surface of wing and Pressure far field boundary was used for rest of the domain. One equation Spalart-Allmaras turbulence model was used to solve all the computations of the optimisation problem. Second order upwind scheme has been used for the spatial discretisation with Roe-FDS as flux type. Standard initialisation was computed from far field boundary condition. The steady state solution was calculated in an iterative manner and convergence criteria was set to be 10^{-4} for all optimised and clean wing computations. Although, all the computations achieved a minimum convergence criterion of 10^{-4}, but aerodynamic coefficients and moments were also monitored in order to ensure the convergence of solution as shown in Figure 7.15.

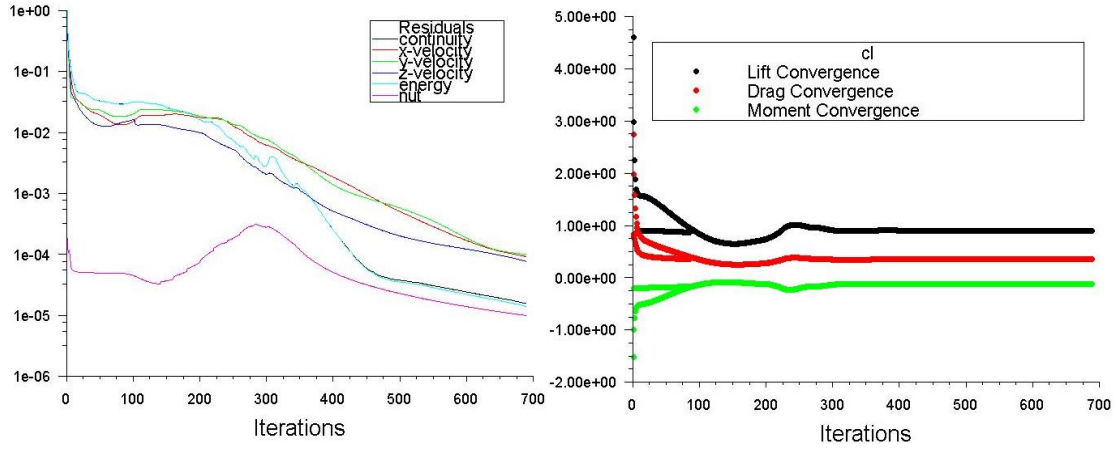

Figure 7.15: Convergence monitors for optimisation analysis: Residual convergence (left); Lift, Drag and Moments (right)

For the optimisation analysis, all computations were calculated using solution steering with full multi-grid initialisation for faster convergence. Solution steering automatically updates the courant number considering residual positions during the simulation and as a result computation time is reduced considerably.

7.3. Optimisation Results and Discussion

In this section, CFD RANS and experimental results are presented for optimised chordwise cavity wings and compared against the clean wings. As noted earlier, similar mesh sizes and CFD setup was used for both clean and chordwise cavity wings so that results can be compared with a reasonable certainty. Freestream conditions were initially provided by wind tunnel tests where Mach = 0.1 and Reynolds number = 5×10^5, and CFD computations were set to match the conditions of wind tunnel tests. The Reynolds number is based on

aerodynamic mean chord length of planforms being investigated in this study. The root chord of the model is 0.528m long and the moment reference point is located at 0.2277m from the apex of the wing. Aerodynamic coefficients and moments are scaled using the reference area, S_{ref} = 0.0906m^2, and reference chord, C_{ref} = 0.37m. We are only interested in the analysis of medium to high angles of attack for the study of optimisation problem, as spanwise flow separation on outboard sections of swept wing vehicle severely affects the manoeuvrability of control surfaces of the vehicle at this incidence angles range (Barnard & Philpott, 2010); (Shevell, 1989). Therefore, we are less interested in the optimisation of the flying wing configuration at low and post stall angles of attack regimes.

The lines used to calculate mass flow rate normal to the trailing edge on upper and bottom surfaces of the wing are shown in Figure 7.16. The results of mass flow rate calculated on the trailing edge of the wing for flat plate cavity model are shown in Figure 7.17 and compared with the clean model. It was noticed that there was a negligible difference in mass flow rate on the bottom surface of the wing between clean and chordwise cavity wings. However, for accuracy purposes the values of mass flow rate obtained from the bottom surface of the wing were added to the mass flow data of the upper surface of the wings to obtain the total mass flow rate for clean and slotted wings as shown in the Appendix of mass flow rate calculations. The objective of the optimisation process is to maximise the mass flow rate of the entire wing, as it is the mass flow rate that enhances the manoeuvrability of the control surfaces. As noted earlier, three lines were placed at the distance of 2mm, 4mm and 8mm from the surface of the wing to compare the mass flow rate of the clean and chordwise cavity models on the trailing edge of the wing.

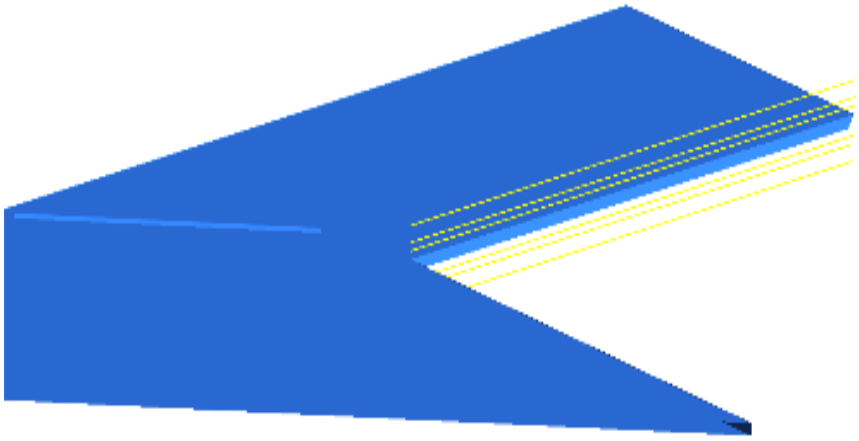

Figure 7.16: Horizontal lines along trailing edge on top and bottom surfaces of the model

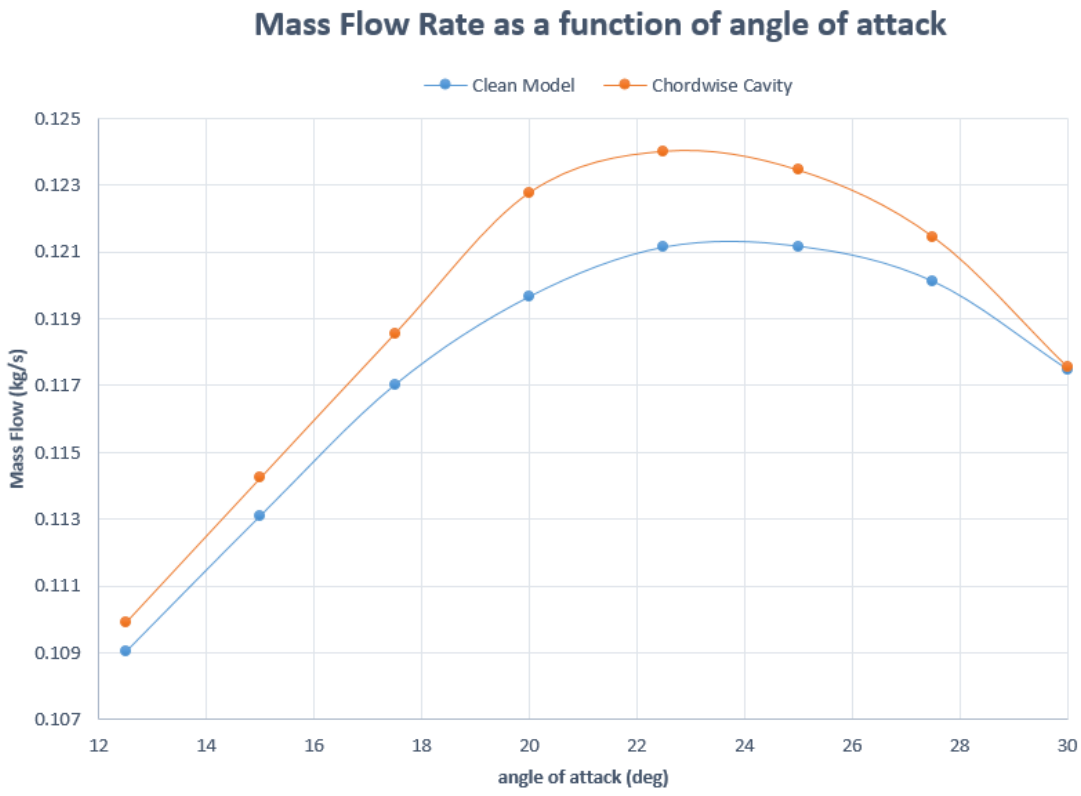

Figure 7.17: Mass flow rate comparison between clean and chordwise cavity flat plate wings

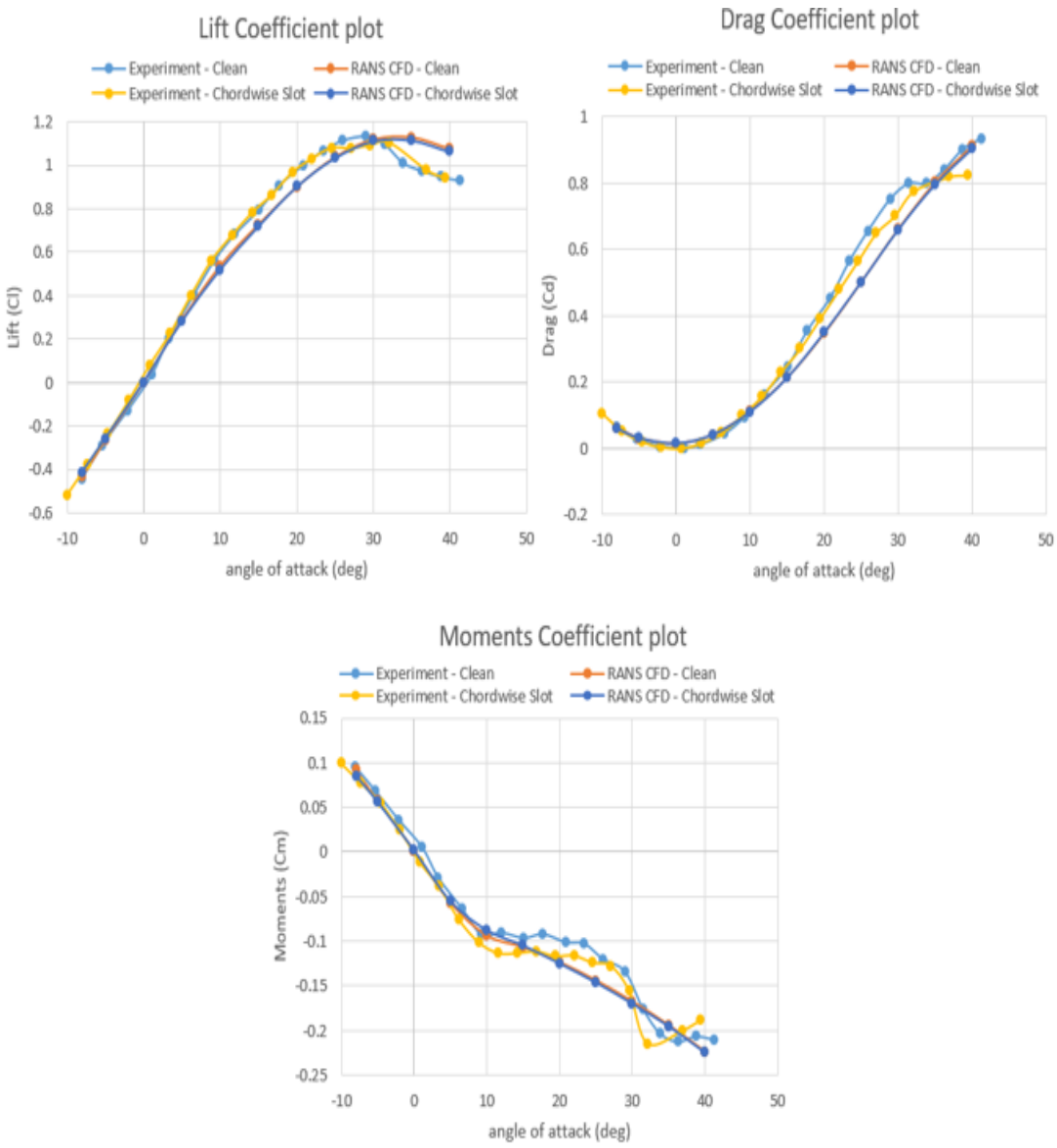

Figure 7.18: Aerodynamic coefficients and moments comparison between clean and optimised chordwise cavity flat plate wings

Mass flow rate was measured as functions of angles of attack ranging from 12.5° ≤ α ≤30° with an incidence angle interval of 2.5°. It can be seen in Figure 7.17 that there is a considerable increase in mass flow rate for the wing with chordwise cavity in comparison to the clean wing. The mass flow rate is consistently higher for the cavity wing for all angles

of attack, ranging from moderate to high angles of attack and then eventually drops down at the incidence angle of 30°. The maximum difference in mass flow rate between clean and cavity wings was observed to be at the incidence angle of 20°. The mass flow rate increased with angle of attack prior to incidence angle of 20° and then decreased with angle of attack, eventually levelling off at stall incidence angle of 30°. It should be noted that the wing under study stalls at incidence angle of 30°, as was shown in Chapter 4 of this thesis. The post stall flowfield is not of interest for optimisation analysis as we are trying to make control surfaces more effective only at medium to high angles of attack. The Figure 7.17 demonstrates that the chordwise cavity design can be implemented on a flying wing configuration as it successfully controls the lateral flow by maximising the flow rate over the control surfaces of the trailing edge.

It should be noted that lateral control contributed by control surfaces of the vehicle becomes restricted only at moderate to high angles of attack, therefore only such angles of attack were considered for the optimisation investigations. Aerodynamic coefficients and moments for optimised chordwise cavity wing were computed as functions of angles of attack using RANS, and results were compared with experiment as shown in Figure 7.18. The purpose of carrying out experimental investigations to measure aerodynamic forces and moments of a chordwise cavity wing were two-fold: first to verify the solutions of optimisation computations, second to understand the effect of chordwise cavity on aerodynamic forces and pitching moments of the wing. Figure 7.18 shows angles of attack range from α = -10° to 40°, and it can be observed that RANS predicts the overall trend of aerodynamic forces and moments quite well. Although general trends of RANS predictions compare well with the experiment, aerodynamic forces and moments predictions follow

the experiment curves closely for angles of attack below 10°. For incidence angles above 10° RANS predictions show a small reduction in force coefficients. Similarly, small offset in the predicted values was observed for the pitching moments curve. This small discrepancy in aerodynamic coefficients and moments could be due to the under prediction of vortex strength by the turbulence model. As regions of separated flows become more noticeable at high angles of attack, aerodynamic coefficients and moments become difficult to predict with absolute accuracy by the RANS method.

Although flat plate wing was able to successfully increase the mass flow rate over control surfaces of the trailing edge, but it was considered important to analyse the capability of chordwise cavity design on a wing with aerofoil sections, as the flowfield of a flat plate model can differ from a wing with aerofoil sections. Therefore, RANS computations are conducted on three clean wings with different types of aerofoil sections, and results are compared against experiment of flat plate model as shown in Figure 7.19. It should be noted that the geometry of the wings with aerofoil sections was based upon flat plate model, termed configuration 2 in this study. The Figure 7.19 shows RANS predictions of aerodynamic forces and moments of a flat plate wing and two aerofoil wings GOE444 and NACA0008, and results of the RANS predictions are compared with the experiment. Aerodynamic forces and moments were measured as functions of angles of attack ranging from $-8° \leq \alpha \leq 40°$. The results shown in Figure 7.19 are obtained using unstructured grids, and it can be noticed that RANS solutions with unstructured grids are not as well predicted as structured grids. Although, RANS method has again predicted the overall trends quite well, but bigger difference in experiment and RANS predictions can be noticed at high angles of attack for unstructured grids than structured grids. It can be observed from Figure

7.19 that configuration based upon GOE444 aerofoil sections has similar aerodynamic forces to flat plate model, but the wing based upon NACA0008 aerofoil sections shows considerable decrease in lift and drag coefficients. This could be due to the shape of the leading edge of the GOE444 wing. As GOE444 wing has a sharp leading edge that is similar to the flat plate model, this results in the formation of a strong leading-edge vortex with high velocity gradients on the upper surface of the wing. It was illustrated in literature review of this thesis that high lifts achieved by swept wings is mainly due to the formation of leading-edge vortices on the upper surface of the wing. The leading-edge shape of the NACA0008 aerofoil section is more rounded in comparison to flat plate and GOE444 wings, thus vortex formation on the upper surface of the wing is limited in strength. The weak vortex on the upper surface of the wing results in lower lift for NACA0008 wing when compared with lift coefficients of flat plate and GOE444 wings. Pitching moments predicted by RANS in Figure 7.19 show a small offset for GOE444 wing, and a higher offset for NACA0008 wing at moderate to high angles of attack. The trend of the predicted pitching moments matches closely to the experiment curve. As GOE444 wing was able to achieve higher lift and produced results similar to flat plate model, it was considered more appropriate choice for the investigation of chordwise cavity design.

Mass flow rate for GOE444 wing was calculated using identical method to flat plate model described earlier in this section. Three lines were placed at the distance of 2mm, 4mm and 8mm from the surface of the wing, and mass flow rate was calculated normal to trailing edge of the wing. The angles of attack considered for optimisation range from $\alpha = 12.5°$ to 30°.

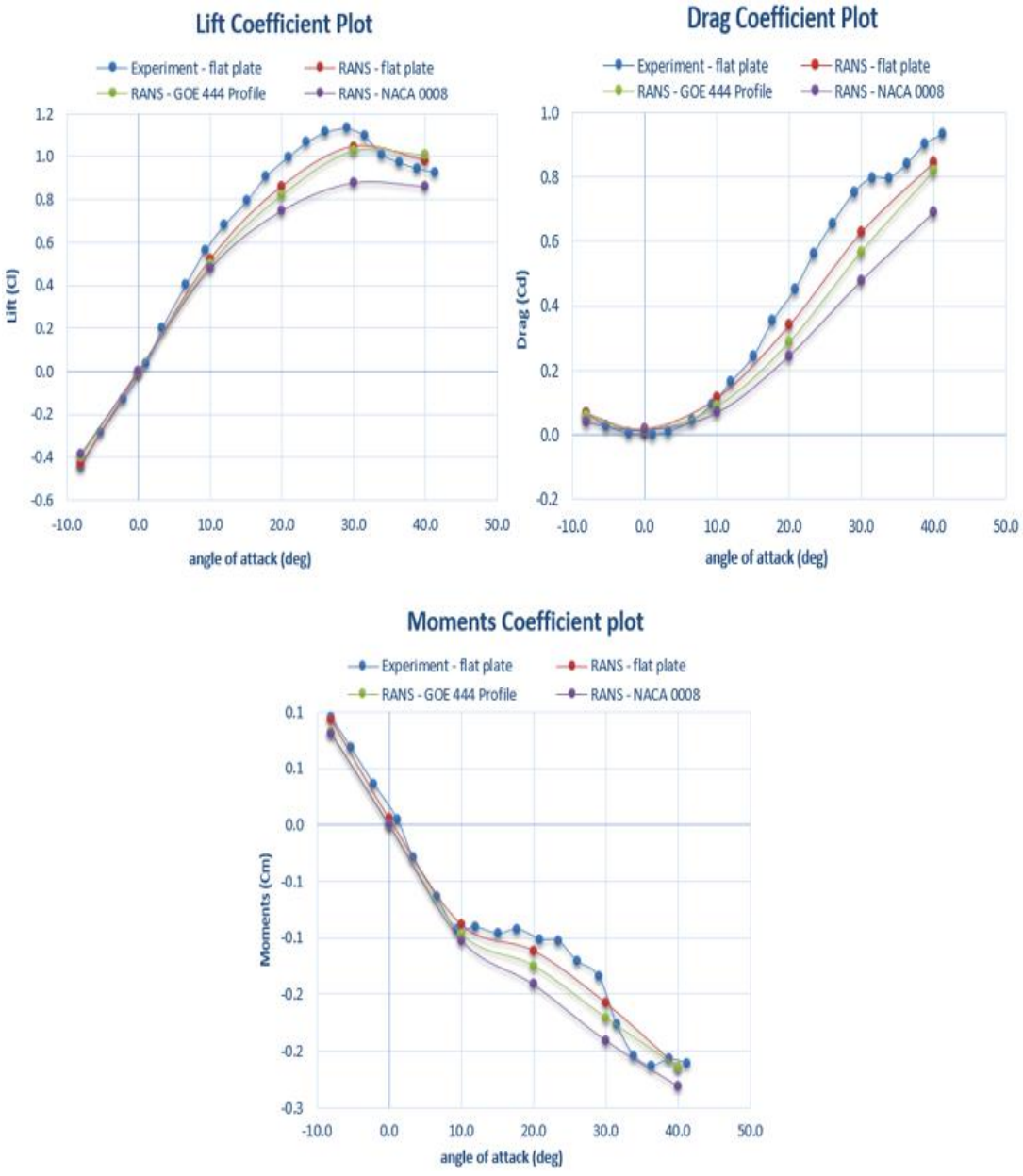

Figure 7.19: Aerodynamic coefficients and moments comparison between clean and chordwise cavity for flat plate, GOE444 and NACA0008 configurations

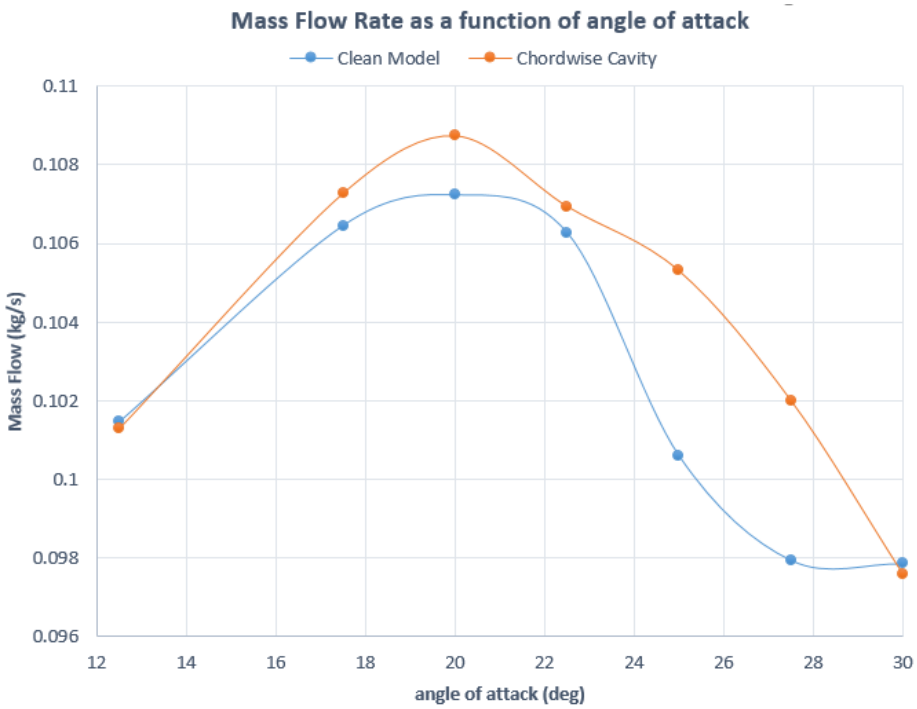

Figure 7.20: Mass flow rate comparison between clean and chordwise cavity models for GOE444 aerofoil sections

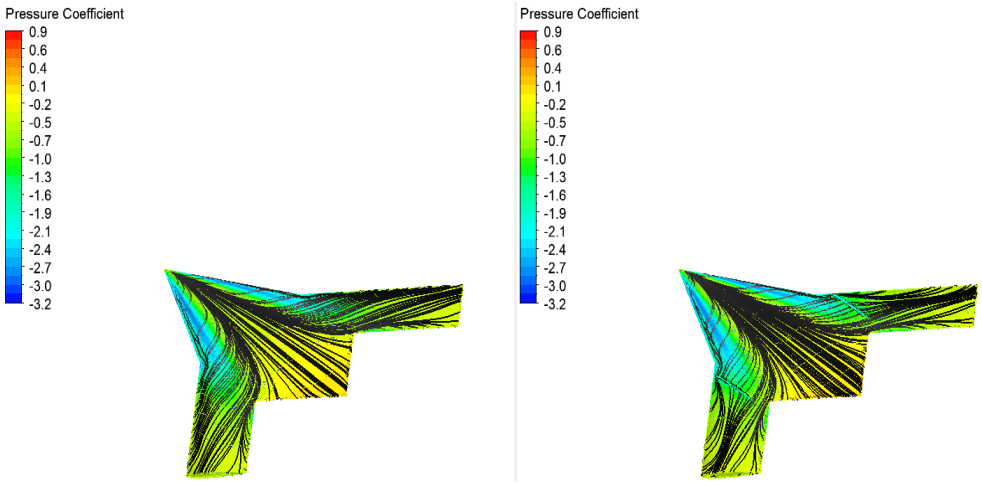

Figure 7.21: Pressure distribution and surface streamlines comparison between clean and chordwise cavity for GOE444 wing at angle of attack of 20°

It should be noted that lines to calculate mass flow rate were placed at same location as flat plate model, and mass flow rate was calculated for GOE444 clean and GOE444 chordwise cavity wings. The Figure 7.20 shows the mass flow rate comparison between clean and chordwise cavity wings. It can be observed that there is a considerable increase in mass flow rate for the wing with chordwise cavity in comparison to the clean wing. The maximum difference in mass flow rate between clean and chordwise cavity wing was noticed at the incidence angle of 24.5°. There is a significant increase in mass flow rate above incidence angles of 17.5°, but a dip in mass flow rate was observed at incidence angle of 22.5°. It was considered important to implement the chordwise cavity design on a wing with aerofoil sections to test the capability of the design to control the lateral flow development on a highly-swept wing. Figure 7.20 demonstrates that chordwise cavity method can be implemented on flying wing configurations to enhance lateral control of air vehicle as it can increase the mass flow rate over the trailing edge control surfaces. Figure 7.21 depicts surface streamline comparison between chordwise slot and clean GOE444 wings on the upper surface of the wing at an incidence angle of 20°. The streamline patterns show that spanwise flow for the wing with chordwise slot is considerably less intense, as slot routes more airflow to the trailing edges and tips of the wings. More airflow over trailing edge control surfaces and spoilers results in enhanced lateral control of the air vehicle.

In this chapter, a novel optimised design for a wing with chordwise cavity was developed to maximise the flow rate at the trailing edges of highly swept flying wing configuration. The mass flow rate results show that wings with the chordwise cavity has successfully increased the mass flow rate of flat plate and GOE444 wings. Considerable increase in mass

flow rate for chordwise cavity wings was observed when results were compared against clean wings. Only moderate to high angles of attack range was considered, as lateral flow of flying configurations effects the manoeuvrability of control surfaces in this range. The computational details of clean and chordwise cavity wings used for optimisation study have been also been provided in this chapter. High lift performance of chordwise cavity wing was computed using RANS method and results were verified with experiment. This served two-fold purpose of elucidating the effect of chordwise cavity design on aerodynamic forces and moments of highly swept wing, and provided experimental data for the validation of optimisation computations. The aerodynamic forces and moments of flat plate chordwise cavity model were compared with the clean model, and it was observed that highly separated flowfield of the flying wing configuration did not make considerable impact on forces and moments of the wing. The predicted aerodynamic forces and moments agree well with the experimental data measured in low speed wind tunnel.

Chapter 8. Conclusion

In this study two main research topics were addressed. The first was to predict and compare high-lift performance of two low observable UCAV configurations using high and low fidelity numerical techniques, and to enhance our understanding of viscous lateral flow development over a highly-swept UCAV configuration. It has been shown that reasonable predictions can be made using RANS and Euler, as results obtained from these two methods agree well with the experiment. It was noticed that flow separation and associated non-linear behaviour appear a little later in RANS and Euler predictions than in the experiment. The flow physics of viscous lateral flow development and vortex structure was captured well by RANS method. The VLM predicts a linear variation of lift and pitching moment with incidence angle and substantially under-predicts the induced drag. This method assumes the flow to be attached to the surface of the wing, whereas in reality swept UCAV configurations such as those considered in this study, experience highly separated flows on the upper surface of the wing.

The second topic concerned with the control of viscous spanwise flow development on the upper surface of a highly-swept wing to maximise the performance of control surfaces. Leading-edge and chordwise slots were considered for flow control purposes because they lie flush with the surface of the wing, and thus are expected to have a reduced RCS

signature. Standard techniques for passive flow control (Buchholz & Tso, 2000); (D. F. Anderson, 2000); (Kermode, 2012); (Gudmundsson, 2014b) can have a detrimental effect on RCS, therefore cannot be implemented on representative UCAV configurations. The flowfields of wings with leading-edge and chordwise slots were visualised with surface streamlines and compared against clean wings. It was found that the leading-edge method improved the flow control for the low angles of attack regime but was ineffective for a highly swept flying wing configuration at medium to high angles of attack. In contrast, wing with the chordwise slot showed better flow control results at high angles of attack, therefore a novel optimised design using chordwise slot was developed to maximise the performance of trailing edge control surfaces at medium to high angles of attack. However, before the optimisation of chordwise slot it was important to determine whether chordwise slots in the wing improved the lift upon the deflection of control surface. It was observed that percentage increase in lift is significant over a range of angles of attack and flap deflections but the total increase in lift is still very small. This still demonstrates that the operationality of the control surfaces at high angles of attack is improved when chordwise slot is present.

The main achievements of this work include the development and application of an optimised wing design using chordwise slots to maximise lift at medium to high angles of attack. The Pattern Search Method of numerical optimisation was used by changing four parameters of chordwise slot: location, width, length and angle. It should be noted that Pattern Search Method finds minimum or maximum of objective function for one variable at a time and thus cannot be used for global optimisation of the problem. The calculations of average mass flow rate for each parameter of chordwise slot were obtained from excel

spreadsheets, and processed into Matlab for the interpolation. An interpolation code was written in Matlab for the chordwise slot optimisation problem to estimate the values between known CFD data points. Novel flow control methods of leading-edge and chordwise slots were used for the first time on a flying wing configuration and they successfully control the flow by maximising the lift of wings with slots. The author would like to reiterate that although leading-edge slots have been used on low sweep wings to enhance the lift of air vehicles, to the best of the author's knowledge they have never been used to maximise the performance of control surfaces on highly swept UCAV configurations. Chordwise slots are a novel strand of this research, as author has not found any literature where this method was used for the purpose of passive flow control. Other achievements of this study include in depth CFD and experimental analysis of high-lift characteristics and flow physics of lateral flow development of moderately and highly swept UCAV configurations. Computational studies were carried out to understand and compare the capabilities of inviscid and viscous flow methods, and to predict the high-lift characteristics and vortex structure of flying wing configurations.

The current work has improved understanding of flow physics and high lift characteristics of moderately and highly swept UCAV configurations. For future work, the author recommends to run time dependent computations to more accurately predict the high lift characteristics of flying wing configurations under study. Yaw moments of flying wing configurations in sideslip angles are highly non-linear, therefore time dependent computations are required to capture the flow physics of the flying wing planforms in high sideslip angles (Tomac & Stenfelt, 2014). The phenomena of separated vortex flows appearing on flying wing configurations is characterised by unsteadiness, therefore LES

may be a more appropriate choice to compute flow physics for angles of attack near and post stall regimes. Improved experimental data obtained from high quality oil flow patterns, Pressure Sensitive Paints (PSP) and Particle Image Velocimetry (PIV) will benefit future investigations in this regard, as such data is essential for evaluation and validation of computational methods. The chordwise slot in this work can be fitted with a closing valve or may be interconnected to control surfaces in such a way that it only opens when control surfaces are deflected. The slot should remain in closed position when control surfaces are neutral, as this is important to reduce the drag at cruise speeds and for RCS purposes. Finally, the author recommends carrying out detailed investigations to study the effects of slots on RCS. Although slots are expected to have a reduced RCS in comparison to other passive flow control techniques where vertical or deflected surfaces are used, the precise effect of slots on RCS needs to be determined. The RAM and other such materials can benefit in this regard as they can be used around slots to help reduce RCS.

References

Abbott, M. B., & Basco, D. R. (1989). *Computational fluid dynamics*: Longman Scientific & Technical.

Alonso, J. J., LeGresley, P., & Pereyra, V. (2009). Aircraft design optimization. *Mathematics and Computers in Simulation, 79*(6), 1948-1958. doi:http://dx.doi.org/10.1016/j.matcom.2007.07.001

Anderson, D. F. (2000). *Understanding flight*. New York: McGraw-Hill.

Anderson, J. D. (1995). *Computational fluid dynamics : the basics with applications*. New York: McGraw-Hill.

Anderson, J. D. (1998). *A History of Aerodynamics: And Its Impact on Flying Machines*: Cambridge University Press.

Anderson, J. D. (2010). *Fundamentals of Aerodynamics*. Boston: McGraw-Hill Education.

Andersson, B. (2012). *Computational fluid dynamics for engineers*. Cambridge: Cambridge University Press.

ANSYS, I. (2019). Ansys Fluent. Retrieved from https://www.ansys.com/en-gb/products/fluids/ansys-fluent

Antoniou, A., & Lu, W. (2007). Practical optimization : algorithms and engineering applications.

Arora, J. S. (2011). *Introduction to optimum design*. Boston, MA: Academic Press.

B.S, K. R., & Poondla, A. (2017). Performance analysis of solar powered Unmanned Aerial Vehicle. *Renewable Energy, 104*, 20-29. doi:http://dx.doi.org/10.1016/j.renene.2016.12.008

Bamber, M., J. (1939). *Wind-tunnel tests of several forms of fixed wing slot in combination with a slotted flap on an NACA 23012 airfoil*. (Technical Note No. 702). Washington: NACA.

Barnard, R. H., & Philpott, D. (2010). *Aircraft flight: a description of the physical principles of aircraft flight*: Pearson Education.

Barnhart, R. K. (2012). *Introduction to unmanned aircraft systems*. Boca Raton: Taylor & Francis.

Barnwell, R. W., & Hussaini, M. Y. (2012). *Natural laminar flow and laminar flow control*. New York: Springer-Verlag.

Bertin, J. J. (2002). *Aerodynamics for Engineers* (4th ed.). USA: Prentice Hall.

Bolsunovsky, A. L., Buzoverya, N. P., Gurevich, B. I., Denisov, V. E., Dunaevsky, A. I., Shkadov, L. M., . . . Zhurihin, J. P. (2001). Flying wing—problems and decisions. *Aircraft Design, 4*(4), 193-219. doi:http://dx.doi.org/10.1016/S1369-8869(01)00005-2

Breitsamter, C. (2008). Unsteady flow phenomena associated with leading-edge vortices. *Progress in Aerospace Sciences, 44*(1), 48-65. doi:http://dx.doi.org/10.1016/j.paerosci.2007.10.002

Buchholz, M. D., & Tso, J. (2000). Lift Augmentation on Delta Wing with Leading-Edge Fences and Gurney Flap. *Journal of Aircraft, 37*(6), 1050-1057. doi:10.2514/2.2710

Campbell, J. F., & Osborn, R. F. (1986). Computation of Leading-Edge Vortex Flows. *Vortex Flow Aerodynamics, 1*, 305-330.

Cebeci, T. a. (2013). *Analysis of turbulent flows with computer programs* (Third edition. ed.). Oxford: Oxford : Butterworth-Heinemann.

Chapra, S. C., & Canale, R. P. (1985). *Numerical methods for engineers : with personal computer applications*. New York: McGraw-Hill.

Chen, C. J. (1997). *Fundamentals Of Turbulence Modelling*. Washington DC: Taylor & Francis.

Clark, R. M. (2000). *Uninhabited Combat Aerial Vehicles: Airpower by the People, For the People, But Not with the People*. Retrieved from College of Aerospace Doctrine, Research and Education, Air University, Maxwell Air Force Base, Alabama:

Coppin, J. (2014). *Aerodynamics, Stability and Shape Optimisation of Unmanned Combat Air Vehicles.* (PhD), University of Sheffield.

Crippa, S. (2008). *Advances in Vortical Flow Prediction Methods for Design of Delta-Winged Aircraft.* (PhD), Royal Institute of Technology (KTH), Stockholm, Sweden.

Cummings, R. M. (2015). *Applied Computational Aerodynamics: A Modern Engineering Approach*. New York: Cambridge University Press.

Cummings, R. M., Forsythe, J. R., Morton, S. A., & Squires, K. D. (2003). Computational challenges in high angle of attack flow prediction. *Progress in Aerospace Sciences, 39*(5), 369-384. doi:http://dx.doi.org/10.1016/S0376-0421(03)00041-1

Cummings, R. M., Morton, S. A., & McDaniel, D. R. (2008). Experiences in accurately predicting time-dependent flows. *Progress in Aerospace Sciences, 44*(4), 241-257. doi:http://doi.org/10.1016/j.paerosci.2008.01.001

Cummings, R. M., Morton, S. A., & Siegel, S. G. (2008). Numerical prediction and wind tunnel experiment for a pitching unmanned combat air vehicle. *Aerospace Science and Technology, 12*(5), 355-364. doi:http://dx.doi.org/10.1016/j.ast.2007.08.007

Cummings, R. M., & Schütte, A. (2013). Detached-Eddy Simulation of the vortical flow field about the VFE-2 delta wing. *Aerospace Science and Technology, 24*(1), 66-76. doi:http://dx.doi.org/10.1016/j.ast.2012.02.007

Davis, M. E. (1984). *Numerical methods and modeling for chemical engineers*. New York: Wiley.

Dehpanah, P., & Nejat, A. (2015). The aerodynamic design evaluation of a blended-wing-body configuration. *Aerospace Science and Technology, 43*, 96-110. doi:http://dx.doi.org/10.1016/j.ast.2015.02.015

Delery, J. M. (2001). Robert Legendre and Henri Werle: Toward the elucidation of three-dimensional separation. *Annual Review of Fluid Mechanics, 33*, 129-154. doi:10.1146/annurev.fluid.33.1.129

Earnshaw, P. B. (1961). *An experimental investigation of the structure of a leading-edge vortex*. (Aeronautical Research Council Reports and Memoranda, No. 3281).

El-Sayed, M., Sun, T., & Berry, J. (2005). Shape optimization with computational fluid dynamics. *Advances in Engineering Software, 36*(9), 607-613. doi:http://dx.doi.org/10.1016/j.advengsoft.2005.03.009

Elkhoury, M., & Rockwell, D. (2004). Visualized Vortices on Unmanned Combat Air Vehicle Planform: Effect of Reynolds Number. *Journal of Aircraft, 41*(5), 1244-1247. doi:10.2514/1.6290

Elle, B., & Britain, G. (1961). *An investigation at low speed of the flow near the apex of thin delta wings with sharp leading edges*. Retrieved from https://books.google.co.uk/books/about/Investigation_at_low_speed_of_the_flow_n.html?id=77C5XwAACAAJ&redir_esc=y

Ferziger, J. H., & Peric, M. (1999). *Computational Methods for Fluid Dynamics*. New York: Springer.

Frink, N. T., Tormalm, M., & Schmidt, S. (2012). Three Unstructured Computational Fluid Dynamics Studies on Generic Unmanned Combat Aerial Vehicle. *Journal of Aircraft, 49*(6), 1619-1637. doi:10.2514/1.C031383

Fujii, K., Gavali, S., & Holst, T. L. (1988). Evaluation of Navier-Stokes and Euler solutions for leading-edge separation vortices. *International journal for numerical methods in fluids, 8*(10), 1319-1329. doi:10.1002/fld.1650081014

Gad-el-Hak, M. (2000). *Flow Control: Passive, Active, and Reactive Flow Management*. New York: Cambridge University Press.

Görtz, S. (2005). *Realistic simulations of delta wing aerodynamics using novel CFD methods.* (PhD), Royal Institute of Technology (KTH), Stockholm, Sweden.

Gudmundsson, S. (2014a). Chapter 9 - The Anatomy of the Wing. In S. Gudmundsson (Ed.), *General Aviation Aircraft Design* (pp. 299-399). Boston: Butterworth-Heinemann.

Gudmundsson, S. (2014b). Chapter 10 - The Anatomy of Lift Enhancement. In S. Gudmundsson (Ed.), *General Aviation Aircraft Design* (pp. 401-457). Boston: Butterworth-Heinemann.

Gursul, I., Gordnier, R., & Visbal, M. (2005). Unsteady aerodynamics of nonslender delta wings. *Progress in Aerospace Sciences, 41*(7), 515-557. doi:https://doi.org/10.1016/j.paerosci.2005.09.002

Gursul, I., Wang, Z., & Vardaki, E. (2007). Review of flow control mechanisms of leading-edge vortices. *Progress in Aerospace Sciences, 43*(7–8), 246-270. doi:http://dx.doi.org/10.1016/j.paerosci.2007.08.001

Houghton, E. L., & Carpenter, P. W. (2003). *Aerodynamics for engineering students*: Butterworth-Heinemann.

Hummel, D., & Srinivasan, P. S. (1967). Vortex Breakdown Effects on the Low-speed Aerodynamic Characteristics of Slender Delta Wings in Symmetrical Flow. *J. R. Aeronaut. Soc. Journal of the Royal Aeronautical Society, 71*(676), 319-322.

Jahanmiri, M. (2010). *Active flow control: a review*. Retrieved from Research Report, Department of Applied Mechanics, Chalmers University of Technology:

James, S. (1987). *Euler analysis of the AFWAL 65-deg delta wing*. Paper presented at the 5th Applied Aerodynamics Conference. http://dx.doi.org/10.2514/6.1987-2272

Jenn, D. C. (1995). *Radar and laser cross section engineering*. Washington, DC: American Institute of Aeronautics and Astronautics.

Johnson, R. W. (1998). *The handbook of fluid dynamics*. Heidelberg: Springer-Verlag.

Johnston, L. J. (July 2012). *High-Lift Aerodynamics of Uninhabited Combat Air Vehicle Configurations with Reduced Radar Cross-Section Characteristics*. Paper presented at the RAES Applied Aerodynamics Conference, Bristol.

Joslin, R. D., Miller, D. N., & Lu, F. K. (2000). *Fundamentals and applications of modern flow control*: American Institute of Aeronautics and Astronautics.

Keane, A. J., & Nair, P. B. (2005). *Computational approaches for aerospace design : the pursuit of excellence*. Chichester, England: Wiley.

Keane, J. F., & Carr, S. S. (2013). A Brief History of Early Unmanned Aircraft. *Johns Hopkins APL Technical Digest, 32,* 558-571.

Kermode, A. C. (2012). *Mechanics of flight*. New York: Pearson Education.

Kerstin, H., Andreas, S., & Martin, R. (2012). *Numerical Investigation of the Aerodynamic Properties of a Flying Wing Configuration*. Paper presented at the 30th AIAA Applied Aerodynamics Conference. http://dx.doi.org/10.2514/6.2012-3325

Kingsley, S., & Quegan, S. (1992). *Understanding Radar Systems*. Berkshire: Mcgraw-Hill.

Klute, S. M., Rediniotis, O. K., & Telionis, D. P. (1996). Flow control over a maneuvering delta wing at high angles of attack. *AIAA Journal, 34*(4), 662-668. doi:10.2514/3.13125

Kundu, A. K. (2014). *Aircraft design*. Cambridge; New York: Cambridge University Press.

Lachmann, G. (1924). *Results of Experiments with Slotted Wings*. (Technical Note No. 282). NACA.

Lambourne, N. C., & Bryer, D. W. (1959). *Some Measurements in the Vortex Flow Generated by a Sharp Leading Edge Having 65 Degrees Sweep*. (Aeronautical Research Council Current Papers, No. 477). H.M. Stationery Office Retrieved from http://books.google.co.uk/books?id=xRX1MgEACAAJ.

Lambourne, N. C., & Bryer, D. W. (1961). *The Bursting of Leading-edge Vortices: Some Observations and Discussion of the Phenomenon*. (Aeronautical Research Council Reports and Memoranda, No. 3282). Retrieved from http://books.google.co.uk/books?id=GlXzMgEACAAJ.

Lee, C. (2014). Taranis and beyond: inspiring aerodynamic capability. *The Aeronautical journal., 118*(1206), 845-860.

Lee, C. (2016). Taranis and beyond: inspiring aerodynamic capability. *The Aeronautical Journal, 118*(1206), 845-859. doi:10.1017/S0001924000009593

Lewis, R. M., Torczon, V., & Trosset, M. W. (2000). Direct search methods: then and now. *Journal of Computational and Applied Mathematics, 124*(1–2), 191-207. doi:http://dx.doi.org/10.1016/S0377-0427(00)00423-4

Liu, C. (2007). *Wake vortex encounter analysis with different wake vortex models using Vortex-Lattice Method.* (MSc), Delft University of Technology.

Lomax, H., Pulliam, T. H., & Zingg, D. W. (2011). *Fundamentals of computational fluid dynamics*. Berlin; London: Springer.

Massey, B. S., & Ward-Smith, A. J. (2012). *Mechanics of fluids*. Boca Raton: CRC Press, Taylor & Francis Group.

McCormick, B. W. (1995). *Aerodynamics, aeronautics, and flight mechanics* (Vol. 2). New York: Wiley.

McLean, D. (2013). *Understanding aerodynamics arguing from the real physics*. Chichester: Chichester : Wiley-Blackwell.

Melin, T. (2000). *A Vortex Lattice Matlab Implementation for Linear Aerodynamic Wing Applications.* (Masters), Royal Institute of Technology.

Mistry, S. (2009). *A Novel Airframe Design Methodology for Silent Aircraft.* (PhD), Cranfield University.

Mitchell, A. M., & Délery, J. (2001). Research into vortex breakdown control. *Progress in Aerospace Sciences, 37*(4), 385-418. doi:http://dx.doi.org/10.1016/S0376-0421(01)00010-0

Moler, C. B. (2004). *Numerical computing with MATLAB*: SIAM.

Moran, J. (2012). *An Introduction To Theoretical and Computational Aerodynamics*. New York: Dover Publications.

Nathan, W., Zhijin, W., & Ismet, G. (2008). *Active Flow Control on a Nonslender Delta Wing*. Paper presented at the 46th AIAA Aerospace Sciences Meeting and Exhibit. http://dx.doi.org/10.2514/6.2008-740

Newsome, R. W., & Thomas, J. L. (1986). *Computation of leading-edge vortex flows*. (AGARD Conference Proceedings 494).

Nocedal, J., & Wright, S. J. (1999). *Numerical optimization*. New York: Springer.

Okonkwo, P., & Smith, H. (2016). Review of evolving trends in blended wing body aircraft design. *Progress in Aerospace Sciences, 82*, 1-23. doi:http://dx.doi.org/10.1016/j.paerosci.2015.12.002

Ordoukhanian, E., & Madni, A. M. (2014). Blended Wing Body Architecting and Design: Current Status and Future Prospects. *Procedia Computer Science, 28*, 619-625. doi:http://dx.doi.org/10.1016/j.procs.2014.03.075

Panton, R. L. (1990). Effects of a contoured apex on vortex breakdown. *Journal of Aircraft, 27*(3), 285-288. doi:10.2514/3.45932

Pattillo, D. M. (2001). *Pushing the Envelope: The American Aircraft Industry*: University of Michigan Press.

Peckham, D. H. (1958). *Low-speed Wind-tunnel Tests on a Series of Uncambered Slender Pointed Wings with Sharp Edges*. (Aeronautical Research Council Reports and Memoranda, No. 3186). H.M. Stationery Office Retrieved from http://books.google.co.uk/books?id=WQ8mnQEACAAJ.

Petrila, T., & Trif, D. (2005). *Basics of fluid mechanics and introduction to computational fluid dynamics*. New York: Springer.

Polhamus, E. C. (1969). *Predictions of vortex-lift characteristics based on a leading-edge suction analogy*. Paper presented at the 6th Annual Meeting and Technical Display. http://dx.doi.org/10.2514/6.1969-1133

Pozrikidis, C. (2017). *Fluid dynamics : theory, computation, and numerical simulation*. New York.

Rao, D. M. (1979). Leading Edge Vortex-flap Experiments on a 74 Deg. Delta Wing: NASA contractor report 159161, Old Dominion University Research Foundation, Norfolk, Virginia.

Rathakrishnan, E. (2013). *Theoretical aerodynamics*. Singapore: John Wiley & Sons.

Ravindran, A., Reklaitis, G. V., & Ragsdell, K. M. (2006). *Engineering optimization: methods and applications*: John Wiley & Sons.

Rehman, N. u. (2009). *Propulsion and Flight Controls Integration for the Blended Wing Body Aircraft.* (PhD), University of Cranfield.

Rizzi, A., & Engquist, B. (1987). Selected topics in the theory and practice of computational fluid dynamics. *Journal of Computational Physics, 72*(1), 1-69. doi:http://dx.doi.org/10.1016/0021-9991(87)90072-6

Rizzi, A., & Eriksson, L.-E. (1985). Computation of inviscid incompressible flow with rotation. *Journal of Fluid Mechanics, 153*, 275-312.

Roache, P. J. (1998). *Fundamentals of computational fluid dynamics*. Albuquerque, N.M.: Hermosa Publishers.

Robert, N., Thomas, C., Chuan, H., Hesham, O., Takashi, M., Mehul, P., & Ng, T. (2007). *Modification of the Flow Structure over a UAV Wing for Roll Control*. Paper presented at the 45th AIAA Aerospace Sciences Meeting and Exhibit. http://dx.doi.org/10.2514/6.2007-884

Schlichting, H., Gersten, K., Krause, E., Oertel, H., & Mayes, K. (1960). *Boundary-layer theory* (Vol. 7). New York: Springer.

Schminder, J. (2012). *Feasibility study of different methods for the use in aircraft coceptual design.* (Masters), Linkopings University. (LIU-IEI-TEK-A-12/01529-SE)

Schütte, A., Hummel, D., & Hitzel, S. M. (2012). Flow Physics Analyses of a Generic Unmanned Combat Aerial Vehicle Configuration. *Journal of Aircraft, 49*(6), 1638-1651. doi:10.2514/1.C031386

Shevell, R. S. (1989). *Fundamentals of Flight* (2nd ed.). New Jersey: Prentice Hall.

Shim, H. J., & Park, S. O. (2013). *Low-speed Wind-tunnel Test Results of a BWB-UCAV Model.* Paper presented at the Procedia Engineering.

Siouris, S., & Qin, N. (2007). Study of the effects of wing sweep on the aerodynamic performance of a blended wing body aircraft. *Proceedings of the Institution of Mechanical Engineers, Part G: Journal of Aerospace Engineering, 221*(1), 47-55.

Srigrarom, S., & Kurosaka, M. (2000). Shaping of Delta-Wing Planform to Suppress Vortex Breakdown. *AIAA Journal, 38*(1), 183-186. doi:10.2514/2.939

Sundaram, R. K. (1996). *A first course in optimization theory*. New York: Cambridge University Press.

Thompson, J. F., Warsi, Z. U. A., & Mastin, C. W. (1985). *Numerical grid generation: foundations and applications*. USA: North-Holland.

Thompson, S. A. (1992). *The Unsteady Aerodynamics of a Delta Wing Undergoing Large Amplitude Pitching Motions.* (PhD), University of Notre Dame. Retrieved from http://books.google.co.uk/books?id=g4u3SgAACAAJ

Tianyuan, H., & Xiongqing, Y. (2009). Aerodynamic/Stealthy/Structural Multidisciplinary Design Optimization of Unmanned Combat Air Vehicle. *Chinese Journal of Aeronautics, 22*(4), 380-386. doi:http://dx.doi.org/10.1016/S1000-9361(08)60114-4

Tomac, M., & Stenfelt, G. (2014). Predictions of stability and control for a flying wing. *Aerospace Science and Technology, 39*(0), 179-186. doi:http://dx.doi.org/10.1016/j.ast.2014.09.007

Tornado. (2019). A Vortex Lattice Method implemented in Matlab. Retrieved from http://tornado.redhammer.se/

Versteeg, H. K., & Malalasekera, W. (2007). *An Introduction to Computational Fluid Dynamics: The Finite Volume Method*. London: Pearson Education Limited.

Wesseling, P. (2010). *Principles of computational fluid dynamics*. Berlin: Springer-Verlag.

Wilcox, D. C. (1994). *Turbulence Modeling for CFD*. USA: DCW Industries.

Wilson, H. A., & Lovell, J. C. (1947). *Full-scale Investigation of the Maximum Lift and Flow Characteristics of an Airplane Having Approximately Triangular Plan Form*. (National Advisory Committee for Aeronautics (NACA) Research Memoranda, No. L7F16

). Retrieved from http://books.google.co.uk/books?id=xkfWSgAACAAJ.

Xing-Zhong, H., & Niek, V. (2003). *NATO RTO AVT Task Group-080 "Vortex Breakdown over Slender Wings": Objectives and Overview*. Paper presented at the 21st AIAA Applied Aerodynamics Conference. http://dx.doi.org/10.2514/6.2003-3939

Zikanov, O. (2010). *Essential computational fluid dynamics*. New Jersey: John Wiley & Sons.

Appendix

List of Publications

Ali, U., & Chadwick, E. (2016). Flow Control and High-Lift Performance for Flying-Wing Unmanned Combat Air Vehicle Configurations by inserting slots. *International Journal of Multiphysics, 10*(2). doi:10.21152/1750-9548.10.2.117

The results of Chapters 4, 5 and 6 were presented at Multiphysics Conference in Imperial College on 10-11 December 2015 London, under the title “High-Lift Performance and Flow Control for Flying-Wing Unmanned Air Vehicle Configurations using Leading-Edge and Cross-Flow Slots”

Fluent Summary Report

```
Fluent
Version: 3d, dp, dbns imp, S-A (3d, double precision, density-based
implicit, Spalart-Allmaras)
Release: 16.0.0
Title:

Models
------

   Model                        Settings
   ---------------------------------------------------------------
   Space                        3D
   Time                         Steady
   Viscous                      Spalart-Allmaras turbulence model
   Production Option            Vorticity
   Heat Transfer                Enabled
   Solidification and Melting   Disabled
   Radiation                    None
   Species                      Disabled
   Coupled Dispersed Phase      Disabled
   NOx Pollutants               Disabled
   SOx Pollutants               Disabled
   Soot                         Disabled
   Mercury Pollutants           Disabled

Material Properties
-------------------

   Material: air (fluid)

      Property                         Units      Method
Value(s)
      ------------------------------------------------------------------
-------------------
      Density                          kg/m3      ideal-gas    #f
      Cp (Specific Heat)               j/kg-k     constant     1006.43
      Thermal Conductivity             w/m-k      constant     0.0242
      Viscosity                        kg/m-s     sutherland
(1.716e-05 273.11 110.56 )
      Molecular Weight                 kg/kgmol   constant     28.966
      Thermal Expansion Coefficient    1/k        constant     0
      Speed of Sound                   m/s        none         #f

   Material: aluminum (solid)

      Property               Units    Method     Value(s)
      ------------------------------------------------------
      Density                kg/m3    constant   2719
      Cp (Specific Heat)     j/kg-k   constant   871
      Thermal Conductivity   w/m-k    constant   202.4

Cell Zone Conditions
--------------------

   Zones
```

```
      name    id   type
      ------------------
      fluid   5    fluid

   Setup Conditions

      fluid

         Condition                                                  Value
         ------------------------------------------------------------
----
         Material Name                                              air
         Specify source terms?                                      no
         Source Terms                                               ()
         Specify fixed values?                                      no
         Local Coordinate System for Fixed Velocities               no
         Fixed Values                                               ()
         Frame Motion?                                              no
         Relative To Cell Zone                                      -1
         Reference Frame Rotation Speed (rad/s)                     0
         Reference Frame X-Velocity Of Zone (m/s)                   0
         Reference Frame Y-Velocity Of Zone (m/s)                   0
         Reference Frame Z-Velocity Of Zone (m/s)                   0
         Reference Frame X-Origin of Rotation-Axis (m)              0
         Reference Frame Y-Origin of Rotation-Axis (m)              0
         Reference Frame Z-Origin of Rotation-Axis (m)              0
         Reference Frame X-Component of Rotation-Axis               0
         Reference Frame Y-Component of Rotation-Axis               0
         Reference Frame Z-Component of Rotation-Axis               1
         Reference Frame User Defined Zone Motion Function          none
         Relative To Cell Zone                                      -1
         Moving Mesh Rotation Speed (rad/s)                         0
         Moving Mesh X-Velocity Of Zone (m/s)                       0
         Moving Mesh Y-Velocity Of Zone (m/s)                       0
         Moving Mesh Z-Velocity Of Zone (m/s)                       0
         Moving Mesh X-Origin of Rotation-Axis (m)                  0
         Moving Mesh Y-Origin of Rotation-Axis (m)                  0
         Moving Mesh Z-Origin of Rotation-Axis (m)                  0
         Moving Mesh X-Component of Rotation-Axis                   0
         Moving Mesh Y-Component of Rotation-Axis                   0
         Moving Mesh Z-Component of Rotation-Axis                   1
         Moving Mesh User Defined Zone Motion Function              none
         Deactivated Thread                                         no
         Laminar zone?                                              no
         Set Turbulent Viscosity to zero within laminar zone?       yes
         Embedded Subgrid-Scale Model                               1
         Momentum Spatial Discretization                            0
         Cwale                                                      0.325
         Cs                                                         0.1
         Porous zone?                                               no
         Conical porous zone?                                       no
         X-Component of Direction-1 Vector                          1
         Y-Component of Direction-1 Vector                          0
         Z-Component of Direction-1 Vector                          0
         X-Component of Direction-2 Vector                          0
         Y-Component of Direction-2 Vector                          1
         Z-Component of Direction-2 Vector                          0
```

```
         X-Component of Cone Axis Vector                          1
         Y-Component of Cone Axis Vector                          0
         Z-Component of Cone Axis Vector                          0
         X-Coordinate of Point on Cone Axis (m)                   1
         Y-Coordinate of Point on Cone Axis (m)                   0
         Z-Coordinate of Point on Cone Axis (m)                   0
         Half Angle of Cone Relative to its Axis (deg)            0
         Direction-1 Viscous Resistance (1/m2)
2.111e+08
         Direction-2 Viscous Resistance (1/m2)
2.111e+08
         Direction-3 Viscous Resistance (1/m2)
2.111e+08
         Direction-1 Inertial Resistance (1/m)                    0
         Direction-2 Inertial Resistance (1/m)                    0
         Direction-3 Inertial Resistance (1/m)                    0
         C0 Coefficient for Power-Law                             0
         C1 Coefficient for Power-Law                             0
         Porosity                                                 1
         Relative Viscosity                                       1
         Equilibrium Thermal Model (if no, Non-Equilibrium)?      yes
         Non-Equilibrium Thermal Model?                           no
         Solid Material Name
aluminum
         Interfacial Area Density (1/m)                           1
         Heat Transfer Coefficient (w/m2-k)                       1
         3D Fan Zone?                                             no
         Inlet Fan Zone                                           0
         Fan Thickness (m)                                        0
         Fan Hub Radius (m)                                       0
         Fan Tip Radius (m)                                       0
         X-Component of 3D Fan Origin (m)                         0
         Y-Component of 3D Fan Origin (m)                         0
         Z-Component of 3D Fan Origin (m)                         0
         Rotational Direction                                     0
         Fan Operating Angular Velocity (rad/s)                   0
         Fan Inflection Point                                     0.83
         Limit Flow Rate Through Fan                              no
         Maximum Flow Rate (m3/s)                                 0
         Minimum Flow Rate (m3/s)                                 0
         Tangential Source Term                                   no
         Radial Source Term                                       no
         Axial Source Term                                        no
         Method                                                   0
         Pressure Jump (pascal)                                   0
         Fan Curve Fitting Method                                 0
         Polynomial Order                                         0
         Initial Flow Rate (m3/s)                                 0
         Fan Test Angular Velocity (rad/s)                        0
         Fan Test Temperature (k)                                 0
         Read Fan Curve                                           no

Boundary Conditions
-------------------

   Zones

      name        id   type
```

```
      -----------------------------------
      wing         2    wall
      symm         3    symmetry
      far-field    4    pressure-far-field

   Setup Conditions

      wing

         Condition                                                  Value
         -----------------------------------------------------------------
-
         Wall Thickness (m)                                         0
         Heat Generation Rate (w/m3)                                0
         Material Name
aluminum
         Thermal BC Type                                            1
         Temperature (k)                                            300
         Heat Flux (w/m2)                                           0
         Convective Heat Transfer Coefficient (w/m2-k)              0
         Free Stream Temperature (k)                                300
         Wall Motion                                                0
         Shear Boundary Condition                                   0
         Define wall motion relative to adjacent cell zone?         yes
         Apply a rotational velocity to this wall?                  no
         Velocity Magnitude (m/s)                                   0
         X-Component of Wall Translation                            1
         Y-Component of Wall Translation                            0
         Z-Component of Wall Translation                            0
         Define wall velocity components?                           no
         X-Component of Wall Translation (m/s)                      0
         Y-Component of Wall Translation (m/s)                      0
         Z-Component of Wall Translation (m/s)                      0
         External Emissivity                                        1
         External Radiation Temperature (k)                         300
         Wall Roughness Height (m)                                  0
         Wall Roughness Constant                                    0.5
         Rotation Speed (rad/s)                                     0
         X-Position of Rotation-Axis Origin (m)                     0
         Y-Position of Rotation-Axis Origin (m)                     0
         Z-Position of Rotation-Axis Origin (m)                     0
         X-Component of Rotation-Axis Direction                     0
         Y-Component of Rotation-Axis Direction                     0
         Z-Component of Rotation-Axis Direction                     1
         X-component of shear stress (pascal)                       0
         Y-component of shear stress (pascal)                       0
         Z-component of shear stress (pascal)                       0
         Fslip constant                                             0
         Eslip constant                                             0
         Surface tension gradient (n/m-k)                           0
         Specularity Coefficient                                    0
         Convective Augmentation Factor                             1

      symm

         Condition   Value
         -----------------
```

far-field

Condition	Value
Gauge Pressure (pascal)	0
Mach Number	0.091
Temperature (k)	300
Coordinate System	0
X-Component of Flow Direction	0.939693
Y-Component of Flow Direction	0
Z-Component of Flow Direction	0.34202
X-Component of Axis Direction	1
Y-Component of Axis Direction	0
Z-Component of Axis Direction	0
X-Coordinate of Axis Origin (m)	0
Y-Coordinate of Axis Origin (m)	0
Z-Coordinate of Axis Origin (m)	0
Turbulent Specification Method	2
Modified Turbulent Viscosity (m2/s)	0.0001
Turbulent Intensity (%)	5
Turbulent Length Scale (m)	1
Hydraulic Diameter (m)	1
Turbulent Viscosity Ratio	10

Solver Settings

Equations

Equation	Solved
Flow	yes
Modified Turbulent Viscosity	yes

Numerics

Numeric	Enabled
Absolute Velocity Formulation	yes

Relaxation

Variable	Relaxation Factor
Modified Turbulent Viscosity	0.8
Turbulent Viscosity	1
Solid	1

Linear Solver

Variable	Solver Type	Termination Criterion	Residual Reduction Tolerance
Flow	F-Cycle	0.1	
Modified Turbulent Viscosity	Flexible	0.1	0.7

Discretization Scheme

Variable	Scheme
Flow	Second Order Upwind
Modified Turbulent Viscosity	Second Order Upwind

Time Marching

Parameter	Value
Solver	Implicit
Courant Number	5

Solution Limits

Quantity	Limit
Minimum Absolute Pressure	1
Maximum Absolute Pressure	5e+10
Minimum Temperature	1
Maximum Temperature	5000
Maximum Turb. Viscosity Ratio	100000

Interpolation Code

```
clc;
clear;

% data imported from cfd simulations

x = 0:0.03:0.21;
y = [0.05956609 0.059904578 0.058966019 0.058080761
0.057933956 0.058012852 0.058073913 0.058215606];

% interpolated data
% linear, spline, or pchip methods can be used to
interpolate data

Xi = 0:0.01:0.21;
Yi = interp1 (x,y,Xi,'pchip');

plot (x,y,'*',Xi,Yi,'o')
grid on;
xlabel ('Trailing Edge Distance (m)')
ylabel ('Mass Flow (kg/s)')
legend ('CFD data','Interpolated data')
title ('Mass Flow Rate as function of
Location','FontSize',14)

% Find maximum mass flow rate and corresponding X value

Max_flowrate = max (Yi)
index = find (Yi == Max_flowrate);
Xindex = Xi (index)
```

Mass Flow Rate Calculations

Clean Model

X	Line1_U	Line2_U	Line3_U	Avg U	Line1_V	Line2_V	Line3_V	Avg V	Normal	Mass Flow
0.4077	20.71942	20.30998	18.65539	19.89493	35.56375	35.24331	33.00739	34.60482	35.43671	0.072291
0.412377	18.81856	18.38122	17.01738	18.07239	36.5087	36.08982	33.57715	35.39189	34.32824	0.07003
0.417054	17.78063	16.9782	15.676	16.81161	38.23547	37.90365	34.80785	36.98232	34.12649	0.069618
0.421732	18.68759	16.32811	14.60283	16.53951	38.06584	39.09464	36.44749	37.86932	34.37671	0.070128
0.426409	21.76805	17.11333	13.84387	17.57508	36.11231	38.80931	37.77769	37.56644	35.08453	0.071572
0.431086	25.88741	19.548	13.88471	19.77337	33.28229	37.18953	38.2904	36.25407	36.22542	0.0739
0.435763	29.67514	22.85219	15	22.50911	30.29963	34.58432	37.81054	34.2315	37.43489	0.076367
0.440441	32.52853	26.10181	17.03794	25.22276	27.53055	31.54693	36.31485	31.79744	38.40348	0.078343
0.445118	34.28722	28.66244	19.59851	27.51606	25.08914	28.48463	33.92482	29.1662	38.91182	0.07938
0.449795	35.16277	30.35715	22.0451	29.18834	22.92512	25.64223	31.0468	26.53805	38.89923	0.079354
0.454472	35.32721	31.22239	23.97393	30.17451	20.99261	23.10188	28.00164	24.03204	38.37526	0.078286
0.45915	34.95418	31.4223	25.24193	30.53947	19.26699	20.86321	25.0437	21.72463	37.43582	0.076369
0.463827	34.18022	31.09378	25.84943	30.37448	17.72109	18.903	22.3231	19.64907	36.17567	0.073798
0.468504	33.14401	30.40384	25.94755	29.8318	16.3271	17.16832	19.87879	17.7914	34.71541	0.070819
0.473181	31.87346	29.39499	25.5627	28.94371	15.0981	15.66264	17.75644	16.17239	33.09343	0.067511
0.477859	30.48724	28.2158	24.88327	27.8621	13.9808	14.32101	15.89068	14.73083	31.40445	0.064065
0.482536	29.00857	26.89259	23.95264	26.61793	13.00737	13.16147	14.28236	13.48373	29.68374	0.060555
0.487213	27.47052	25.47251	22.83596	25.25966	12.15748	12.14398	12.88187	12.39444	27.95225	0.057023
0.49189	25.90849	24.00964	21.61838	23.8455	11.3789	11.22442	11.64816	11.41716	26.23426	0.053518
0.496567	24.34732	22.52857	20.32738	22.40109	10.69736	10.43943	10.62123	10.586	24.56975	0.050122
0.501245	22.8025	21.05361	19.00647	20.95419	10.10524	9.762489	9.73693	9.868218	22.96439	0.046847
0.505922	21.29369	19.60331	17.67374	19.52358	9.598347	9.181404	8.975668	9.251806	21.4275	0.043712
0.510599	19.82134	18.1822	16.34521	18.11625	9.132283	8.6507	8.293087	8.692023	19.9408	0.040679
0.515276	18.39104	16.79722	15.03818	16.74215	8.692574	8.163341	7.695973	8.183962	18.51	0.03776
0.519954	17.00001	15.45154	13.76906	15.40687	8.274069	7.712394	7.169287	7.718583	17.13494	0.034955
0.524631	15.65364	14.1541	12.54948	14.11907	7.876003	7.295765	6.704359	7.292042	15.82081	0.032274
0.529308	14.35287	12.90583	11.37947	12.87939	7.491145	6.903508	6.284896	6.893183	14.56212	0.029707
0.533985	13.08401	11.69389	10.24983	11.67591	7.106541	6.520662	5.892574	6.506592	13.34053	0.027215
0.538663	11.78464	10.46514	9.12771	10.45916	6.721662	6.139565	5.514488	6.125238	12.1106	0.024706
0.54334	9.961991	8.96436	7.941646	8.955999	6.428174	5.744921	5.14303	5.772042	10.65486	0.021736
									28.31114	**0.057755**

Chordwise Cavity

X	Line1_U	Line2_U	Line3_U	Avg U	Line1_V	Line2_V	Line3_V	Avg V	Normal	Mass Flow
0.4077	21.15863	20.57115	18.94753	20.22577	36.74794	36.30708	34.1852	35.74674	36.33204	0.074117
0.412377	18.9553	18.49624	17.22289	18.22481	37.89267	37.29886	34.89495	36.69549	35.16076	0.071728
0.417054	17.61466	17.08601	15.82541	16.84203	40.18605	39.45618	36.21114	38.61779	35.03563	0.071473
0.421732	18.03516	16.1749	14.73767	16.31591	40.17249	41.2629	38.08859	39.84133	35.25391	0.071918
0.426409	21.79225	16.88427	13.85899	17.51184	37.92194	41.29031	40.22281	39.81169	36.24428	0.073938
0.431086	27.15931	19.76089	13.69253	20.20424	34.50304	39.44796	41.10929	38.35343	37.72216	0.076953
0.435763	32.00684	24.04712	14.89045	23.64813	31.12411	36.43998	40.77435	36.11281	39.40976	0.080396
0.440441	35.42419	28.20631	17.44247	27.02432	28.18147	32.90888	39.11289	33.40108	40.78587	0.083203
0.445118	37.50265	31.43292	20.69369	29.87642	25.62297	29.41412	36.3545	30.46386	41.59914	0.084862
0.449795	38.46255	33.47844	23.8764	31.93913	23.37225	26.23595	32.89185	27.50002	41.73374	0.085137
0.454472	38.55064	34.41194	26.33526	33.09928	21.36382	23.47548	29.24683	24.69538	41.19484	0.084037
0.45915	38.06312	34.56699	27.92308	33.51773	19.54734	21.07074	25.79024	22.13611	40.16435	0.081935
0.463827	37.15101	34.13322	28.68398	33.32274	17.91179	18.97712	22.68098	19.85663	38.7688	0.079088
0.468504	35.93468	33.26828	28.75934	32.6541	16.44676	17.15217	19.96544	17.85479	37.12465	0.075734
0.473181	34.50721	32.09762	28.30307	31.63596	15.13888	15.55671	17.62363	16.10641	35.32334	0.07206
0.477859	32.93446	30.70757	27.44615	30.36273	13.98015	14.16403	15.61837	14.58752	33.43132	0.0682
0.482536	31.26905	29.17154	26.30682	28.91581	12.96206	12.95245	13.90594	13.27348	31.50383	0.064268
0.487213	29.55254	27.54885	24.97909	27.36016	12.06767	11.89789	12.44602	12.13719	29.58087	0.060345
0.49189	27.81331	25.87829	23.53171	25.74111	11.28804	10.98829	11.21138	11.16257	27.69189	0.056491
0.496567	26.08097	24.20052	22.01906	24.10018	10.62147	10.21626	10.17424	10.33732	25.8652	0.052765
0.501245	24.37923	22.53955	20.47672	22.46517	10.04591	9.553333	9.299824	9.633024	24.10883	0.049182
0.505922	22.70575	20.90133	18.93248	20.84652	9.533639	8.97369	8.557835	9.021721	22.41647	0.04573
0.510599	21.06827	19.30092	17.42286	19.26401	9.077254	8.470797	7.93989	8.49598	20.80075	0.042434
0.515276	19.47955	17.75724	15.97598	17.73759	8.675746	8.040788	7.434787	8.05044	19.27554	0.039322
0.519954	17.94944	16.28271	14.60257	16.27824	8.322881	7.673849	7.023339	7.673356	17.84377	0.036401
0.524631	16.48845	14.88689	13.3098	14.89505	8.005807	7.355187	6.682007	7.347667	16.50385	0.033668
0.529308	15.0936	13.56714	12.09446	13.58506	7.70018	7.058427	6.38168	7.046762	15.23892	0.031087
0.533985	13.74056	12.29681	10.9308	12.32272	7.381152	6.758533	6.096523	6.745403	14.01384	0.028588
0.538663	12.3536	11.0114	9.788641	11.05121	7.046308	6.440732	5.81215	6.433063	12.77512	0.026061
0.54334	10.42469	9.463524	8.602845	9.497019	6.723558	6.072985	5.534016	6.110186	11.29281	0.023037
									29.80654	**0.060805**

Mass Flow Rate Calculations

Clean Model					**Chordwise Cavity**			
alpha	bottom	top	total mass		alpha	bottom	top	total mass
12.5	0.059324	0.049693	0.109017		12.5	0.059376	0.050544	0.10992
15	0.060403	0.052686	0.11309		15	0.060471	0.053779	0.114249
17.5	0.061358	0.055654	0.117012		17.5	0.061415	0.057148	0.118563
20	0.061896	0.057755	0.119651		20	0.061974	0.060805	0.122779
22.5	0.062155	0.058975	0.121129		22.5	0.062101	0.061909	0.12401
25	0.062222	0.058933	0.121155		25	0.062084	0.061359	0.123443
27.5	0.062216	0.057883	0.120098		27.5	0.062081	0.059361	0.121442
30	0.062177	0.05528	0.117457		30	0.062032	0.055513	0.117545

Velocity comparison over trailing edge on upper surface of the wing

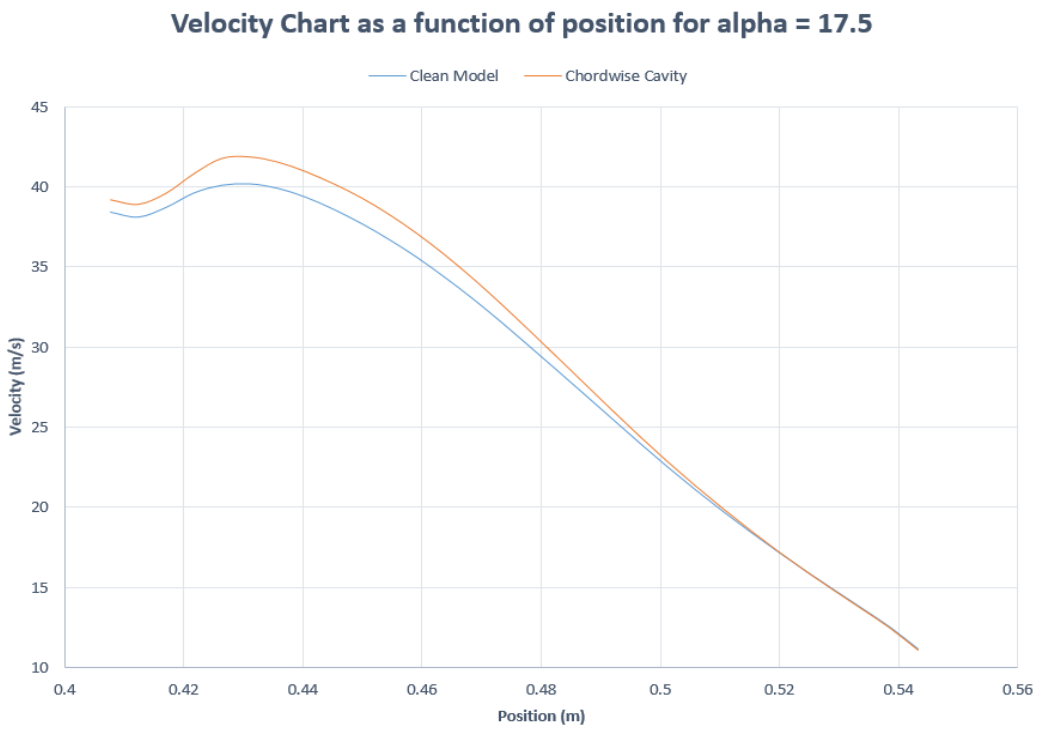

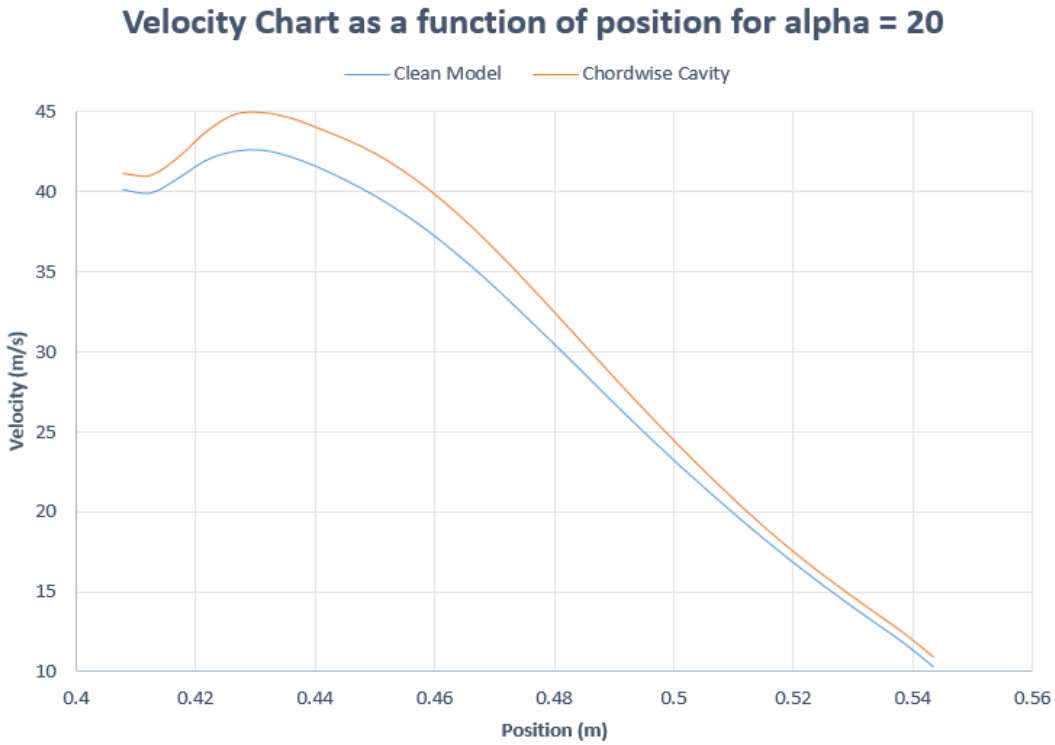

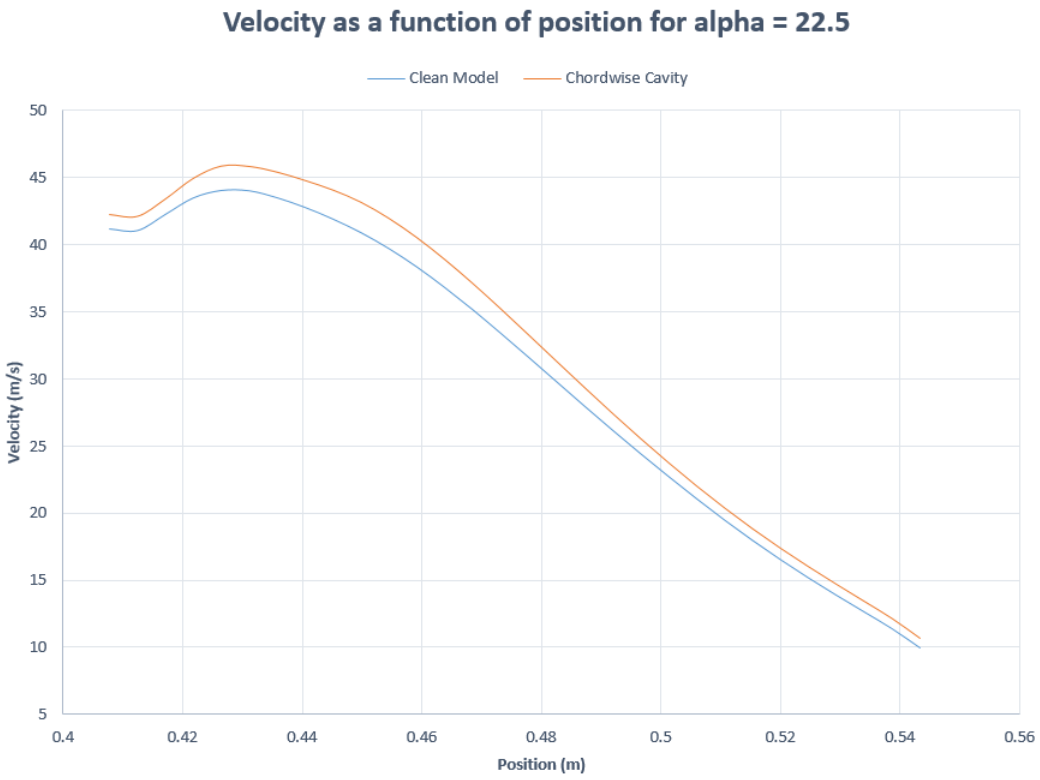
Velocity as a function of position for alpha = 22.5
Clean Model
Chordwise Cavity
Velocity (m/s)
50
45
40
35
30
25
20
15
10
5
0.4
0.42
0.44
0.46
0.48
0.5
0.52
0.54
0.56
Position (m)


Velocity as a function of position for alpha = 25
Clean Model
Chordwise Cavity
Velocity (m/s)
50
45
40
35
30
25
20
15
10
5
0.4
0.42
0.44
0.46
0.48
0.5
0.52
0.54
0.56
Position (m)

Mass flow rate comparison at bottom surface of the wing

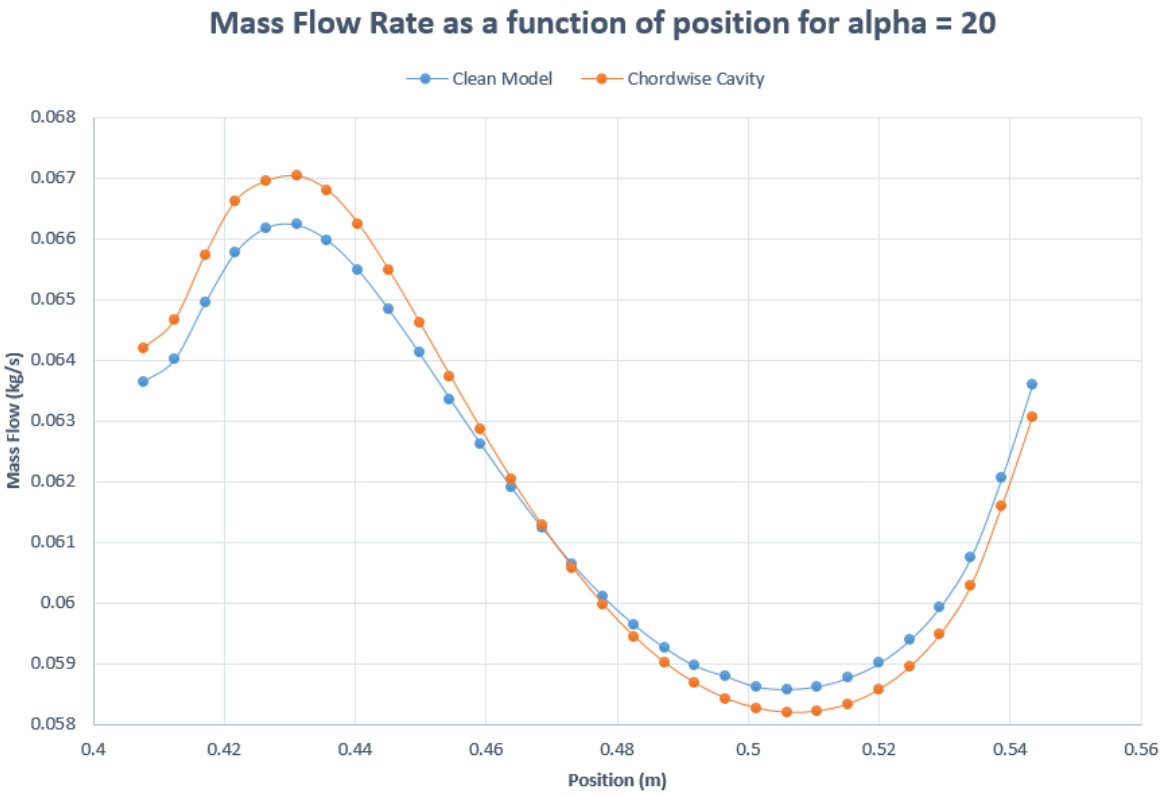

Calculations of wind tunnel test

UCAV 1 - No.1 LOW-SPEED WIND TUNNEL - 1:20 Scale Model

Patm:	774	mmHg			Date of Test:	27-Nov-13	
Wing Geometry							
Span:	0.8	m	**Calibrations**			Wing Pivot Point:	0.1 m behind root 1/4-chord (Based on UCAV 1)
Root Chord Based on UCAV 1):	0.4	m					
			Lift F.:	1mV =	0.2346 N		
Area (Based on UCAV 1):	0.147068	m^2	Drag F.:	1mV =	0.0763 N		
MAC (Based on UCAV 1):	0.229149	m	Pitch M.:	1mV =	0.0113 Nm		
			Side F.:	1mV =	0.1386 N		
			Roll M.:	1 mV =	0.006326 Nm		
			Yaw M.:	1 mV =	0.008048 Nm		
Wind Tunnel Conditions	Average for Run						
Ttunnel:	25.8	deg C	Air Speed:	31.665	m/s		
Betz Reading:	5.130	mbar	Reynolds Number:	473,576	based on MAC		
Air Density:	1.2025	kg/m^3	Mach Number:	0.091			
Air Viscosity:	1.84236E-05	kg/ms					
Force Measurements from Incidence Angle Sweep					Yaw Angle:	0 deg	

Calculations of wind tunnel test

uncorr								Wind-Off Readings							uncorr						corr		corr	
alf (deg)	L (mV)	D (mV)	PM (mV)	RM (mV)	SF (mV)	YM (mV)	Betz (mbar)	Lo (mV)	Do (mV)	PMo (mV)	RMo (mV)	SFo (mV)	YMo (mV)		CL	CD	CM	Croll	Cside	Cyaw	epsilon	alf (deg)	CL	CD	CM
-22.0	-462.177	770.494	-533.865	-23.856	-13.679	43.396	5.100	0.239	-2.049	17.795	-0.557	-1.124	0.726		-1.23093	0.66884	0.22850	-0.00209	-0.01974	0.00487	-0.022686	-22.232	-1.23093	0.66011	0.22850
-19.5	-417.540	604.513	-456.434	-86.254	-9.827	35.166	5.100	-1.352	7.379	1.890	-89.656	-1.958	0.158		-1.10788	0.51698	0.22702	0.00031	-0.01238	0.00400	-0.020418	-19.602	-1.10788	0.50294	0.22702
-16.5	-380.942	469.414	-351.016	-167.702	-9.401	21.421	5.190	-0.401	-2.493	11.971	-86.063	-1.267	0.564		-0.99542	0.40147	0.23481	-0.00720	-0.01257	0.00234	-0.018345	-16.483	-0.99542	0.38308	0.23481
-13.5	-345.213	343.745	-187.189	-168.353	-10.670	10.096	5.220	-1.185	4.933	0.138	-92.592	-2.422	0.486		-0.89474	0.28659	0.28805	-0.00664	-0.01267	0.00107	-0.016490	-13.377	-0.89474	0.26469	0.28805
-11.0	-280.055	230.021	-113.512	-156.602	-6.362	6.525	5.250	-0.209	-1.837	10.983	-96.520	-1.771	0.628		-0.72365	0.19500	0.24813	-0.00524	-0.00701	0.00065	-0.013337	-10.696	-0.72365	0.16800	0.24813
-8.5	-214.345	133.106	-96.322	-151.491	-6.287	3.417	5.300	-0.553	-1.023	-2.580	-93.790	-2.470	0.521		-0.54763	0.11174	0.18851	-0.00498	-0.00578	0.00032	-0.010093	-8.010	-0.54763	0.08062	0.18851
-6.0	-140.048	79.119	-31.723	-111.553	-5.153	7.739	5.340	-0.355	-3.929	3.826	-84.874	-2.107	1.068		-0.35514	0.06867	0.13599	-0.00229	-0.00458	0.00073	-0.006545	-5.307	-0.35514	0.03434	0.13599
-3.0	-65.554	48.109	-1.993	-106.385	-2.487	3.261	5.340	-1.223	-2.760	-2.164	-92.997	-1.980	1.167		-0.16355	0.04206	0.07146	-0.00115	-0.00076	0.00023	-0.003014	-2.105	-0.16355	0.00590	0.07146
0.0	16.597	39.466	46.367	-83.121	-0.880	3.160	5.360	-0.065	-4.989	-7.644	-97.106	-0.783	1.328		0.04220	0.03662	0.01034	0.00119	-0.00015	0.00020	0.000778	1.113	0.04220	0.00000	0.01034
2.0	100.162	53.037	92.627	-68.711	1.034	8.010	5.360	1.205	-4.057	-4.485	-79.616	-1.718	1.964		0.25064	0.04703	-0.05768	0.00093	0.00412	0.00066	0.004619	3.333	0.25064	0.01154	-0.05768
5.0	194.574	99.397	149.740	-48.737	2.766	12.610	5.340	-0.414	-2.688	-18.848	-84.179	-1.313	2.421		0.49572	0.08441	-0.12624	0.00304	0.00613	0.00111	0.009136	6.592	0.49572	0.05229	-0.12624
7.5	272.748	170.867	215.404	-61.181	1.546	24.126	5.320	1.217	0.444	-3.465	-70.211	-2.272	2.491		0.69292	0.14144	-0.18498	0.00078	0.00576	0.00237	0.012770	9.300	0.69292	0.11364	-0.18498
10.0	325.289	262.413	318.660	-48.198	3.199	30.177	5.270	-0.427	-4.459	-25.602	15.758	-1.146	3.322		0.83908	0.22359	-0.17975	-0.00555	0.00661	0.00297	0.015464	11.954	0.83908	0.19992	-0.17975
13.0	375.931	379.668	421.804	-22.483	1.877	31.573	5.200	1.377	3.436	-6.260	-41.026	-1.939	3.002		0.97788	0.31946	-0.19183	0.00163	0.00588	0.00320	0.018022	15.101	0.97788	0.30043	-0.19183
15.5	426.440	517.209	516.695	7.709	3.291	38.519	5.170	0.600	-7.603	-35.528	-90.335	-0.396	2.737		1.11822	0.44821	-0.18318	0.00868	0.00572	0.00403	0.020608	17.749	1.11822	0.43460	-0.18318
18.5	463.985	656.567	586.947	19.042	4.407	48.585	5.100	1.681	2.857	-13.278	-7.345	-1.091	4.053		1.23064	0.56596	-0.20119	0.00237	0.00865	0.00508	0.022680	20.868	1.23064	0.55721	-0.20119
21.0	488.892	789.595	612.025	14.880	3.301	64.694	5.050	0.261	-9.400	-40.104	-70.709	-0.492	3.504		1.31359	0.69859	-0.20474	0.00776	0.00602	0.00705	0.024209	23.455	1.31359	0.69374	-0.20474
23.5	502.553	911.501	603.209	8.944	5.211	82.961	4.960	1.752	1.678	-20.549	-53.725	-1.238	4.339		1.37074	0.80992	-0.23932	0.00578	0.01043	0.00923	0.025262	26.015	1.37074	0.80790	-0.23932
26.5	504.244	1021.253	534.432	-10.114	6.683	89.828	4.900	0.831	-8.156	-52.459	-5.539	-1.408	3.776		1.39476	0.92760	-0.26688	-0.00043	0.01324	0.01022	0.025705	29.041	1.39476	0.92680	-0.26688
29.0	488.290	1094.807	377.590	24.446	3.691	69.898	4.890	2.533	3.367	-31.038	-2.090	-0.769	5.115		1.34860	0.98551	-0.35006	0.00248	0.00732	0.00771	0.024854	31.492	1.34860	0.98237	-0.35006
31.5	449.470	1088.208	167.228	32.886	2.375	57.462	4.890	1.189	-8.966	-68.408	-94.121	-2.044	3.624		1.24455	0.99068	-0.40561	0.01189	0.00725	0.00641	0.022937	33.882	1.24455	0.98258	-0.40561
34.0	430.426	1148.544	121.566	32.646	4.186	63.038	4.850	1.998	-0.564	-47.739	6.344	-0.733	4.201		1.19925	1.04613	-0.42373	0.00248	0.00813	0.00706	0.022102	36.334	1.19925	1.03599	-0.42373
36.5	416.452	1221.802	90.066	-6.615	3.147	57.519	4.840	1.074	-7.953	-73.993	-127.662	-1.100	1.886		1.16512	1.12187	-0.41173	0.01144	0.00704	0.00669	0.021473	38.798	1.16512	1.11023	-0.41173
39.0	405.417	1294.757	75.611	-3.379	2.253	65.837	4.790	2.146	4.002	-57.785	-25.511	0.689	-2.389		1.14296	1.18981	-0.41931	0.00211	0.00262	0.00829	0.021064	41.275	1.14296	1.14934	-0.41931

Lift Coefficient Calculations

Alpha = 20

Deflection	Clean Rotated	Clean	Difference Clean	Chordwise Rotated	Chordwise	Difference Slot
5	8.88E-01	0.87301007	1.48E-02	0.87964468	8.60E-01	1.99E-02
10	0.89409494	0.87301007	2.11E-02	0.89234811	0.85975282	3.26E-02
15	0.90289179	0.87301007	2.99E-02	0.90015687	0.85975282	4.04E-02
20	0.90999456	0.87301007	3.70E-02	0.91061014	0.85975282	5.09E-02
25	1.0253044	0.98945447	3.58E-02	1.0253032	0.98627272	3.90E-02
30	0.92844873	0.87301007	5.54E-02	0.92027544	0.85975282	6.05E-02